ROVIBRONIC SPECTROSCOPY OF SYMPATHETICALLY COOLED CaH^+ IN COULOMB CRYSTALS

A Dissertation
Presented to
The Academic Faculty

By

Aaron Calvin

In Partial Fulfillment
of the Requirements for the Degree
Doctor of Philosophy in the
School of School of Chemistry and Biochemistry, Georgia Institute of Technology

Georgia Institute of Technology

August 2018

ROVIBRONIC SPECTROSCOPY OF SYMPATHETICALLY COOLED CaH^+ IN COULOMB CRYSTALS

Approved by:

Dr. Kenneth R. Brown, Advisor
School of Chemistry and Biochemistry, School of Physics, School of Computer Science
Georgia Institute of Technology

Dr. Thomas Orlando
School of Chemistry and Biochemistry
Georgia Institute of Technology

Dr. Joseph Perry
School of Chemistry and Biochemistry
Georgia Institute of Technology

Dr. David Sherrill
School of Chemistry and Biochemistry
Georgia Institute of Technology

Dr. Chandra Raman
Georgia Institute of Technology
Georgia Institute of Technology

Date Approved: May 17, 2018

When we try to pick out anything by itself, we find it hitched to everything else in the Universe.

John Muir

To my parents.

ACKNOWLEDGEMENTS

While looking into grad school, I heard several horror stories about life as a graduate student. This was not one of them. First, I have to thank my advisor, Dr. Kenneth Brown for guidance along the way and incredible insight in the field. It was an incredible experience being exposed to topics as diverse as cold chemistry to quantum computing.

The group cultivated a collaborative culture and ultimately convinced me that this was the lab to join. I am fortunate to have supportive mentors and friends who were more than willing to discuss science and have fun outside of lab. Gang (Rick) Shu, I hope we will be able to go hiking again someday. Thanks for the help in the lab as well as photography tips. To René Rugango, you really taught me everything to know about trapping and really got the CaH^+ experiments going. Smitha Janardan, it was a pleasure writing with you and thanks for all the calculations. John Condollci, the music you introduced me to on the drive from Illinois is incredible. I'd also like to thank Kisra Egodapitiya, Jyothi Saraladevi, Zhubing (Gloria) Jia, Omid Khosravani, and Bichen Zhang for always being willing to help out. To the theorists Colin Trout, Mauricio Gutierrez, Pak Hong (James) Leung, Muyuan Li, Natalie Brown, and Eric Sabo, I enjoyed the conversations about quantum computing and helpful questions/criticisms during practice talks. I'd like to thank Eric Pretzch, and Evan Reed for all the hard work they did in the molecular experiments and I wish them the best in their graduate career.

Thanks to my parents for being supportive and always being available for advice. To my brother, Adam, it's been nice to have been able to share an apartment filled with your amazing artwork. Keep it up! To my neighbors Mary Francis and Meg, I will miss those afternoons on the porch and I appreciate your hospitality. Thanks to Krystin Allaire for you catching all of those mistakes in the paper that I must have overlooked thousands of times! Your encouragement has really gotten me through the most stressful times in grad school.

Finally, I would like to acknowledge the Army Research Office and the National

Science Foundation for funding.

TABLE OF CONTENTS

LIST OF TABLES

LIST OF FIGURES

SUMMARY

CaH^+ is an astrophysically relevant molecule with proposed applications in fundamental physics. CaH^+ is co-trapped with Doppler cooled Ca^+ to perform resonance enhanced multi-photon dissociation spectroscopy with a frequency doubled, mode locked Ti:Sapph laser. This method was used to measure the vibronic spectrum of the $1^1\Sigma, v = 0 \rightarrow 2^1\Sigma, v' = 0, 1, 2, 3$ transitions. Spectroscopy on the deuterated isotopologue, CaD^+ confirmed a revised assignment of the CaH^+ vibronic levels and a disagreement with MS-CASPT2 theoretical calculations by approximately 700 cm^{-1}. Updated high-level coupled-cluster calculations that include core-valence correlations reduce the disagreement between theory and experiment to 300 cm^{-1}. The broad bandwidth of the pulsed Ti:sapph provided an advantage for the initial search for transitions, but did not allow spectral resolution of rotational transitions. Pulse shaping was applied to spectrally narrow the linewidth of the pulsed laser to obtain rotational constants for the $2^1\Sigma, v' = 0, 1, 2, 3$ and $1^1\Sigma, v = 0$ states. This measurement has value in the control of quantum states of the molecule to enable high precision measurements of rovibrational transitions using quantum logic spectroscopy.

CHAPTER 1
INTRODUCTION

1.1 Motivation for spectroscopy of cold molecular ions

Spectroscopy of molecular ions in Coulomb crystals has gained attention in recent years for the high degree of control this platform affords. Despite the challenges associated with molecular ions such as low densities due to Coulomb repulsion, poor yields, and large reaction cross sections, spectroscopy of molecular ions is imperative in understanding reaction mechanisms such as ionic reactions in organic chemistry [1, 2] or the reactions proposed to occur in space [3, 4]. Ion traps provide an isolated environment for the creation and study of reactive species whose spectra are lacking compared to their neutral counterparts. As an example, CaH was identified in sunspots over a century ago [5], yet endothermic reactions of Ca^+ in the ground state with H_2 [6] hindered the spectroscopy of the molecular ion. Spectroscopy of this molecular ion was only recently performed in Coulomb crystals with the measurement of a dissociative transition [7], two vibrational overtones [8], non-destructive state detection [9], finally the vibronic [10, 11] and rovibronic [12], transitions discussed in this thesis. Trapping molecular ions in a Coulomb crystal allows a high degree of localization and long storage times that enable the observation of weak transitions on as few as single ions. These molecular ions are translationally cooled to millikelvin temperatures by the Coulomb interaction with the Doppler-cooled atomic ions and can be cooled further to tens of microkelvin by sympathetic sideband cooling. The control of the molecular ion's internal degrees of freedom is an active area with promising methods in development. This pristine control, combined with progress made in controlling molecular beams, will allow the study of cold, controlled ion-neutral reactions that tests our current models of processes vital to

chemistry in general, and in particular astrochemistry. Additionally, this control will enable efficient measurements of narrow transitions using of quantum logic techniques to probe fundamental physics.

1.1.1 A new platform for spectroscopy

Coulomb repulsion limits the density of molecular ions and makes spectroscopy difficult compared to their neutral counterparts. Fluorescence measurements are impractical for low densities of molecular ions, so some form of action spectroscopy is generally adopted. These methods rely on a chemical reaction to indicate a transition; commonly dissociation or photo-activated charge exchange. Reaction products are traditionally detected via mass spectrometry [13–16]. The advantage of co-trapping molecular ions in a Coulomb crystal is the ability to probe a reaction from a change in the fluorescing atomic ion. A variety of methods at a range of wavelengths from tens of kilohertz to hundreds of terahertz allows indicates the versatility of Coulomb crystals for spectroscopy. Many species of interest to physicists and chemists can be trapped and sympathetically cooled from the lightest, H_2^+ [17], to proteins. With Ba^+, molecular ions up to 410 Da [18] as well as multiply charged cytochrome c [19] are trapped and sympathetically cooled. Extending this, spectroscopy on large, complex molecules with high sensitivity was demonstrated when transitions in single aniline ions were studied using nondestructive mass determination to characterize consecutive dissociation products [20].

Two vibrational overtones (between 800 and 900 nm) in CaH^+ were measured for a single molecule at a time using resonance enhanced photodissociation (REMPD) [8]. REMPD was easily extended to the electronic transition at around 400 nm with rotational resolution [12]. The hyperfine resolution of rovibrational lines in HD^+ shows the extension of spectroscopy into the mid-IR [21]. Each case demonstrates how the response of the molecular ions over a range of wavelengths can be detected by the fluorescence of the atomic ion around 300 to 400 nm. The rotational spectra of CaH^+ in the electronic

ground state using stimulated Raman transitions to coherently excite phonons in the crystal conditional on the initial state of the molecular ion shows resolution of magnetic sub-levels with about a 10 kHz spacing [9].

Monitoring a change in the atomic ion's fluorescence may be accomplished in a variety of ways. The change in the Coulomb crystal's structure is one indicator of reactions. In one case [22], the fundamental vibrational transition of N_2^+ is probed. N_2^+ is prepared in the ground vibrational state [23] and are sympathetically cooled in the interior of a Ca^+ Coulomb crystal. Vibrationally excited N_2^+ will undergo charge exchange with background Ar. The loss of N_2^+ in the interior and collection of Ar^+ on the shell is observed and comparison with numerical simulations provide an estimate of the N_2^+ lost as a function of the probe laser. In another example, a non-destructive form of mass spectrometry is performed by exciting the mass-dependent motion of the ions [21]. A change in the atomic ion fluorescence occurs as the motion heats the crystal and changes the laser detuning the atomic ion experiences due to the Doppler effect. A suppression of this fluorescence change indicates resonance enhanced photodissociation. Finally, when the molecular ion dissociates into fluorescing ions, the dissociation product can be directly detected [8, 10–12]. As discussed later, those alkaline earth hydride ions are of interests to physicists for precision measurements with this destructive method providing a convenient preliminary spectrum.

1.1.2 Quantum state control of molecular ions

Full quantum state control for both neutral [24–26] and ionized molecules is currently driving much research in the field of molecular physics. State control will enhance spectroscopic signals by increasing the number of ions in the state being addressed. In the context of precision measurements, non-destructive detection of transitions in state controlled molecules should allow a high signal to noise ratio to measure weak clock transitions for probing the time change of fundamental constants. State control is also of

interest in state controlled chemical reactions to fully map the state to state dynamics of cold reactions.

While the translational motion of molecular ions are automatically cooled to millikelvin temperatures by sympathetic cooling from the Doppler cooled atomic ion, further cooling to microkelvin temperatures is achieved by sympathetic sideband cooling to approach the ground state of motion. This technique relies on optically pumping on the resolved red sideband of the crystal's motional mode and is discussed in detail later. So far the technique has been demonstrated with CaH^+ [9, 27], and MgH^+ [28].

Even though the translational temperature can approach the quantum limit, the internal states have weak coupling to the external degrees of freedom and are still at equilibrium with the surroundings. Molecular ions generally decay to the ground electronic state and for diatomic hydrides, only the ground vibrational state is populated to a significant degree due to the large energy difference between vibrational levels. However, the molecules are typically rotationally excited [29–31].

Many approaches to controlling the rotational state have been proposed and implemented including cryogenic cooling of the molecule's surroundings [32], optical pumping [21, 33, 34], and buffer gas cooling [35–37]. AlH^+ can be rotationally cooled by optical pumping using pulse shaping to filter out the blue frequencies to drive only the P branch transitions. This is possible because of the nearly diagonal Franck-Condon factors [38]. This scheme should be extended to molecular ions with diagonal Franck-Condon factors such as BH^+ [39] and possibly SiO^+, although more recent measurements indicate the latter is less diagonal than predicted [40]. Optical pumping on a rovibrational transition takes advantage of rotational selection rules and blackbody radiation-induced quantum jumps between rotational levels to drive the population to the ground rovibrational state. This was used to rotationally cool MgH^+ [34], and control hyperfine states of HD^+ [21]. Coherent state preparation by projecting into a pure rotational state was predicted [41] and realized in CaH^+ [9] with control of the magnetic sublevels. This

technique relied on blackbody redistribution to populate the desired rotational state, however a frequency comb covering multiple transitions should populate the state on timescales faster than the blackbody rates [41, 42].

Buffer gases are frequently used to cool internal degrees of freedom. The helium nanodroplets are used to quench higher vibrational levels to rid the resulting spectrum of hot bands. Inspired by the success of these techniques, buffer gas cooling is used in tandem with Coulomb crystals. Vibrational cooling of $BaCl^+$ co-trapped in a Yb^+ Coulomb crystal overlapped with laser cooled calcium atoms was achieved [43], and theoretically explored [44, 45] for extension to other species.

Finally homonuclear diatomics are of interest to several groups who published studies on O_2^+ [46, 47], N_2^+ [48], and H_2^+ [49, 50]. The lack of a permanent dipole offers protection against blackbody induced rotational excitations. In particular, the creation of N_2^+ in a desired rovibrational state using a state-selective photoionization technique [23] allowed the measurement of a dipole-forbidden vibrational transition [22] which has applications analogous to the electric-quadrupole transitions in atomic ion clocks. These molecular ions have vibrational states that are insensitive to magnetic field fluctuations; however, the measurement was destructive and requires nine orders of magnitude improvement to compete with the best atomic ion clocks [51].

1.1.3 Cold chemistry and astrochemical applications

Astrochemistry is faced with the task of understanding how complex molecules are formed. To highlight a specific problem, a forest of unassigned transitions observed in the diffuse interstellar clouds known to contain mostly molecules [52]. The molecules form within the cloud [53] prompting the question of how reactions could occur, assuming Arrhenius behavior, at such low densities and energy. Ion-molecule reactions have large rates that indicate ions play a significant role in astrochemistry. Identification is the first step in understanding the roles of molecular ions in interestellar chemistry. Except for a

few simple molecules, such as HD^+ where theory and experiment agree up up to sixth order in the fine structure constant [54], quantum chemistry calculations currently do not provide spectroscopic quality results. For CaH^+, initial theoretical calculations underestimated the electronic transition by 700 cm^{-1} with CaD^+ spectroscopy necessary to confirm the labeling of vibronic transitions [10, 11]. Improved theoretical calculations [11] still underestimated the transition by 300 cm^{-1} which remains far from the accuracy required for astrochemical identification. As a result, ion spectroscopy provides benchmarks for quantum chemical calculations.

With the spectra necessary for confirmation, measurements of ion-molecule rates are crucial for inferring the densities of molecular ions in interstellar space [53]. Coulomb crystals are currently being explored to measure reaction kinetics with promising results. In addition, the of full quantum controlled chemistry provides insight into the details of non-Arrhenius behavior such as tunneling and submerged barriers that may influence reaction kinetics at low temperatures and densities. Aside from astrochemistry, these ion-molecule reactions are important in understanding the fundamental processes underlying practical applications like plasma etching [55] and reactions in organic chemistry [1, 2]. As important as the reactions are to organic chemistry in the identification of reaction pathways and predicting yields [2], this class of reactions has limited studies at the fundamental level [56]. Coulomb crystals present a unique opportunity of detailed studies of these reactions because of the degree of control afforded. As discussed earlier, methods are being developed to control the internal state of molecular ions. Given progress made in decelerated molecular beams [57–59], state controlled chemical reactions are possible in distinguishing competing pathways of reactants in different quantum states for understanding fundamental reaction mechanisms [60].

Coulomb crystals have allowed the study of several cold reactions that are easily extended to any reaction of interest. While beam experiments studied the reaction of the

ground state alkaline earth ions with H_2, D_2, and HD [6, 61], more recent research extends reaction studies to reactions with excited state atomic ions. Moreover, these experiments extract quantitative information of reaction kinetics at the single ion level taking advantage of ion cycling reactions [7, 62]. This may be advantageous for limited samples, such as in investigating chemical properties of transactinide elements with strong influence of the relativistic effects of the electron. In addition to hydrogen and deuterium, N_2O [63], CH_3F [64], CH_3F, CH_2F_2, and CH_3Cl [65] and the radical NO [56] have been studied for their reactions with Ca^+. In these cases, state control of the atomic ion is demonstrated using the detuning of the cooling lasers. The relative population in the ground and excited states are estimated from the optical-Bloch equations. The rate constants of the excited states were generally found to be in line with capture theories, however, suppression of ground state kinetics indicates the existence of submerged barriers [56, 65].

The reactant ion need not be a laser cooled atomic ion. Molecular ions or atomic ions that cannot be laser cooled can nonetheless be trapped and quickly cooled by Coulomb interactions with a laser cooled ion. Example reactions studied in Coulomb crystals include $OCS^+ + ND_3 \rightarrow OCS + ND_3^+$ [66] where selective loading of the molecular ion is achieved by resonantly exciting the secular motion to heat and eject undesired contaminants from the crystal. The same controlled loading was used to create a Coulomb crystal with $BaOCH_3^+$ from the reaction of laser cooled Ba^+ with methanol [67]. $BaOCa^+$ formed in the triplet enabled reaction of $BaOCH_3^+$ with laser cooled Ca in a MOT. This demonstrates the opportunity to study chemical species with exotic bonding and testing new formation pathways.

While the field of cold chemistry in Coulomb crystals is relatively new, experiments so far demonstrate this versatile setup holds promise filling in gaps of molecular spectra and kinetics useful for astrochemical applications as well as challenging conventional notions of bonding and reaction dynamics.

1.1.4 Tests of quantum theory

One current area of interest in the field is in precision measurement for testing proposed changes in physical constants. The standard model is known to be incomplete because it fails to explain the matter-antimatter asymmetry, dark matter, dark energy, and gravity. Yet, all the predictions of the standard model have been experimentally confirmed within the current limit of our detection [68]. Some hypotheses beyond the standard model predict a small change in the relative strengths of the fundamental forces, for instance the weak force relative to the strong. This would manifest itself as a change in the ratio of the mass of the electron to the mass of the proton, $\mu = m_e/m_p$. The rotational and vibrational transitions have different scalings with this constant.

$$v_{rot} \sim \frac{m_e}{\mu} R_\infty \tag{1.1}$$

$$v_{vib} \sim \sqrt{\frac{m_e}{\mu}} R_\infty \tag{1.2}$$

Molecules are well suited for testing the time dependence of μ by comparisons of a rovibrational transitions. The time variation in μ has a fractional change with a lower bound of 10^{-16} per year [47]. Progress in this direction is rapid with recently reported rotational spectroscopy of HD^+ with a fractional uncertainty of around 10^{-9} [69]. The creation of ultracold neutral molecules [24–26] for studies of fundamental constants and condensed matter physics shows the broad interests in the molecular physics community, however the control afforded by ion traps make molecular ions competitive this endeavor.

Alkaline earth hydride molecular ions are attractive for high precision studies since the vibrational splitting is large and negates the need for vibrational cooling. For these molecules, the Stark and Zeeman shifts mostly cancel each other and the second order Doppler shift dominates the error, but can be mitigated to below 10^{-17} for molecular ions below a millikelvin [70]. For high precision measurements, single molecular ions are

preferable to Coulomb crystals due increased micromotion in the latter. While resonance enhanced dissociation experiments are easily implemented, non-destructive methods eliminate systematic errors caused by reloading as well as allowing efficient and rapid measurements for the collection of large enough samples to attain a large signal to noise ratio.

Fluorescence measurements of a one photon transition in a single molecular ion is not practical due to the limited collection efficiency that would hardly distinguish the signal from background counts. In contrast, the fluorescence of the atomic ion is routinely measured after implementing quantum gates [71]. Quantum logic techniques were extended to a dark and a bright ion pair to measure a transition in Al^+ through Hg^+ [72]. In this scheme, a photon absorbed in a narrow clock transition is mapped to a logic atomic ion-which scatters many detectable photons- through a frequency dependant optical dipole force that excites the motion of the trapped atomic-molecular ion pair. Quantum logic techniques have been extended to non-destructively measuring the rovibronic transitions of MgH^+ [73]. This is extendable to CaH^+ with the recent measurement of rovibronic transitions[12]. A variation of the technique was used in coherently manipulating the rotational state of CaH^+ and observing Rabi flopping and Ramsey fringing using far-off-resonant laser. This is advantageous in that the laser is not particular to any molecular ion and should be extended to other species. One concern in the context of high precision is the high power required for far detuned lasers risks unintended scattering errors [74]. Both experiments, however, demonstrate the progress towards full control of molecular states and techniques needed for high precision measurements that can be implemented on polyatomic species [75].

Beyond measuring the time variation of physical constants, precision measurements of transitions in chiral molecules may indicate parity violations that have impacts in fundamental physics. Charge, parity, and time reversal symmetry (CPT) is thought to be the fundamental symmetry, however, any element or combination of two may be broken.

Parity violation was predicted [76] and observed in the β decay of Cobalt-60 [77]. The interaction of the electrons and nucleons may result in an enantiomer specific shift of internal energy levels. The state-selective enantiomeric purification [78] demonstrates progress towards high precision enantiomer specific spectroscopy in Coulomb crystals [75]. Beyond testing fundamental physics, measuring hypothetical spectral lines with chiral signatures in space may provide an indication of extraterrestrial life and may provide answers in biochemical homochirality [79, 80].

1.2 Contributions of the thesis

The details of ion trapping, laser cooling, and sympathetic cooling are given in Chapter 2. Chapter 3 outlines the experimental methods employed in the spectroscopy of CaH^+ including the vacuum systems, optics, imaging, lasers, and control systems. Chapter 4 discusses the measurement of vibronic transitions in CaH^+ and the deuterated isotopalogue that reveal the need to include electron correlation in **ab initio** calculations of even a relatively simple molecule. To summarize the experiment, a frequency doubling a mode-locked Ti:Sapph laser allowed for the measurement of four vibronic transitions ($1^1\Sigma, v = 0 \rightarrow 2^1\Sigma, v' = 0, 1, 2, 3$) using resonance enhanced photodissociation. These were initially assigned to the $1^1\Sigma, v = 0 \rightarrow 2^1\Sigma, v' = 1, 2, 3, 4$ based on MS-CASPT2 calculations [81] but spectroscopy on the deuterated isotopologue supported reassignment [11]. The bandwidth of the frequency doubled laser was too broad to resolve rotational transitions, so pulse shaping was used to spectrally narrow the probe beam to obtain rotational resolution of the $1^1\Sigma, v = 0 \rightarrow 2^1\Sigma, v' = 0, 1, 2, 3$ transitions as discussed in chapter 5. These transitions will allow tests of rotational cooling techniques such as optical pumping or cooling with a cloud of laser cooled K atoms. Pulse shaping demonstrated here, may be extended to the rotational cooling of molecular ion with nearly diagonal Franck-Condon factors such as BH^+ by removing blue frequencies of a broad bandwidth laser that drive R branch transitions. The diagonal nature should also allow

direct Doppler cooling, the observation of transitions by direcly imaging fluorescence, or efficiently measuring the heating of a molecular-atomic ion pair by quantum heating spectroscopy. A reaction chamber for producing this molecular ion is discussed in chapter 6. Finally, the possibility of non-destructive measurements of CaH^+ by quantum logic techniques as well as possible rotational cooling techniques such as optical pumping is discussed in the conclusion.

CHAPTER 2

ION TRAPPING AND LASER COOLING

2.1 Ion trapping

Ion trapping involves creating a confining force applied to charged particles by manipulating the electric potential. Earnshaw's theorem shows that no static potential will be suitable since $\nabla^2 V = 0$ in free space. However, a time varying potential will allow stable confinement. As a simple example, the equations of motion for a charged particle in a parallel plate capacitor with an applied potential $V(t) = V_0 \cos \Omega t$ (ignoring the y and z motion) shows the ion's position oscillates in between the plates (**Figure 2.1**).

$$F = m\ddot{x} = e\vec{E} = eE_0 \cos \Omega t \tag{2.1}$$

where $E_0 = \frac{V_0}{d}$ for the plate separation, d. An *ansatz* solution is $x(t) = A \cos \Omega t$. Substituting back into the equation of motion gives

$$A = \frac{-qE_0}{m\Omega^2}. \tag{2.2}$$

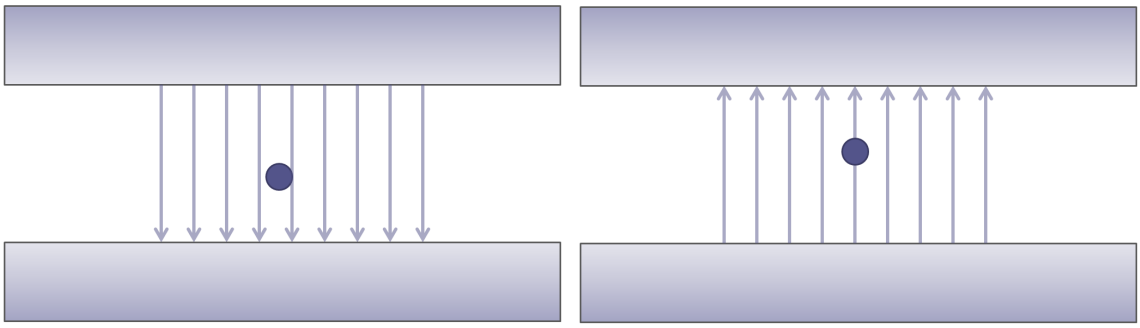

Figure 2.1: A positive charge in a two dimensional homogeneous oscillating electric field.

This solution shows that the ion oscillates with a micromotion frequency proportional to the applied field with the position 180° out of phase. For this case with the homogenous field, the time average force is zero. For a slightly inhomogenous field, as an example where the capacitor plates are curved such that the field is weaker on one side, there is a time averaged force. The equation of motion is the same as before, with a corrective term, $E' = \frac{d\vec{E}}{dx}$, proportional to the displacement along the x direction added to account to the inhomogeneity

$$\vec{E}(x,t) = (E_0 + E'x)\cos\Omega t. \tag{2.3}$$

For small inhomogeneities, the solution is approximately the same:

$$x(t) \approx \frac{-eE_0}{m\Omega^2}\cos\Omega t. \tag{2.4}$$

In other words, the micromotion is not affected. The force at any instant is

$$F = e(E + E'x)\cos\Omega t. \tag{2.5}$$

Averaging over time results in a nonzero net force,

$$\langle F\rangle = \langle eE_0\cos\Omega t\rangle + \langle eE'x\cos^2\Omega t\rangle. \tag{2.6}$$

The first term averages to zero. Using the approximate solution of $x(t)$ gives the time averaged force,

$$\langle F\rangle = \langle -\frac{eE'E_0}{m\Omega^2}\cos^2\Omega t\rangle = -\frac{eE'E_0}{2m\Omega^2}, \tag{2.7}$$

where the ion still experiences a fast driven micromotion, but a slower secular motion is superposed due to this time averaged force in an inhomogenous field. Extending this to

three dimensions, a practical inhomogenous field is created from a quadrupole potential,

$$V = \frac{V_0}{2r_0^2}\alpha x^2 + \beta y^2 + \gamma z^2. \tag{2.8}$$

The Laplace condition requires $\nabla^2 V = 0$, hence $\alpha + \beta + \gamma = 0$. For a cylindrically symmetric configuration, $\alpha = 1 = -\beta$, $\gamma = 0$ and the potential is

$$V = \frac{V_0}{2r_0^2}(x^2 - y^2). \tag{2.9}$$

The electric field ($\vec{E} = -\nabla V$) produced by the configuration has the components:

$$E_x = -\frac{V_0 x}{r_0^2} \tag{2.10}$$

$$E_y = \frac{V_0 y}{r_0^2} \tag{2.11}$$

$$E_z = 0. \tag{2.12}$$

A charge injected along the z axis will oscillate in the x direction, but will be deflected towards the y direction. In order to prevent deflection, an oscillating potential may be used, as in the 1 dimensional example,

$$V_0 = U + V\cos\Omega t. \tag{2.13}$$

Here, U is an offset voltage to 'float' the trap, and V is the amplitude of the oscillating voltage.

The equations of motion become:

$$F_x = m\ddot{x} = qE_x = -\frac{qV_0 x}{r_0^2} \tag{2.14}$$

$$F_y = m\ddot{y} = qE_y = +\frac{qV_0 y}{r_0^2} \tag{2.15}$$

$$0 = \ddot{x} + \frac{q}{mr_0^2}(U + V\cos\Omega t)x \tag{2.16}$$

$$0 = \ddot{y} - \frac{q}{mr_0^2}(U + V\cos\Omega t)y \tag{2.17}$$

These equations for a charge, e with mass, m, injected into this field can be written in the dimensionless form [82]:

$$\frac{d^2x}{d\tau^2} + (a_x + 2q_x\cos 2\tau)x = 0 \tag{2.18}$$

$$\frac{d^2y}{d\tau^2} - (a_y + 2q_y\cos 2\tau)x = 0, \tag{2.19}$$

with

$$a_x = a_y = \frac{4\kappa eU}{mr_0^2\Omega^2} \tag{2.20}$$

$$q_x = -q_y = \frac{2eV}{mr_0^2\Omega^2} \tag{2.21}$$

$$\tau = \frac{\Omega t}{2}. \tag{2.22}$$

κ is a constant geometric factor. r_0 is half the distance between diagonally opposed rod electrodes. U is typically set to zero in experiments discussed in this thesis in order to trap a wide variety of masses.

These Mathieu equations have analytical solutions $x(\zeta)$ that are either periodic and unstable or periodic and stable. The analytic solutions to the equations are discussed in

depth elsewhere[83–85], but briefly Floquet's theorem assumes a series solution of the form:

$$x(\zeta) = Ae^{\mu\zeta} \sum_{n=-\infty}^{\infty} C_{2n} e^{i2n\zeta} + Be^{-\mu\zeta} \sum_{n=-\infty}^{\infty} C_{2n} e^{-i2n\zeta}. \tag{2.23}$$

C_{2n} and μ depend on the parameters a and q. Stable solutions exists when x remains finite as ζ spproaches infinity. When μ is purely imaginary, $\mu = i\beta$ for an integer β, the solution is stable and oscillatory. Else, the ion is not stably bound. For $\beta = 0$ and $\beta = 1$ respectively, the bounds of the lowest stability region is approximated with the following relationships between a and q

$$a = -\frac{1}{2}q^2 + \frac{1}{128}q^4 - \frac{29}{2304}q^6 + ... \tag{2.24}$$

$$a = 1 - q - \frac{1}{8}q^2 + \frac{1}{64}q^3 - \frac{1}{1536}q^4 ... \tag{2.25}$$

These were used to produce the stability diagram show in **Figure 2.2**. The RF frequency and amplitude are chosen to stably trap the ions in the radial (x-y) direction. Additional DC potentials are used to confine the ion along the z-axis and compensate for stray fields.

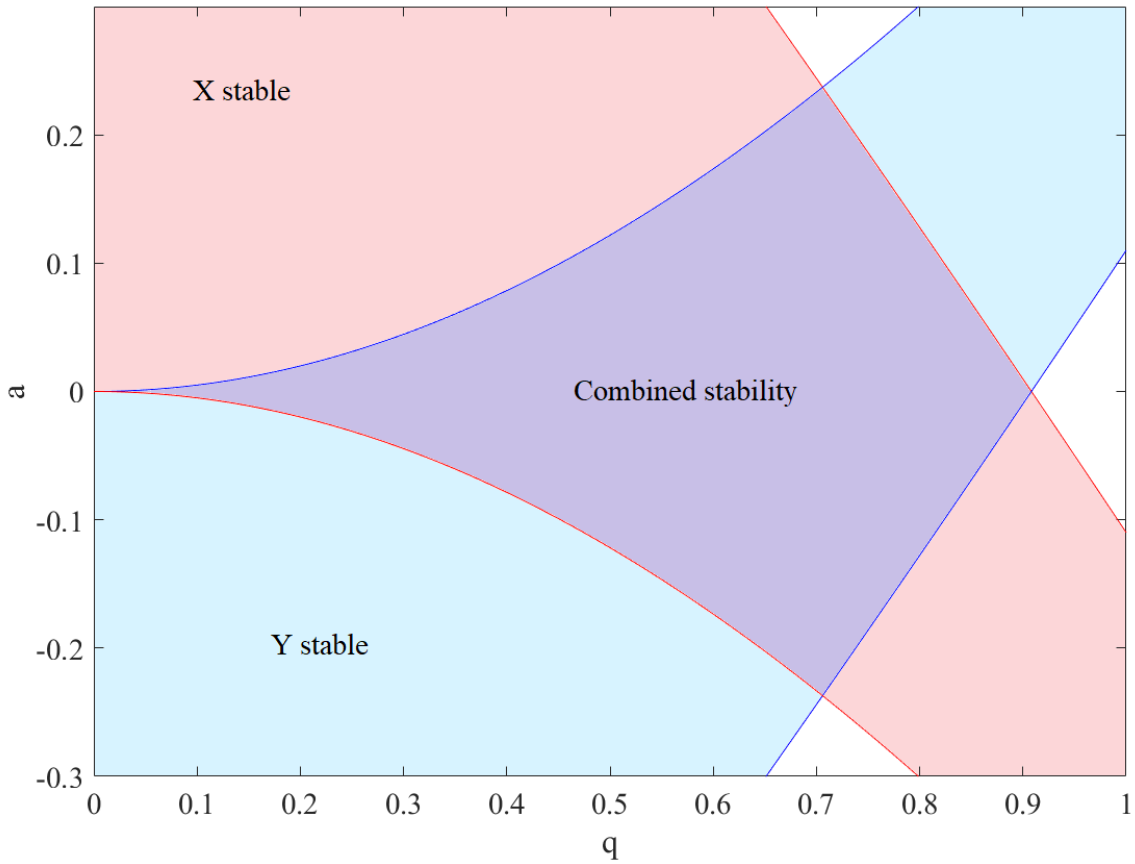

Figure 2.2: The stability diagram for β_x and $\beta_y = 0, 1$ showing stable trapping regions for the x, and y axes. The ions are confined between $0 \leq q \leq 0.9$ for $a = 0$. Lower q values are typically preferred to confine ions near the trap center to minimize micromotion [83]. Ca^+ is typically trapped at a q value of 0.2

With a low Mathieu $q < 0.4$, the ion's position changes little in the period of an RF cycle, its motion can be decomposed into micromotion driven at the trapping frequency and a slower secular motion due to the inhomogenous field that can be described by an effective pseudopotential,

$$\Phi = \frac{1}{2}m(\omega_z^2 z^2 + \omega_r^2 r^2). \tag{2.26}$$

In this regime, the RF driven micromotion can be separated from slower driven secular frequencies ω_z and ω_r [86].

$$\omega_z = \frac{1}{2}\omega_{RF}\sqrt{a} \tag{2.27}$$

$$\omega_r = \frac{1}{2}\omega_{RF}\sqrt{\frac{1}{2}(q^2 - a)} \tag{2.28}$$

The micromotion ideally vanishes at the trap center and is in practice minimized by using DC electrodes to compensate for stray fields that pull the ions out of the RF null. The pseudopotential is proportional to the charge to mass ratio and, for a fixed charge, heavier ions are more weakly confined. Multiple ions can be trapped in this pseudopotential with heavier ions forming a shell around the atomic ion and lighter ions being trapped in the core. When the potential energy between the ions is significantly larger than their kinetic energy, a lattice-like structure called a Coulomb crystal forms. The transition occurs in the regime given by the parameter [87, 88]

$$\Gamma = \frac{E_{pot}}{E_{kin}} = \frac{Q^2}{4\pi\epsilon_0 A k_b T} > 150. \tag{2.29}$$

The Wigner-Seitz radius, A, is the average inter-ion distance. For the typical Wigner-Seitz radius of $\approx 10\mu m$, the temperature to crystalize is about 10 mK. Reaching this regime requires laser cooling as discussed in the next section. The density of the Coulomb crystals

can be found [89],

$$\rho = \frac{\epsilon_0 V_{RF}^2}{m r_0^2 \omega_{RF}^2} = \frac{3}{4\pi A^3}. \tag{2.30}$$

Typical densities are on the order of 10^8 ions per cubic centimeter [90]. The trap depth of the psuedopotential can be estimated by

$$D = \frac{m}{2}\omega r_0^2 \tag{2.31}$$

and is typically on the order of several eV. This is well above the average kinetic energy of room temperature molecules as well as reaction energies, so reactions will create molecular ions that remain trapped. The Coulomb crystals containing mixtures of atomic and molecular ions have structures that can be simulated by molecular dynamics as a method for determining the number of ions in an imaged crystal e.g. in detecting the ions lost in a dissociation measurement [21, 22, 64]. Molecular ions can be co-trapped and sympathetically cooled in a Coulomb crystal [91]. The cooling efficiency is optimized for molecular ions of similar mass with the atomic coolant. Alternatively, higher charged heavy ions can be efficiently cooled with lighter atomic ions [19]. In this thesis, CaH^+ is formed by the reaction of Ca^+ with H_2 and is co-trapped in the Coulomb crystal. The molecular ions accumulate on the outer edge of the crystal because the higher mass.

2.2 Laser cooling

Since the first laser cooling of atomic ions [92, 93], Doppler cooling has become the workhorse for cold ion studies. Generally a hydrogen-like atom can be efficiently Doppler cooled. This includes the alkali atoms for neutrals and alkaline earth atoms for ion traps. These atoms possess strong dipole-allowed transitions that scatter many photons. For Doppler cooling, the laser is red-detuned from the transition which allows the atoms to preferentially absorb photons when moving due to the Doppler shift. The ion isotropically

emits a photon at the natural transition energy. Over millions of absorption-emission cycles per second, kinetic energy of the ion is exchanged for the energy difference in the absorbed and emitted photon. The cooling efficiency is limited by the natural linewidth of the transition, Γ. This Doppler limit (T_D) is typically 1 mK for the atomic ions and is given by the expression

$$T_D = \frac{\hbar\Gamma}{2k_B}. \tag{2.32}$$

In Ca^+, **Figure 2.3**, the $4^2P_{1/2}$ has a lifetime of 7.1 ns with a 1:18 branching ratio to decay to the metastable $3^2D_{3/2}$ (94.3 ns lifetime). A laser at 866 nm repumps the ion to the cooling cycle. With the two lasers, the Ca^+ can be cooled to about half a millikelvin. In general, molecules lack the simple level structure to scatter enough photons for laser cooling. A few exceptions exists consisting of molecules with nearly diagonal Franck-Condon factors [38, 39, 94].

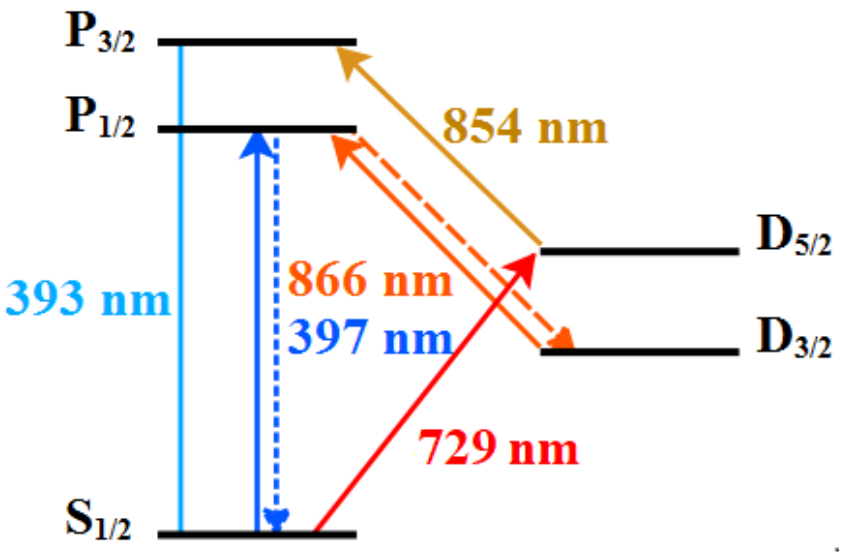

Figure 2.3: Energy level diagram of Ca^+ for laser cooling and state detection.

CHAPTER 3
EXPERIMENTAL METHODS

The experimental methods used to trap and laser cool atomic ions are discussed in detail. The vacuum system to create a well isolate environment will be discussed first with a brief summary of the methods used to get the pressure to ultra high vacuum. The trap used in the thesis is also described, but discussed in more detail elsewhere [95, 96]. The RF sources and DC controls used to trap and compensate are explained. Finally, the optical system including the Doppler cooling lasers, ion imaging setup, laser stabilization, and the spectroscopy laser are mentioned.

3.1 Molecular ion trap and vacuum system

The CaH^+ experiments use a linear Paul trap described in [95, 96]. The molecular trap is housed in a spherical octagon vacuum chamber (Kimball Physics MCF800-SphOct-G2C8) held at a base pressure of 10^{-10} torr. The pressure is low enough that collision rate is on the order of per minute, and ions can be stored for potentially days.

In general, after opening the chamber for modifications, a high temperature bake ($\approx 170^\circ$ C) is initiated while running a turbo pump. Baking continues until the pressure reaches about 10^{-6} torr. At this point, the temperature is slowly decreased and the pressure should continue to decrease about an order of magnitude as the valve connected to the turbo pump is closed. High vacuum is achieved by flashing a titanium sublimation pump for a minute every hour and using an ion pump (Varian Diode ion pump controlled by a dual ion pump controller). Hydrogen and deuterium are introduced by a manual leak valve (Kurt Lesker VZLVM267) to about 10^{-8} torr for reactions with Ca^+ in the excited $P_{1/2}$ state. The base pressure can be restored after voiding the backing line with a scroll pump.

3.2 Controls and electronics

3.2.1 RF Control and the fabrication of an RF resonator

The RF signal is generated using an AWG (Agilent AG33220ws) and amplified with a Bruker BLAX300RS amplifier. A helical resonator serves to impedance match the RF source to the trap as well as a frequency filter to select a narrow frequency range input. Construction generally follows [97].

First, inventory of available materials is acquired including the copper wire and copper tubing of various diameters. Larger gauge wire is preferred to minimize mechanical vibrations that cause fluctuations in the resonant frequency. For us, 2.4 mm copper wire was used and the quantity is denoted d_0. The turn ratio, τ is chosen to be twice d_0. Given the sizes available for the tube diameter D, the diameter of the coil, d is decided for a suitably large quality factor Q from the contour plots in [97]. Roughly, the ratio of $\frac{d}{D}$ should be less than 0.5 to minimize capacitance of the resonator. D was chosen to be 8 cm while d was chosen to be 3.5 cm. The value 3.5 was selected in part due to the availability of a form to guide winding the coil by hand. Finally, the case length, B and coil length b must be calculated.

The coil length is given by the expression:

$$b \approx \frac{C_\Sigma + K_{cd}}{K_{cs} + K_{cb}} \left(\sqrt{\frac{K_{cs} + K_{cb}}{(C_\Sigma + K_{cd}) K_{lc} \omega_0^2} + \frac{1}{4}} - \frac{1}{2} \right) \tag{3.1}$$

where ω_0 is the preferred angular frequency ($2\pi \times \Omega_{RF}$). The trap and wire capacitance, C_Σ, was measured at 4.5 pF by an LRC meter. The parameters in the above approximation are defined by:

$$K_{cs} = 39.37 \times \frac{0.75}{\log\left(\frac{D}{d}\right)} \times 10^{-12} \left[\frac{F}{m}\right] \tag{3.2}$$

$$K_{cb} = 11.26 \times 10^{-12}\left[\frac{F}{m}\right] \tag{3.3}$$

$$K_{cd} = 35d \times 10^{-12}\Big[F\Big] \tag{3.4}$$

$$K_{lc} = 39.37 \times \frac{(0.025)d^2(1-(d/D)^2)}{\tau^2} \times 10^{-6}\left[\frac{H}{m}\right] \tag{3.5}$$

For a desired frequency of 20 MHz, this comes to $b \approx 7$ cm. $B = b + D/2 \approx 11$ cm. The design of the coil support is given in the appendix and the completed coil is shown in **Figure 3.1**. The RF is applied to a small pickup coil with 2 to 3 windings and is inserted into the larger coil.

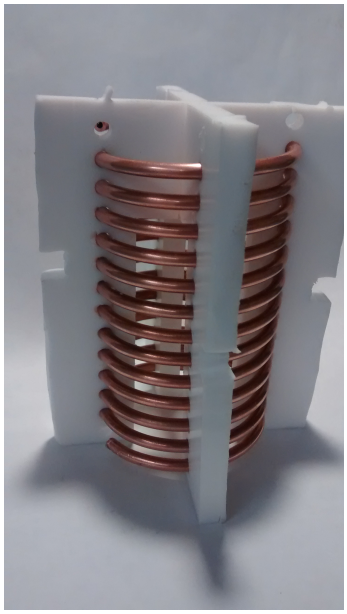

Figure 3.1: The resonator coil is supported by teflon supports and housed in a copper tube (8 cm diameter).

The resonator was built and had a resonant frequency of 17.16 MHz. The quality factor, Q was larger than 40 and the RF pickup ratio was about 23. To maximize the power into the trap, the back section of the resonator can was adjusted to minimize the reflected signal, which was sent to an oscilloscope with a directional coupler (Mini-Circuits Coupler,

ZFDC-20-5+, 0.1 - 2000 MHz). Two other resonators were also used with resonances at 19.35 MHz and 21.78 MHz. The output of the resonator is coupled to the trap by copper pin feedthroughs (Kurt J Lesker EFT0123053) with high voltage wires (Accu-Glass 112716) leading to the trap. Wires are kept the same length to prevent a phase mismatch on opposite electrodes.

3.3 DC electrode controls and ion micromotion compensation

3.3.1 The averaged-ion position compensation

For initial trapping, a cloud of ions is trapped and weakly Doppler cooled. Once the laser beam alignment and laser detuning maximizes the fluorescence, a smaller cloud is trapped and further optimized. This is repeated until a Coulomb crystal or well localized cloud is trapped. Stray electric fields pull the ion out of the RF null and drive excess micromotion. These may be due to trap asymmetries, imperfections in the machining, or patch potentials potentially generated by calcium buildup on the trap blades. Calcium has a work function is 2.9 eV, much lower than the 3.1 eV from the 397 cooling laser. It is expected that calcium coated onto the electrodes eject electrons by the cooling beam and ionization laser. The effect of stray potentials can be compensated using the DC electrodes to manipulate the position of the ion to the center RF trap. For initial compensation, the position of the ions is marked on the EMCCD display and the RF amplitude is returned to the original level. The DC electrodes, typically the center opposing two, are adjusted to position the ions to the marked position. The process is repeated until the ions no longer respond to a change in the RF amplitude.

The RF amplitude can push the ions out of the plane of focus of the EMCCD. While the center DC electrodes do have a component in that axis, DC rods lying just above and below the DC electrodes are used to more substantially position the ions normal to the imaging plane. For this, the RF is again increased and the laser is moved vertically to maximize the fluorescence. The RF is then returned to the original position and the DC voltage on

the compensation rods is adjusted to return the ions to the maximized fluorescence. By necessity of the imaging optics and laser access, the DC electrodes and compensation rods do not occupy orthogonal positions. For this reason, the process described above must be iterated until the ions no longer respond to changes in the applied RF amplitude. With compensation in the radial plane mostly optimized, compensation in the axial directions is achieved by a photon correlation method.

3.3.2 Compensation by photon correlation

When the ion is off the RF null, micromotion is induced dependent on the instantaneous field of the RF. This micromotion creates a Doppler shift [98] that manifests as a decrease or increase in fluorescence depending on the relative detuning of the cooling laser. By observing the phase relation between the fluorescence signal and the RF field, the magnitude of micromotion can be determined. When the ion is not compensated, there are some times in the RF oscillation with more fluorescence than others. The compensation rods for the radial direction and DC electrodes not including the center for the axial direction are used to flatten the response of the fluorescence to the RF at different times in the oscillation. Together, these two methods of compensation are iterated to minimize the micromotion in all the directions of the trap.

3.3.3 DC potential controls

The DC potentials are controlled on each of the 22 electrodes by a digital signal generated in LabView and converted to an analog signal with a DAC (Analog Devices Eval AD5370). The signal is amplified using op-amps (Analog Devices LT6090) and sent to the chamber through a butterworth filter. The capacitors and resistors are chosen to be compatible with the applied voltage and filter filter MHz frequencies used for trapping.

3.4 Doppler cooling lasers

The calcium ionization and cooling lasers are continuous wave (CW) external cavity diode lasers (ECDLs, Toptica DL100) that are shown in **Figure 3.2**. These diode lasers are stabilized by an external grating that feeds a frequency range to seed the diode and form a cavity. The tilt of the cavity provides adjustment of the frequency that is finely controlled by a piezo. ECDLs are generally low cost, with a large mode hope free tuning range, and sub-MHz linewidth. For Doppler cooling applications, a stability comparable to the natural linewidth of the cooling transition ($\approx$ 20 MHz) which requires stabilization to compensate for the long term drifts up to hundreds of MHz per hour.

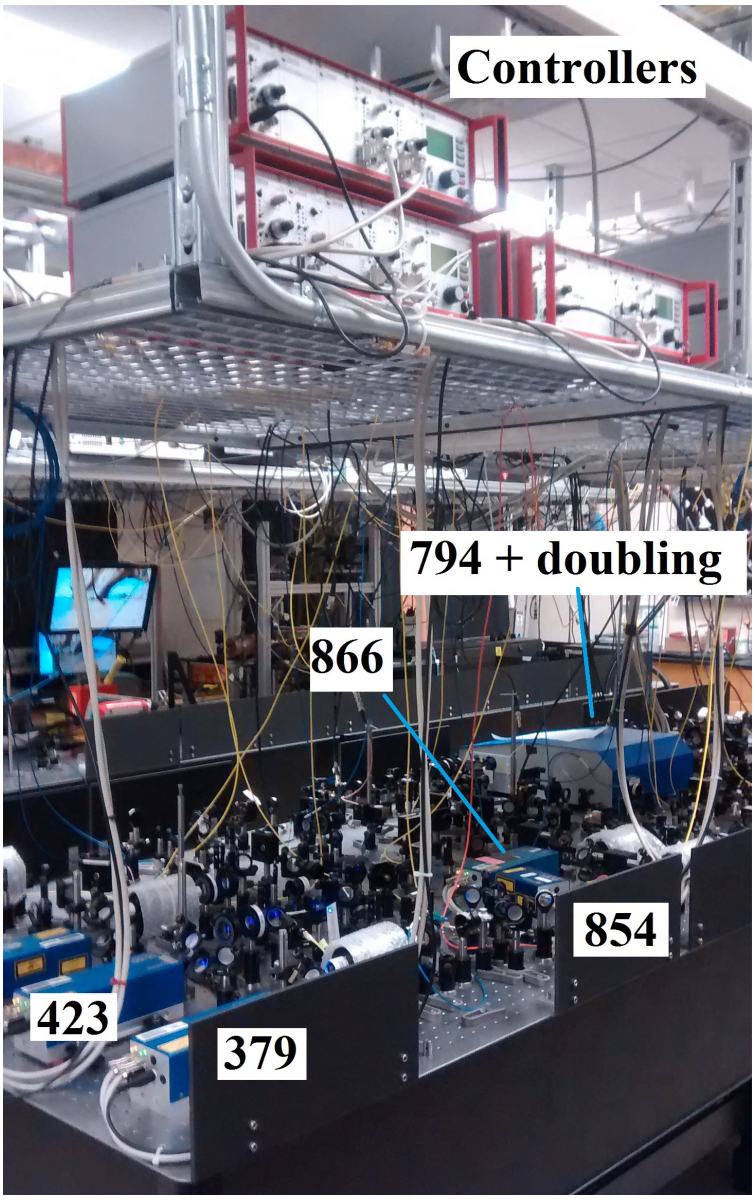

Figure 3.2: The optical table with all the lasers used for producing and Doppler cooling Ca^{+}. All values are in nm.

We use a transfer cavity to lock the lasers to a temperature stabilized HeNe (Melles-Griot). The setup is described in detail in [99], but is briefly summarized here following [100]. In this, a laser is sent into an etalon. Consecutive reflections destructively interfere unless the cavity length (L) is an integer multiple of the half wavelength (λ),

$$\frac{2L}{\lambda} = n. \tag{3.6}$$

In this case, constructive interference allows a buildup of light in the cavity, and a substantial amount of light can leak out of the second mirror. The cavity length is scanned by piezo actuators and the transmitted light as a function of the length is detected by balanced photodetectors. The change in frequency of the ECDL manifests as a change in the cavity resonance position relative to the HeNe resonance. The error signal is fed back to the diode to compensate for frequency drifts. As shown in **Figure 3.3**, three lasers are locked to the HeNe. The 397 is locked to the HeNe using a portion of the fundamental 794 nm beam.

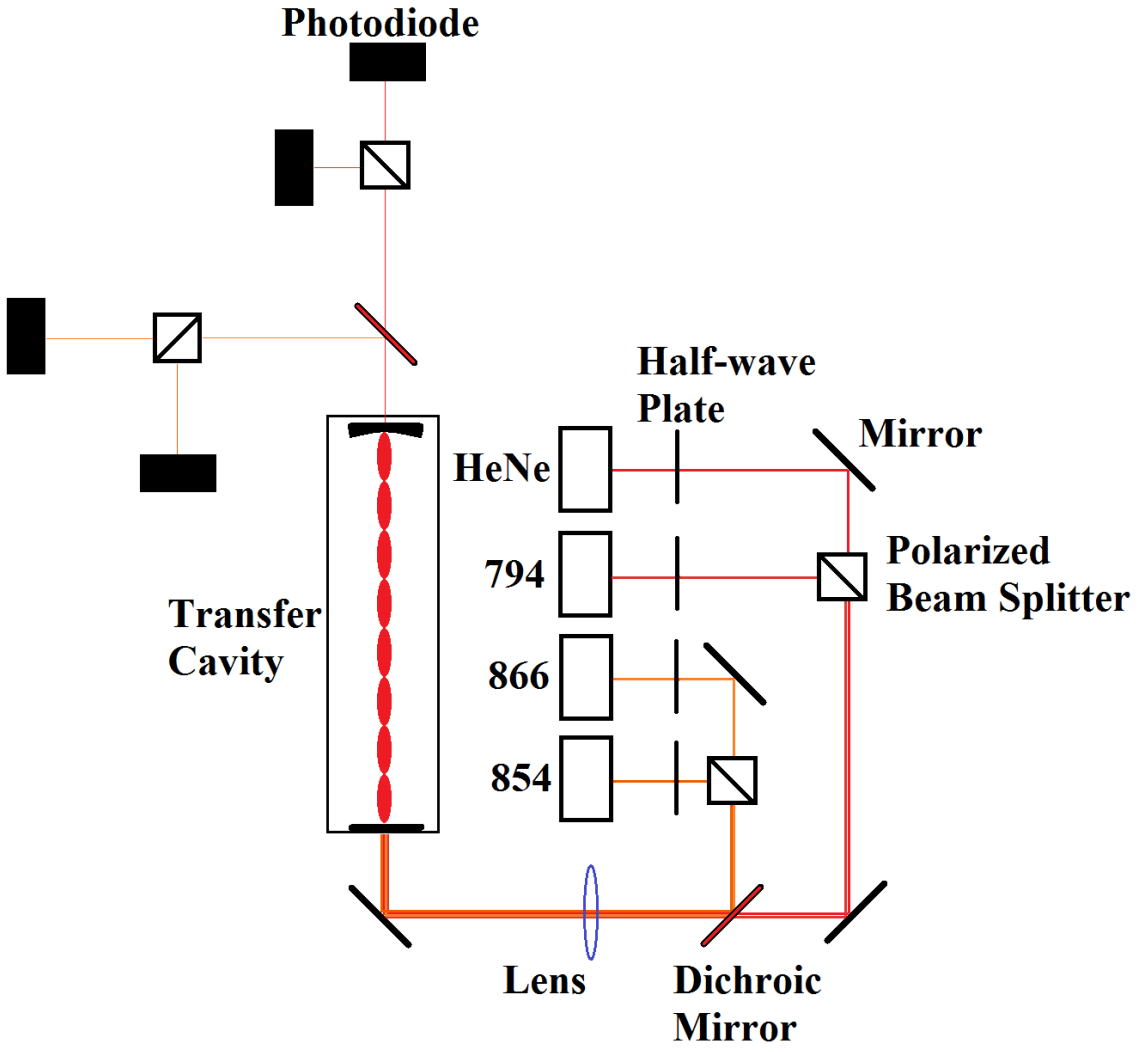

Figure 3.3: The transfer cavity setup is shown schematically. Lasers of similar wavelength are combined with a polarized beam splitter (PBS) and the two pairs are combined with a dichroic mirror (Thorlabs DMSP-805). A lens mode-matches to the cavity by focusing to the back mirror. The components of the output beam are split using a PBS and dichroic, and sent to a photodiode. The cavity itself is made of a flat and concave broadband mirrors separated by a low expansion quartz housed in a CF T-tube. The bottom arm of the T has a feed-through to send the scanning waveform to the piezos. The tube allows for mechanical isolation but is housed at ambient pressure.

Before sending the beams to the trap, an acousto-optic modulator (AOM) shown in **Figure 3.4**, is used as a fast switch and fine frequency control by applying acoustic waves with frequencies in the megahertz range. The transmitted light is Bragg diffracted into different orders that are spatially separated. The first order has a wavelength of the input beam plus the frequency of the phonon. In this way, the frequency and amplitude of the beam is controlled by the acoustic waveform. A double pass setup prevents beam misalignment during frequency changes is sent into a fiber coupler. The output of the couplers are combined and sent into the axial and radial directions of the trap as shown schematically in **Figure 3.5**.

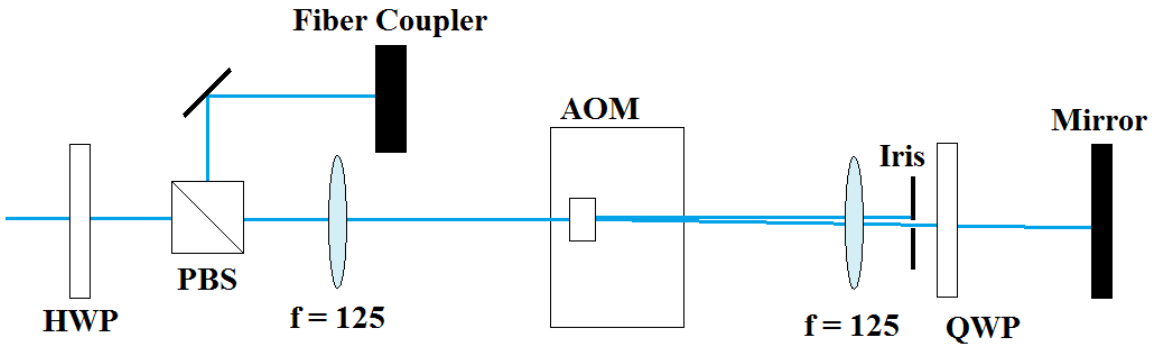

Figure 3.4: The incoming beam is sent to the AOM and focused on the crystal with a lense. A second lens after a pass through the crystal provides collimation. An iris selects the first order which is rotated twice by $\pi/4$ such that the second pass is reflected by the polarized beam splitter to the fiber coupler.

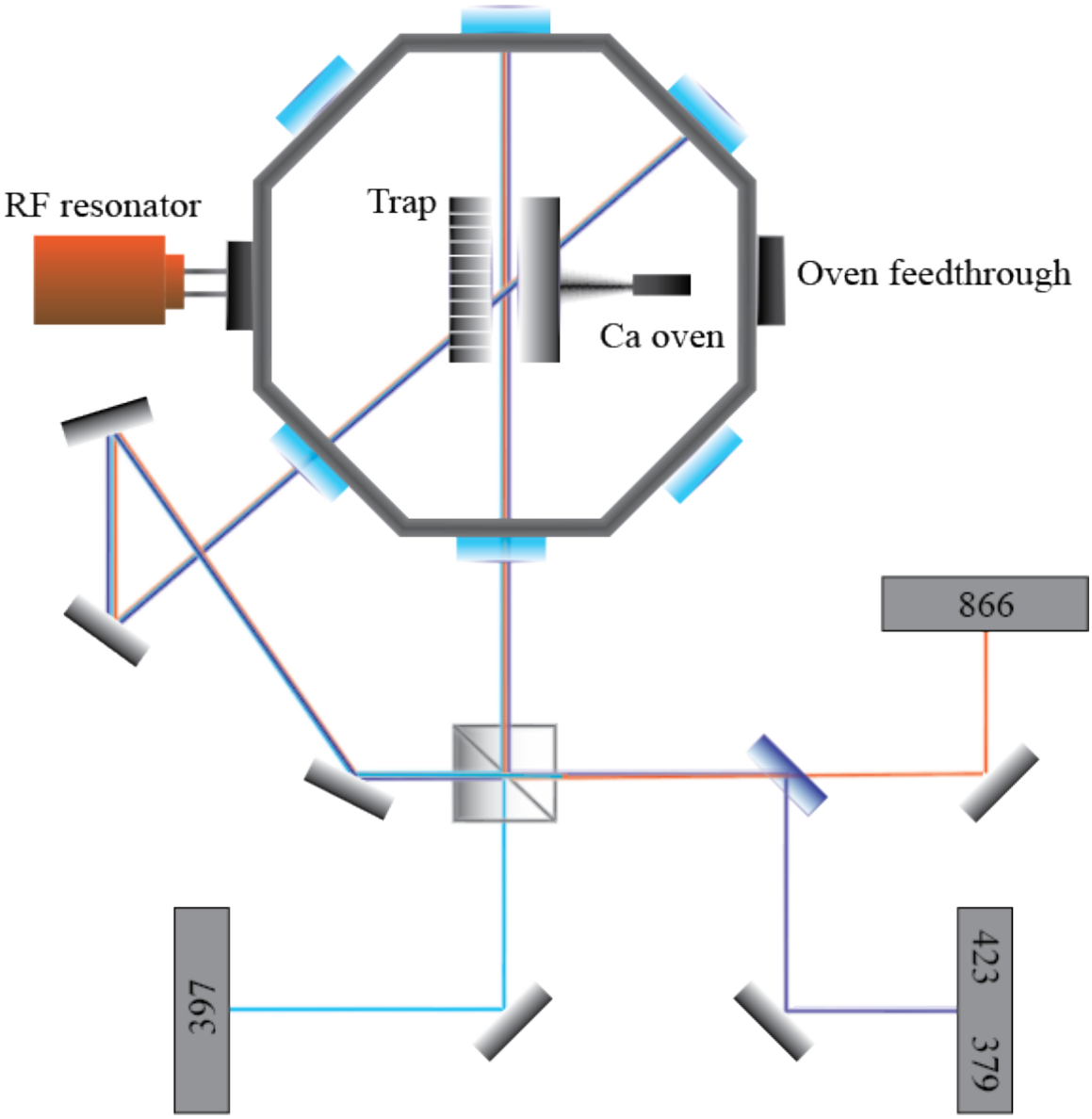

Figure 3.5: Trapping setup and cooling lasers. The calcium oven consists of a 0.1 mm stainless steel tube with a small chunck of elemental calcium. The tube is crimped on the end not pointing to the trap. Kapton-insulated wires are inserted both ends and a current is applied to sublimate the calcium.

The cooling and ionization beams are co-aligned using a dichroic and cube beamsplitter, the sent into the trap from two directions. For initial trapping, co-alignment is checked by reflecting the combined beams before any lenses to a wall several meters away. The camera is aligned close to the center of the trap by observing the reflection of a laser off the trap blades. Finally, the axial and radial beams are verified to transmit through the trap center by collimating the beam after exiting the chamber and marking the beam on a wall. The tilt of the beam is moved by the kinetic mirror until the beam is clipped by the trap. All directions are tested and provide an estimate of the trap center. The oven is then run at a current hotter than normal (typically up to 1.4 amps) to produce a dense beam of calcium atoms.

Ca^+ is generated by photoionizing a neutral beam, **Figure 3.6**, with 1 + 1' REMPI. The first 423 nm photon excites the $^1S_0$ to $^1P_1$ and a second UV photon ionizes from the excited state. The ions are Doppler cooled with a 397 nm laser scattering on the main cooling transition ($S_{1/2} \rightarrow P_{1/2}$) and an 866 nm repump beam. Ca^+ is directly imaged by detecting the 397 nm photons by an EMCCD camera (Princeton Instruments Cascade 1K) and PMT (Hamamatsu H7360-02).

The optics for collecting the fluorescence, **Figure 3.7**, consists of a lens stack with a numerical aperture of 0.25 mounted $\approx$ 60 mm above the trapping region. A micrometer allows for positioning control. A mirror is required to reflect the image to the camera horizontally mounted 260 mm away due to the limited vertical space. An iris is used to cut out background scattering from the fluorescing Coulomb crystal and a 30 mm lens is mounted 150 mm in front of the camera. The lens is translated to focus the image of the iris blades on the camera. A narrow-band filter at 397 or 423 nm is used to filter background scatter during trapping or searching for neutrals respectively. Finally, a beamsplitter allows simultaneous collection of the ion fluorescence on the camera and PMT. The setup, including all losses, has a collection efficiency on the order of 0.1 %.

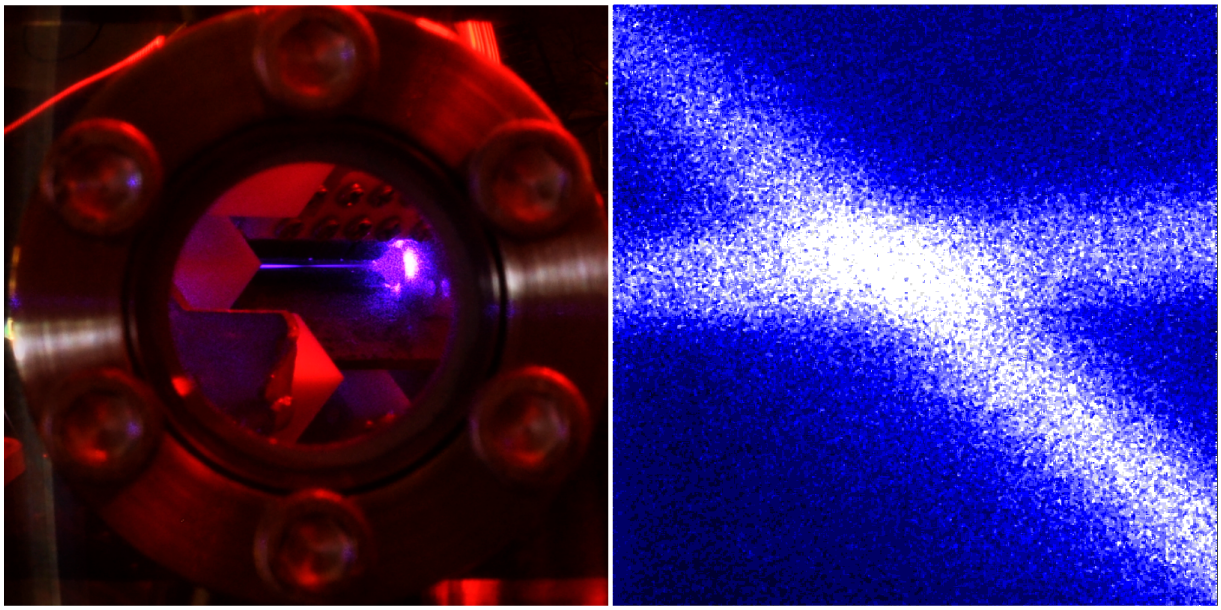

Figure 3.6: Neutrals imaged in the atomic trap with a DSLR (30 s exposure), left, and an EMCCD (300 ms exposure) on the right showing the 423 nm fluorescence. The EMCCD image shows the axial (horizontal) and radial beams.

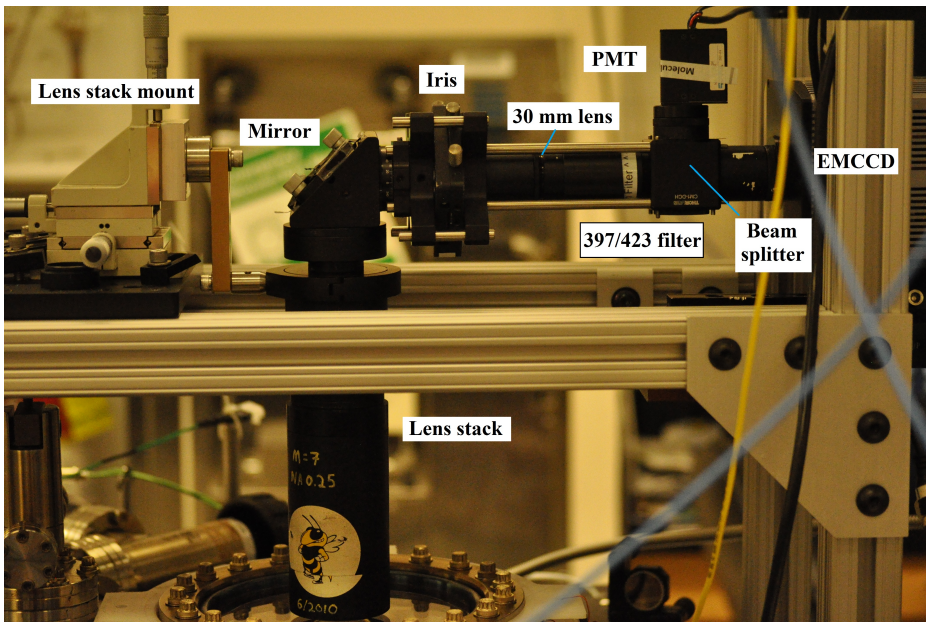

Figure 3.7: The imaging optics used in the molecular ion experiments.

3.5 Ti:sapph laser setup and pulse shaping

In obtaining the spectrum of CaH^+, we use a Coherent Mira Optima 900-F femtosecond laser. The titanium:sapphire crystal is pumped by a 15 W Verdi V10 and has a broad gain bandwidth from 680 to 1100 nm. The mirrors used in the construction of the cavity further limit the lasing bandwidth to within about 150 nm while a birefringent filter selects a narrow spectrum within this bandwidth to give a frequency range between about 700 and 980 nm. In addition to the constraint of the gain bandwidth, the cavity limits the lasing frequencies by the requirement that an integer number of half wavelengths must match the total length of the cavity. The broad gain bandwidth will allow many lasing modes. In general, these modes have random phases. The resulting output of this multimode laser is a nearly constant intensity proportional to the number of modes, N,

$$I \approx N|E_0|^2. \tag{3.7}$$

The intensity fluctuates slightly and periodically with a period of $T = 1/\Delta f$, where $\Delta f = c/2l$ for a cavity length l. When the longitudinal modes have a fixed phase relationship, constructive interference at a point in the cavity is produced periodically in time as shown for ten modes in with locked phases, **Figure 3.8**, and random phases, **Figure 3.9**. When phase locked, the resulting pulses have a peak intensity, $I \approx N^2|E_0|^2$. Phase locking is not achieved automatically. The Mira employs a passive mode locking mechanism that takes advantage of the enhanced intensity [101]. Although discussed in detail elsewhere [102], the mechanism is summarized. The high intensity pulses are self focused when traveling through the optics within the cavity due to the Kerr effect, a nonlinear change in the index of refraction due to a distortion of the electron configuration caused by the intense electric field. This self focusing only occurs for the high intensity when the laser is phase-locked. A slit before one of the cavity mirrors attenuates the beam when the laser is not phase-locked, but allows the Kerr focused beam to pass when the laser is phase-locked. Perturbing the

cavity length initiates the phase-locking by inducing an instantaneous power fluctuation to cause Kerr focusing. Once initiated, the phase-lock is self sustaining.

The pulses resulting from phase locking have a temporal and spectral widths inversely proportional to the number of modes by the equations:

$$\Delta t = 2\pi/N \tag{3.8}$$

$$\Delta\omega = 1/N\Delta f. \tag{3.9}$$

In this case, the laser produces a pulse width of about 200 fs. The intensity enhancement while pulsing is advantageous for frequency doubling to reach the predicted vibronic transitions of CaH^+. The doubling crystal introduces a chirp that expands the temporal pulse width to about 300 fs or about a 4 nm spectral width. This spectrally broad laser, with a sample profile shown in **Figure 3.10**, aided the initial search for the vibronic transitions since the bandwidth matched the bandwidth of the vibronic transition. In other words, all the rovibronic transitions would be expected for the rotational levels populated at 300 K are covered by the laser. To resolve these rovibronic transitions, pulse shaping was used to spectrally narrow the probe laser.

Femtosecond pulse shaping [102, 103] generates a desired optical waveform by decomposing a pulsed laser into its spectral components and uses a spatial mask tailored to modulate the phase or amplitude in the Fourier plane. The basic idea is that in the time domain, a filter is modeled by the response function $h(t)$. For an input pulse, $e_{in}(t)$, the output of the filter is described by the convolution.

$$e_{out}(t) = e_{in}(t) * h(t) = \int dt' e_{in}(t')h(t-t') \tag{3.10}$$

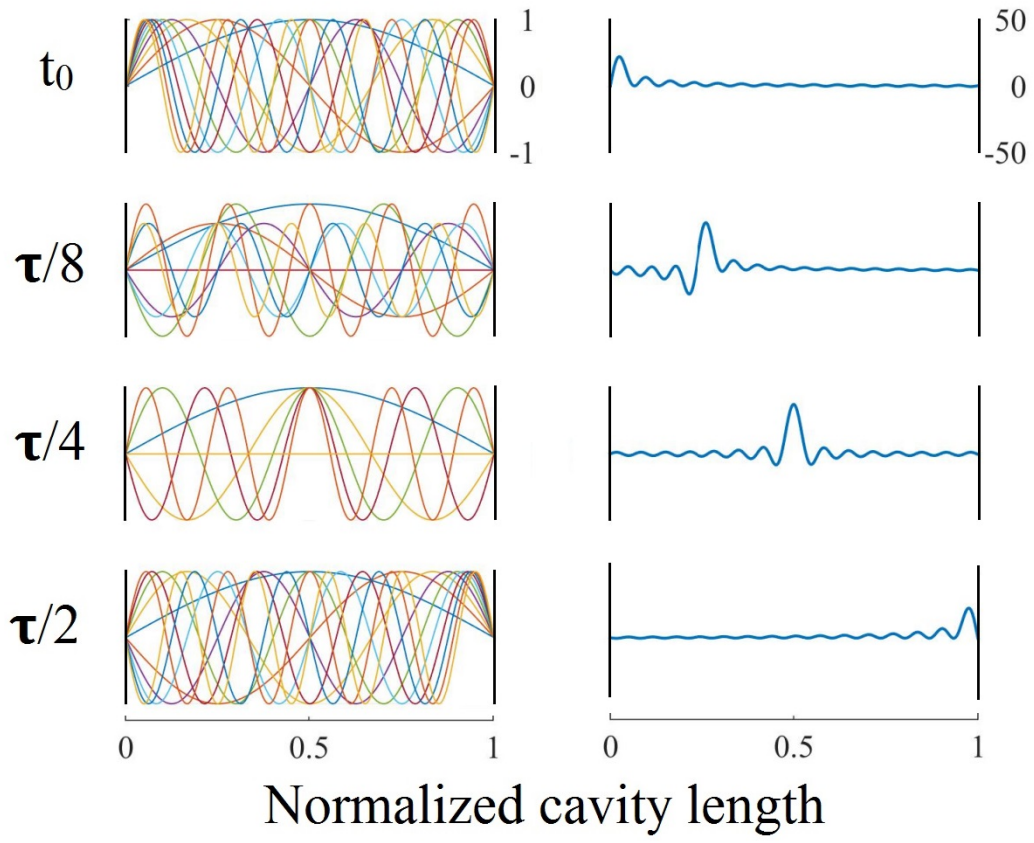

Figure 3.8: Ten modes in the cavity are shown on the left with constructive interference of thirty modes shown on the right. The position of the constructive interference changes with time. This pulse oscillates between the cavity mirrors with a repetition rate set by the time it takes for the light to transverse the cavity, $\Delta\tau = 2L/c$. The Ti:sapph we use has a repetition rate is 76 MHz. The Y axis is the normalized electric field.

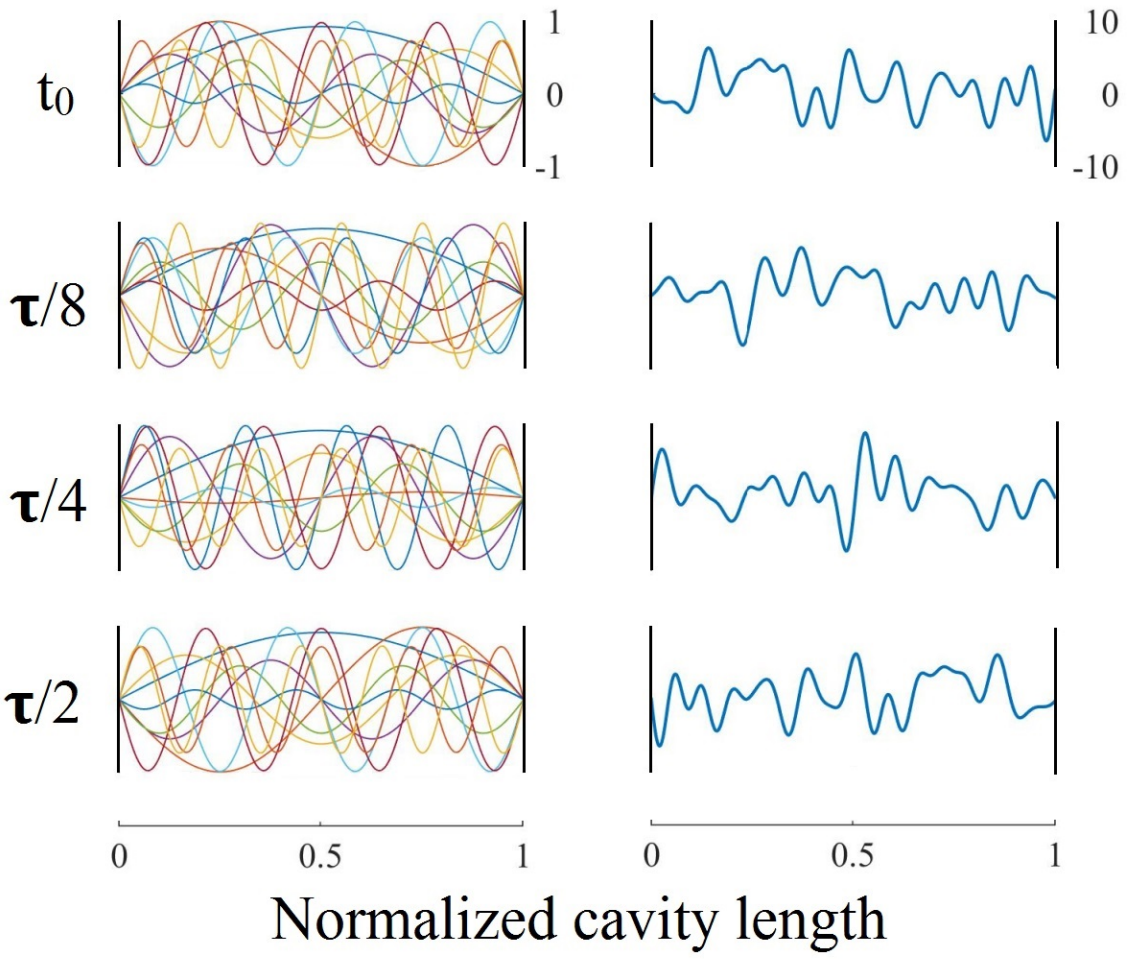

Figure 3.9: The same modes in **Figure 3.8** but with random phases showing a near CW intensity with random fluctuations.

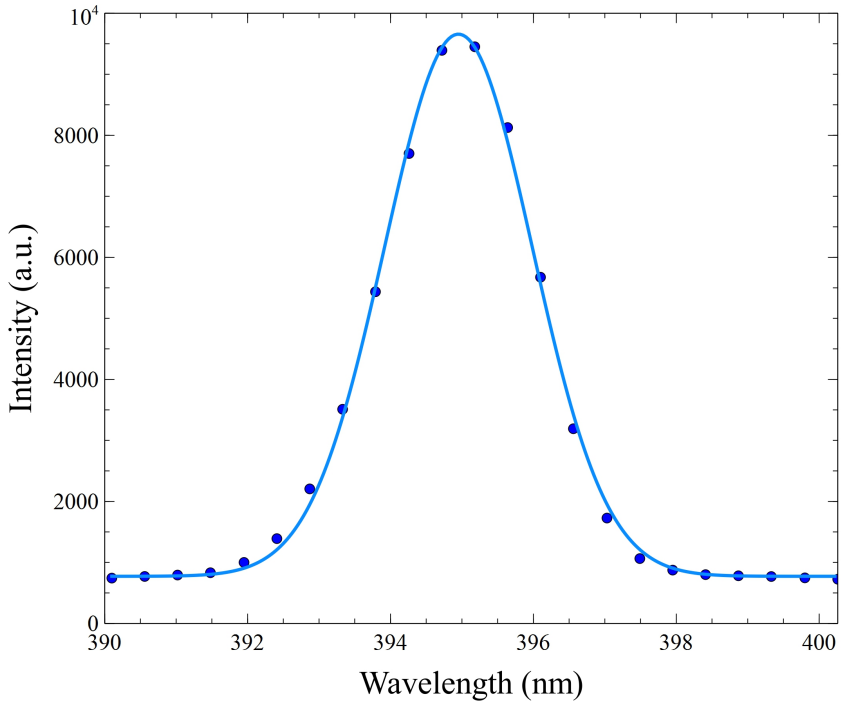

Figure 3.10: The spectral profile of the frequency doubled Ti:sapph beam

The Fourier transform of this equation gives the output pulse in the frequency domain.

$$E_{out}(\omega) = E_{in}(\omega)H(\omega) \tag{3.11}$$

For a fast input pulse, $e_{in}(t) \approx \delta(t - t')$. The output in the frequency domain is simply the frequency response of the filter, $H(\omega)$. By switching to the frequency-domain, choosing a mask with the desired frequency response becomes simpler than manipulating the pulse directly in the time domain. The 4-f pulse shaper is used to manipulate a pulse in the frequency domain.

Figure 3.11 shows the basic setup also known as a 4-f pulse shaper. A beam with spatial size w_i is sent to a grating. The grating performs angular dispersion of the frequency components of the beam. A lens performs a Fourier transform to convert angular dispersion. At the Fourier plane, a spatial mask modulates the amplitude or phase of any desired component. The Fourier transform of the mask results in the output of the

pulse shaped beam when the spectral components are recombined [103]. In this case, a spacial slit acts as the mask and creates a tunable frequency filter. In the case that the mask is absent, the output beam should ideally equal the input beam. Dispersion from the first grating and the lens causes this not to be the case. To compensate, a 'telescope' configuration by adding another lens and grating, hence the 4-f setup. In order to simplify the setup, a mirror is positioned just behind the mask to send the beam through the first lens and grating. To test the 4-f setup is dispersion free, the 397 beam was collimated and sent into the pulse shaping setup. Since it is a CW beam with a narrow linewidth, a spatially narrow diffraction limited band is observed at the focus of the first lens. This is where the slit was positioned. Fine tuning of the mirror position allowed the optimization of the outgoing beam until it spatially matched the incoming beam.

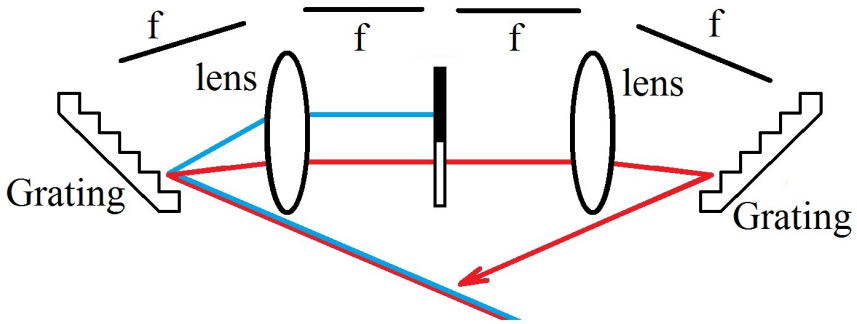

Figure 3.11: The 4-f setup showing the masking of the blue components of the spectrum. A modification used in our experiments uses a mirror behind the mask to negate the need of the extra lens and grating while compensating for dispersion.

At the Fourier plane, any frequency component with wavelength λ has a spot size given by [102]:

$$w_0 = \frac{\cos\theta_{in}}{\cos\theta_d}\frac{\lambda f}{\pi w_{in}} \tag{3.12}$$

where c is the speed of light, and θ_d and θ_{in} are the dispersed and incident angles from

the grating. In our near-Littrow configuration, $\theta_d \approx \theta_i$. The full width half max (FWHM) spectral resolution is estimated by the following:

$$\delta v = \sqrt{ln(2)}\frac{w_0}{\alpha} = \sqrt{ln(2)}\frac{\cos\theta_{in}}{\pi w_{in}}\frac{cd}{\lambda} \tag{3.13}$$

for a grating with grating period, d. Decreasing the grating period and increasing the input beam size increases the resolution of the pulse shaping. Here, a telescope increases the beam size from about 5 mm to nearly 20 mm. The size was limited by the available optics and the grating period was 3600 groves per mm. For a wavelength centered at 400 nm, the expected resolution is about 0.086 cm^{-1}. In practice, the resolution was limited by the minimum slit width possible without causing spatial diffraction. For mask features, $x > w_0$, the pulse shaping resolution is estimated [104]:

$$\delta v = \sqrt{ln(2)}\frac{x}{\alpha} = \sqrt{ln(2)}\frac{\cos\theta_{in}}{\pi w_{in}}\frac{xcd}{\lambda^2 f} \tag{3.14}$$

For a slit width of 76μm, the expected resolution is 2 cm^{-1}. Our resolution is limited by the spectrometer reading with the method for estimating the frequency discussed in **Chapter 5**.

CHAPTER 4

VIBRONIC SPECTRUM OF SYMPATHETICALLY COOLED CaH^+ AND CaD^+

4.1 Introduction

The chapter is based on the following articles:

R. Rugango, **A. T. Calvin**, S. Janardan, G. Shu, and K. R. Brown. "Vibronic spectroscopy of sympathetically cooled CaH^+". ChemPhysChem **17** 22 (2016), pp. 3764–3768.

J. Condoluci, S. Janardan, **A.T. Calvin**, R. Rugango, G. Shu, and K. R. Brown. "Reassigning the CaH^+ $1\ ^1\Sigma \rightarrow 2^1\Sigma$ vibronic transition with CaD^+". Journal of Chemical Physics **147** 21 (2017), p. 214309.

Prior to the work in this thesis, the only bound transitions measured in CaH^+ were two vibrational overtones [8]. In order to move towards non-destructive methods of state detection, such as was demonstrated on an electronic transition in MgH^+ using a walking standing wave [73], the measurement of more transitions in CaH^+ would be required. By frequency doubling the laser used in the previous measurement [8], several vibronic transitions in CaH^+ were within access with the potential for rotational resolution.

4.2 Methods

4.2.1 Experimental setup

The experiment employed a manually-tuned, frequency-doubled Ti:Sapphire laser to probe the vibronic transitions of CaH^+ and CaD^+ separately co-trapped with laser-cooled Ca^+ in a heterogeneous Coulomb crystal. A schematic of the setup is shown in **Figure 4.1**. The Ti:sapph beam is doubled with about a 10% efficiency using a 0.1 mm thick Foctek BBO crystal. A thin BBO crystal suffers lower efficiency compared to thicker crystals tested,

but is required to reduce spatial dispersion that becomes problematic when the beam is sent long distances. The doubled beam is sent to the crystal along the trap axis using the outgoing 397 or 423 beams as a guide to co-align the dissociation beam into the trap. Another check is performed by tuning the dissociation laser to 393 nm. This induces the $S_{1/2}$ to $P_{3/2}$ transition which decays to the long lived $D_{5/2}$ state. When the beam is aligned to the Coulomb crystal, the crystal goes dark or melts depending on the power of the beam.

The experiments take place in an ultrahigh vacuum chamber with a background pressure of 10^{-10} torr and the ions held in the linear Paul trap described in Section 3.1. CaH^+ is generated by reaction of H_2 with excited Ca^+ at pressures of 3×10^{-8} torr. When a suitable number of calcium ions are reacted to give a crystal similar to **Figure 4.2a**, the pulse sequence shown in **Figure 4.2b** exposes the crystal to the dissociation laser. A single pass acousto-optic modulator is used to shutter the beam. The 854 nm repump is needed when probing transitions near 393 nm. By measuring the Ca^+ fluorescence increase upon laser exposure, **Figure 4.3**, a spectrum of molecular dissociation rate was generated as a function of frequency. The frequency doubled Ti:sapph beam is scanned between 370 and 421 nm to access all predicted vibronic transitions within the lasers tuning range as shown by the *ab initio* potential curves in **Figure 4.4**. An Ocean Optics spectrometer (model HR2000+) is used to measure the center frequency. The laser has a frequency bandwidth corresponding to a 185 fs pulse width (FWHM) with a repetition rate of 76 MHz. The power of the dissociation beam is kept constant at 20 mW using a variable beamsplitter (HOLMARC HO-VBS-F100). A 175 mm lens focuses the beam to the trap center with a beam diameter of 20 μm

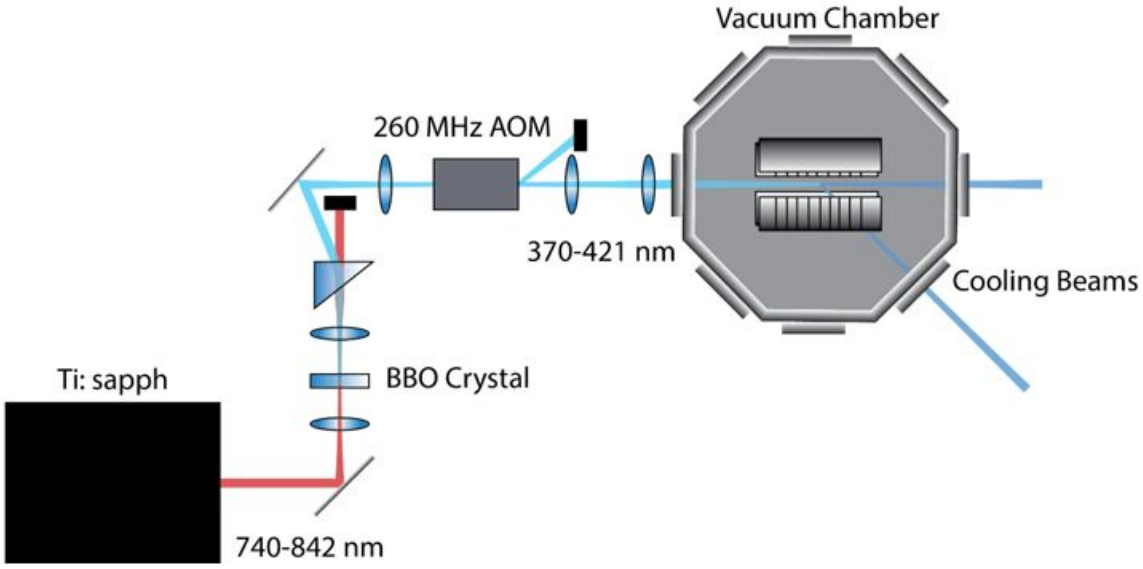

Figure 4.1: The vibronic experimental schematic of the frequency doubled Ti:Sapph beam. The fundamental is separated from the doubled beam using a prism while 20 mW of the doubled beam is shuttered by an AOM and sent into a trap. Spherical lenses are used to collimate the beam for a constant beam waist at the crystal.

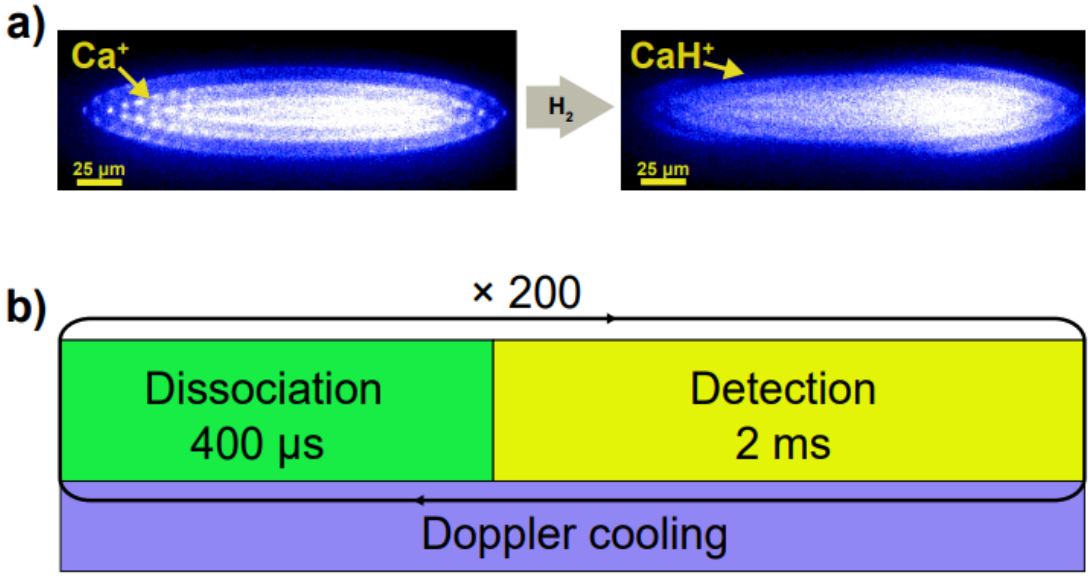

Figure 4.2: **a** The Coulomb crystal of Ca^+ darkens upon exposure to H_2 due to the formation of CaH^+, which is more stably trapped on the outer edge of the crystal. The asymmetry is due to the radiation pressure of the cooling beam on Ca^+. **b** The frequency doubled Ti:Sapph beam is turned on for 400 μs and fluorescence is detected for 2 ms. The process is repeated 200 times to obtain the fluorescence recovery curves.

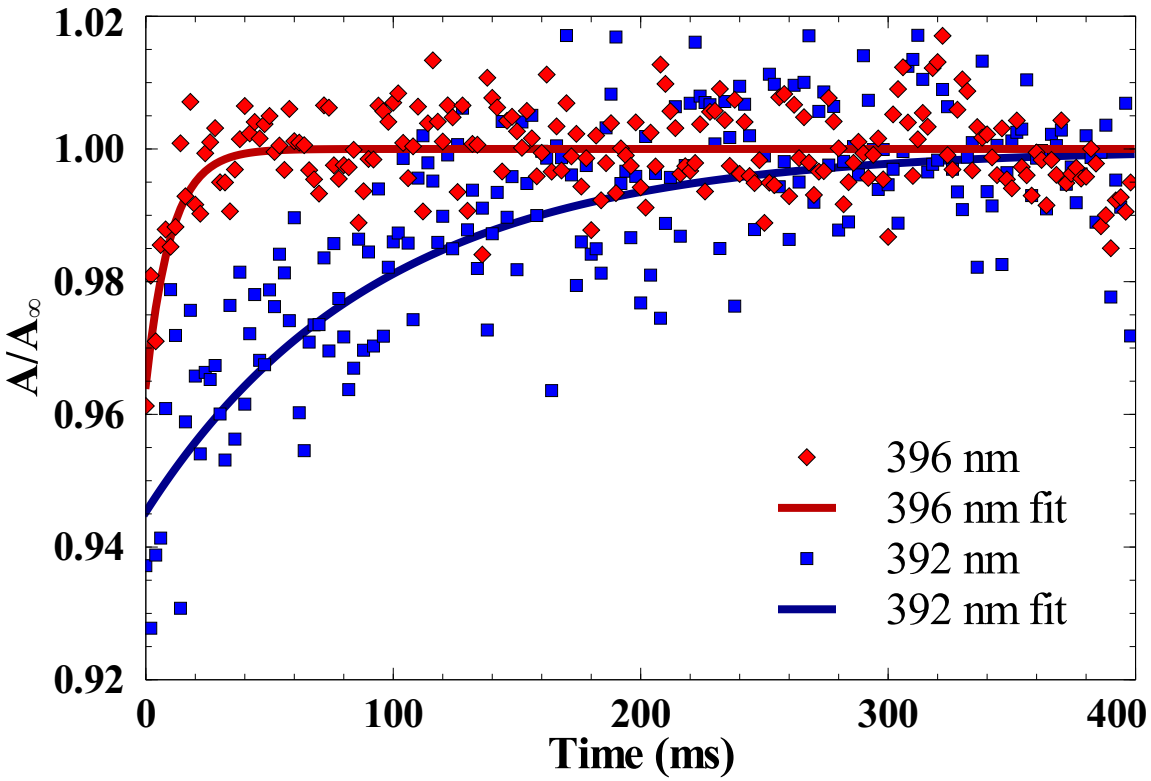

Figure 4.3: The fluorescence recovery curve for CaD^+ shows the difference in dissociation rate on and off resonance. The curve is fit to a first order model for dissociation to extract a rate as a function of laser frequency.

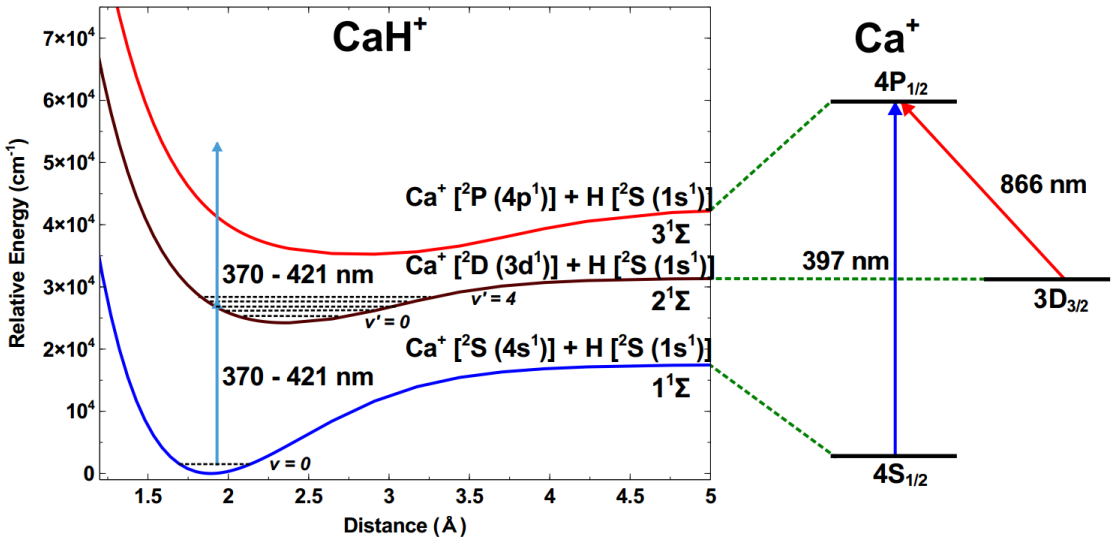

Figure 4.4: The potential energy surfaces of CaH^+ generated from *ab initio* calculations [105]. The CaH^+ begins in the ground state and is excited to the lowers four vibrational states of the electronically excited state with the range of the Ti:sapph.

Resonance enhanced photodissociation yielded the spectrum shown in **Figure 4.5**. Going solely off *ab initio* MS-CASPT2 calculations [81], the v' = 0 transition was initially labeled v' = 1 and the v' = 0 was reported as unobserved [10]. Similar unobserved lower vibrational transitions were reported for KH, however reassignment was supported by vibronic spectroscopy of KD [106–109]. Within the Born-Oppenheimer approximation, an isotope has no effect on the potential curves shown in **Figure 4.4**. The increase in the reduced mass shifts the vibrational energy levels closer and shifting the zero point vibrational energy down, as shown in **Figure 4.6**. Deviations from the Born-Oppenheimer approximations are expected to be small on the order of 10 cm^{-1} by comparison with the isoelectronic KH [107].

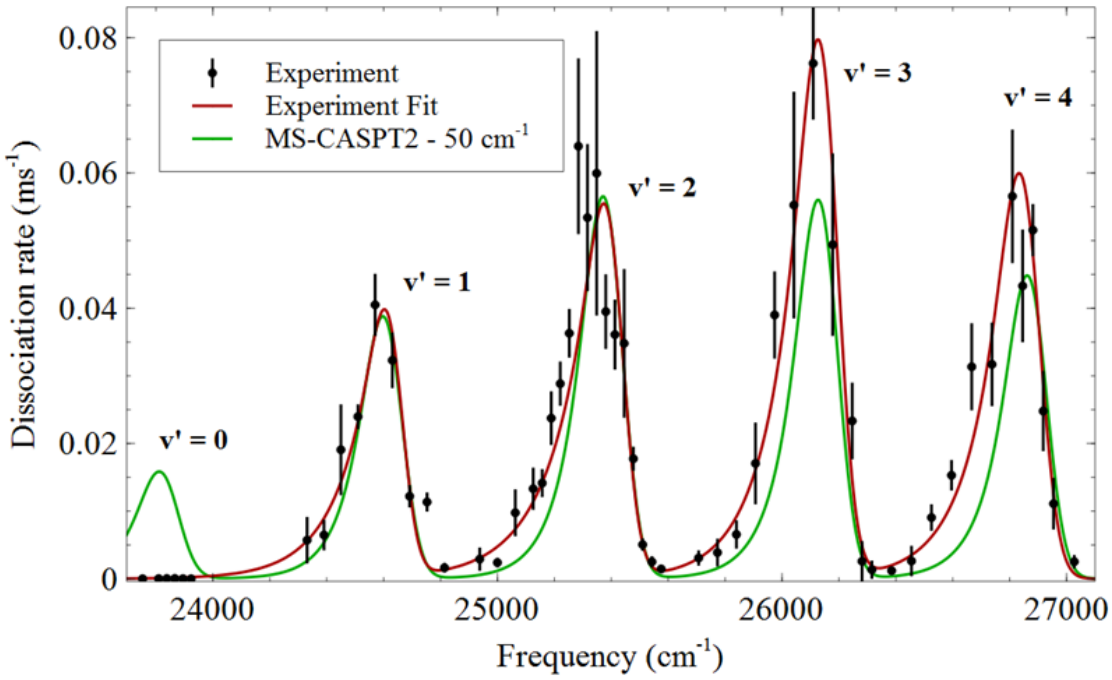

Figure 4.5: The vibronic spectrum of CaH^+ shows close agreement with *ab initio* calculations when shifted by 50 cm^{-1}, a reasonable shift based on the calculated energies of the atomic constituents at the asymptotes of the potential curve. The relative transition strengths show decent agreement with the Franck-Condon factors. Here, the red curve is an experimental fit and is compared to dissociation model in red. The model is convolution of the laser line-width and the underlying rovibronic transitions (and their relative strengths) covered by the laser. The model assumes a first order dissociation rate. However, the v' = 0 transition was not observed and prompted a study with CaD^+

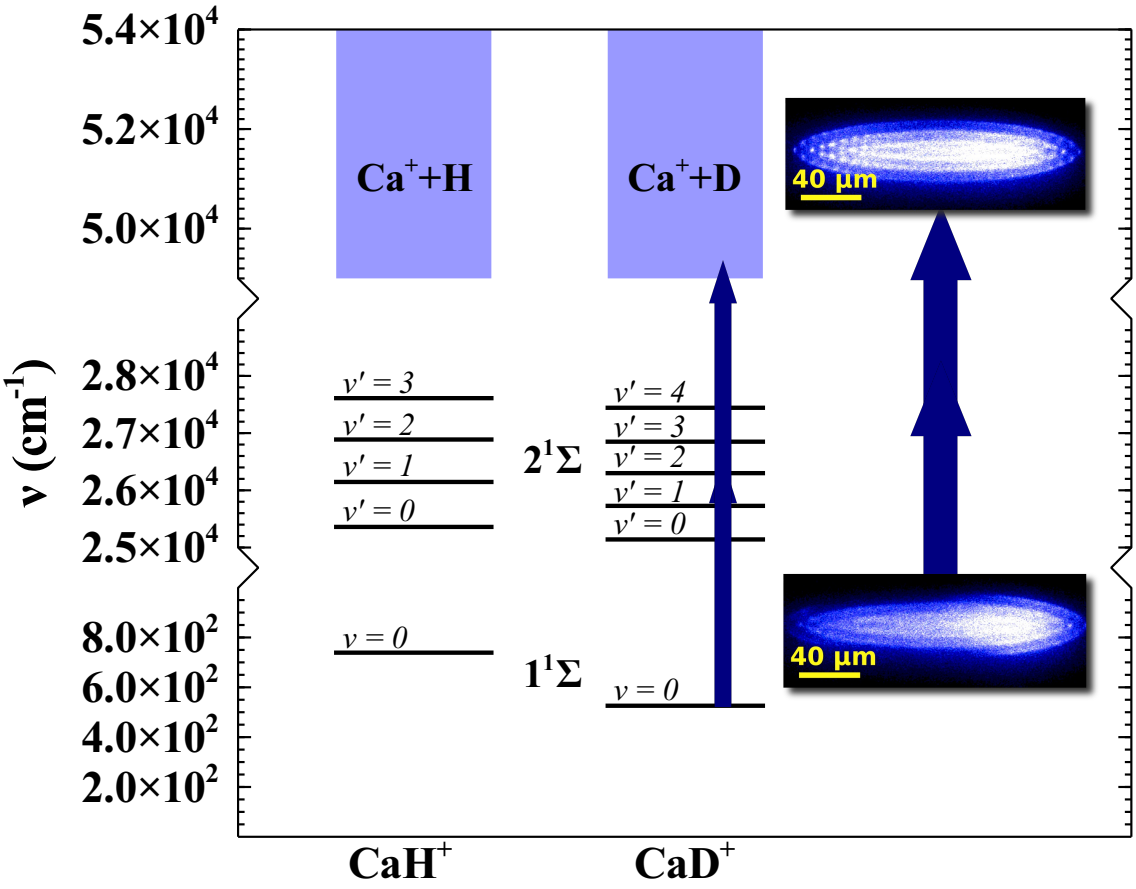

Figure 4.6: Energy level diagram of the CaH^+ and CaD^+ transitions probed by applying a doubled Ti:sapphire laser and observing photodissociation.

CaD^+ is generated by reaction of D_2 with excited Ca^+ at pressures of 5×10^{-8} to 10^{-7} torr, which is larger than the 3×10^{-8} torr used in the CaH^+ experiment. The reaction of Ca^+ with deuterium is slower due to the kinetic isotope effect so a higher pressure is required to overcome background dissociation from the cooling laser. As a result, the fluorescence recovery curves are not as consistent as with the measurements with CaH^+ and the vibronic spectrum in **Figure 4.5** does not show the expected relative transition heights from the Franck-Condon overlap like CaH^+. Nonetheless, the measured spectrum **Figure 4.7** support reassignment of the measured CaH^+ transitions as discussed in the Results and Discussion.

4.2.2 Theoretical Model for Parameter Estimation

To compare theory and experiment, CaD^+ dissociation spectra were modeled using theoretical and experimental parameters. Calculation of the Einstein A for each transition gave a dissociation rate, and the total rate at each wavelength was obtained by summing all transitions covered by the laser linewidth. [10] Although the experimental CaD^+ dissociation is a multiphoton process, we used a first-order model by assuming the dissociation rate is much greater than the first excitation rate. This model produced reasonable agreement with our previous CaH^+ data but cannot be justified theoretically without accurate measurements of the higher excited state potentials.

The spectra labeled "Theory" in **Figure 4.7** use MS-CASPT2 *ab initio* calculations. The potential energy surfaces, transition dipole moments $\mu_{v \to v'}$, and vibronic transition frequencies $G_0 \rightarrow 1(v')$ come from Ref. [81]. Harmonic, ω_1, and anharmonic, $\omega\chi_1$, constants were generated using the internuclear potential curves and R.J. LeRoy's open-source project, Level 8.2. [110] Relative peak heights were determined by assuming a thermal distribution of the rotational states in $1^1\Sigma$. The first 15 *J* rotational levels contribute $>$99.99% of the initial state population and dominate the shapes of the vibronic peaks.

During spectral simulation, the spectral density of the laser was held at a constant

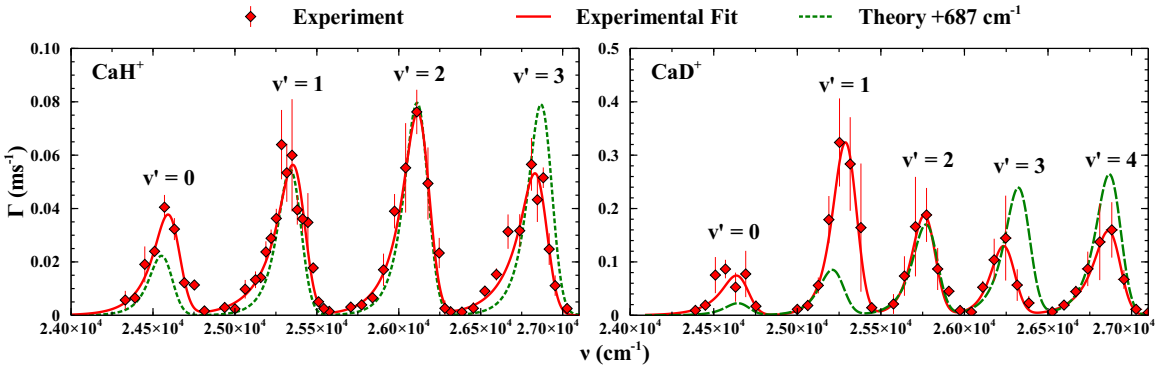

Figure 4.7: Comparisons of the experimental and *ab initio*-predicted spectra for each isotopologue. The optimized parameters include $G_1(v')$, $B_{1,v'}$, and $\mu_{v\to v'}$. Relative heights of theoretical vibronic peaks are governed by MS-CASPT2 transition dipole moments scaled to fit the experimental $v' = 2$ peak, while peak shapes come from the Boltzmann rotational state distribution 298 K.

linewidth of 80 cm^{-1} to match the laser linewidth based on spectrometer measurements. The model's invariant peak intensity of 4.77 $\times$ 10^8 W/m^2 was calculated from the laser power and beam waist diameter at the trap center. The *ab initio* calculated energy of the $1^1\Sigma$ ground vibrational state was used as a reference for all transitions due to lack of experimental data on the ground state potential.

4.3 Results and Discussion

4.3.1 Comparison of Spectra

Figure 4.9 compares the REMPD spectra of CaH^+ and CaD^+. As expected, the CaD^+ transition frequencies were more tightly-packed, owing to the decrease in ω_e accompanying the increase in m_r. The MS-CASPT2 shifted by -50 cm^{-1} agrees with CaH^+. However, it systematically underestimated the CaD^+ vibronic transition frequencies by more than 100 cm^{-1}. If the assignments proposed in Ref. [10] were correct, this study would imply a 150 cm^{-1} isotopic shift of the electronic energy potential

and further evidence the experimentally unobserved transition to the $v' = 0$ state. The isotopic shift of the electronic energy level is large compared to the 10 cm^{-1} shifts seen in KH [106, 108], prompting a reassignment of the vibrational energy levels within the $2^1\Sigma$ manifold.

4.3.2 Vibrational spectroscopic constants

With the new CaH^+ and CaD^+ peak assignments, we determined the spectroscopic constants of the excited state by fitting both theory and experimental values to a second-order model of vibrational energy levels. Vibronic transitions to v' of the $2^1\Sigma$ state were modeled with the equation,

$$v_{v'} = T(1) + \omega_1(v' + \frac{1}{2}) - \omega\chi_1(v' + \frac{1}{2})^2 - E_0, \tag{4.1}$$

where $T(1)$ is the potential minimum of the $2^1\Sigma$ state, and E_0 is the zero-point energy of the ground state. The parameters $T(1)$, ω_1, and $\omega\chi_1$ for both CaH^+ and CaD^+ are varied to fit experimental data points by quadratic regression. Regression curves of theory predictions and experimental fits were plotted **Figure 4.9** to obtain the constants listed in **Table 4.1**. Since CaH^+ ground state information is limited [8], the E_0 energy is confined to the MS-CASPT2 prediction. The experimental constants are determined using the second order fit of Equation 4.1, which compares well with theoretical constants obtained by fitting the vibrational energies determined by LEVEL for MS-CASPT2 with the same equation (labeled in **Table 4.1** as MS-CASPT2 Fit). The theoretical MS-CASPT2 constants and CCSDT constants are derived from fitting the potential curve yield similar values to each other, but lower values of ω_1 compared to using Equation 4.1 due to higher order terms in the fit. The CCSDT calculations are presented in in the next section.

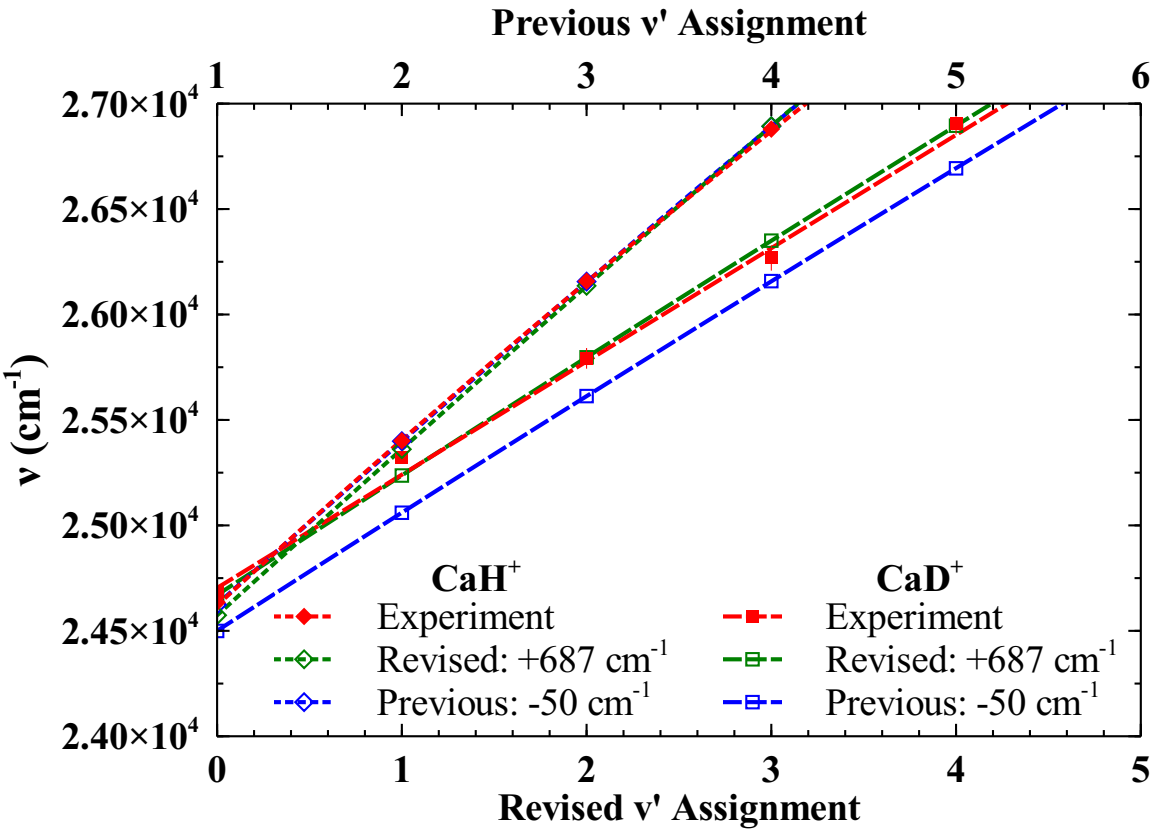

Figure 4.9: The vibronic transitions of CaH^+ and CaD^+ and their associated fits using Eqn. 4.1. Theoretical and experimental values are separated by 687 cm^{-1} on average. Spectroscopic constants of each species may be found in Table 4.1.

Table 4.1: Molecular constants for the $1^1\Sigma \rightarrow 2^1\Sigma$ vibronic transitions of CaH^+ and CaD^+ based on the revised peak assignments are shown. Note that ω_1 and $\omega\chi_1$ scale as $m_r^{-1/2}$ and m_r^{-1}, respectively. All values are in cm^{-1}.

	ω_1	$\omega\chi_1$	T(1) - E_0	E_0
CaH^+ Experimental	813 ± 6	16.8 ± 1.4	24239 ± 5	-
CaH^+ CASPT2 Fit	803 ± 3	7.5 ± 0.7	23487 ± 2	739
CaH^+ CASPT2	773	3.4	23488	739
CaH^+ CCSDT	772	3.8	23907	749
CaD^+ Experimental	521 ± 72	1.0 ± 14.0	24506 ± 76	-
CaD^+ CASPT2 Fit	574 ± 1	3.5 ± 0.1	23697 ± 1	526
CaD^+ CCSDT	553	1.9	24123	537

The spectroscopic constants agree reasonably with theory, however we notice a large shift of the excited state potential relative to the MS-CASPT2 calculation. To maintain the assumption that the internuclear potentials of CaH^+ and CaD^+ are similar, the energy surfaces of the MS-CASPT2 *ab initio*-calculated $1^1\Sigma$ and $2^1\Sigma$ states must be separated by an additional 687 cm^{-1}. The 72 cm^{-1} uncertainty in ω_1 absorbs the CaD^+ $\omega\chi_1$ constant. The deviations in peak position and relative peak heights from our simple model may be due to the details of the dissociation pathway and is a topic of future research. In particular, the shape of the v'=0 peak was not well matched by our simple model leading to a large uncertainty in its calculated position.

4.3.3 Revised Theoretical Predictions

The deviation from the initial *ab initio* calculations could be due to the frozen core electron approximation of the previous MS-CASPT2 study, or non-adiabatic effects. The latter effect is expected to be small based on estimations from other diatomic hydrides. LiH vibrational levels [111, 112] and the KH, KD system [106, 108] feature corrections around 10 cm^{-1}.

To address the former, new computational results for the ground $1^1\Sigma$ state were

obtained and reduce the disagreement to 300 cm^{-1} [11] [1]. All computations were executed through Psi4, [113] with its driver module parsing user input and managing the computation. As part of a project under development, the Quantum Chemistry Common Driver and Databases (QCDB), Psi4 can run its own modules, other interfaced modules (e.g., MRCC [114]), and even other quantum chemistry programs (initially, CFOUR [115]). For this work, (EOM-)CCSD used code intrinsic to Psi4, CCSDT used CFOUR, and EOM-CCSDT and (EOM-)CCSDTQ used MRCC, all from a unified input format. Spectroscopic constants were obtained through Psi4's diatomic anharmonicity module.

These new theoretical results account for many differences seen between the previous predictions and experimental results, **Table 4.2**. Various basis sets (cc-pCV5Z vs cc-pCVTZ) adjust the absolute difference to 70-300 cm^{-1}, compared to the previous 687 cm^{-1} shift.

4.4 Conclusion

The vibronic spectrum of CaD^+ was obtained by scanning a frequency-doubled Ti:Sapph laser over the frequencies predicted to excite $2^1\Sigma$ vibrational modes before coupling to unbound electronic states. Collection of Ca^+ fluorescence allowed us to quantify the rate of CaD^+ dissociation and plot it against frequency at constant laser linewidth and intensity. The harmonic constant $\omega_1 = 521 \pm 72$ cm^{-1} of the $2^1\Sigma$ state were extracted by fitting our experiments to a second-order vibrational energy expression, Eqn. 4.1. The anharmonicity constant was not resolved and may be attributed to an unknown dissociation pathway that is a topic of further research. Comparison of the simulated experiment with MS-CASPT2 predictions revealed a 687 cm^{-1} average deviation from standing theory. CaH^+ vibrational levels within $2^1\Sigma$ were consequently reassigned by reducing the vibrational quantum number by one relative to the previous assignment. [10]

To understand this disagreement, we required further information on the ground and

[1] Computations were performed by C. D. Sherrill and Lori Burns

excited electronic states of CaH^+. New theoretical estimates were found by unfreezing 3s and 3p core electrons through (EOM)-CCSDT/cc-pCV5Z, which accounted for majority of the difference. Experiments using mid-infrared spectroscopy to measure lower vibrational transitions of the ground-state can be combined with previous vibrational overtone data [8] to construct a $1^1\Sigma$ potential energy. Probing higher-lying electronic states could offer insight into photodissociation rates and explain why they differ from theoretical expectations. Future experiments will also include examination of the $2^1\Sigma$ state with rotational resolution, improving the precision of the constants presented here.

Table 4.2: Comparison of MS-CASPT2 [81] and CCSDT/cc-pCV5Z theoretical prediction for vibronic transition frequencies for CaH^+ and CaD^+. Below, experimental transition frequencies are determined by fitting a convolution of laser linewidth and parameter-dependent level structure to laser-induced dissociation rates of CaH^+ and CaD^+. The previous CaH^+ assignments are shifted -50 cm^{-1} from MS-CASPT2 calculations [10] while the revised CaH^+ transitions are shifted +687 cm^{-1}. The resulting fit is compared to an *ab initio* spectrum in **Figure 4.5**.

v'	CaH^+ CASPT2	CaH^+ CCSDT	CaD^+ CASPT2	CaD^+ CCSDT
0	23887	24302.0	23983	24404.4
1	24674	25066.4	24666	24953.3
2	25449	25823.2	25305	25498.4
3	26206	26572.4	25845	26039.7
4	26942	27314.0	26199	26577.2
v'	Previous CaH^+	Revised CaH^+	CaD^+	
0	(missasigned)	24635 ± 49	24683 ± 128	
1	24635 ± 74	25401 ± 21	25321 ± 22	
2	25401 ± 31	26158 ± 18	25792 ± 49	
3	26158 ± 27	26879 ± 29	26268 ± 60	
4	26879 ± 35	-	26908 ± 55	

CHAPTER 5

ROVIBRONIC SPECTRUM OF SYMPATHETICALLY COOLED CaH^+

5.1 Introduction

This chapter was based on the folowing article:

A. T. Calvin, S. Janardan, J. Condoluci, R. Rugango, E. Pretzsch, G. Shu, and K. R. Brown, "Rovibronic spectroscopy of sympathetically cooled $^{40}CaH^+$". J. Phys. Chem. A **122** 12 (2018), pp. 3177-3181.

With the vibronic measurement of CaH^+ reassigned, the next experiment was to obtain a spectrum with rotational resolution. The previously measured transitions were a convolution of the spectrally broad Ti:sapph linewidth and the underlying rotational structure shown in **Figure 5.1**. Femtosecond pulse shaping is widely used to modulate femtosecond optical waveforms [103] and has use in rotationally cooling molecules with nearly diagonal Frank-Condon factors [38]. We employ a modification of that technique here to obtain rotational resolution and extract rotational constants for CaH^+.

5.2 Experimental Methods

A frequency doubled Ti:Sapph laser was chosen for the spectroscopy of CaH^+ because of the large range of frequency tunability and ease of frequency doubling when mode-locked. After frequency doubling, the laser has a pulse width of around 300 fs and a linewidth too broad to resolve rotational transitions. In order to narrow the linewidth, we employed a 4-f pulse shaping system [103]. The pulsed laser is angularly dispersed by a holographic grating (Thorlabs GH25 with 3600 lines/mm). At a focal point away, a cylindrical lens (f=500mm) performs a Fourier transform to convert angular dispersion to spatial dispersion. A 76 μm slit spatial mask lies at the focal point of the lens and is used

to pick out desired frequency components. The slit lies directly in front of a mirror and the second pass recombines the selected frequency components into a collimated beam. The mirror is tilted vertically to spatially separate the outgoing pulse shaped beam from the incoming beam in order to pick the beam with a D-shaped mirror and send to the trap, **Figure 5.2**. 76 μm is the narrowest slit width achieved without spatial diffraction of the outgoing beam. The slit position is correlated to wavelength by the calibration curve shown in **Figure 5.3**. For this, the pulse shaped beam is sent to a commercial spectrometer (Ocean Optics Spectrometer model HR2000+). The center wavelength is estimated for various slit positions. The input power to the 4-f system was 500 mW and the output was typically 50 μW.

The pulse shaped beam is co-aligned to the axial direction of the trap. A shutter (Vincent Associates Model V51452T0 Serial 11355) is used to switch the beam **Figure 5.4**. The beam switching sequence, **Figure 5.5**, exposes the molecular ions to the dissociating beam and Ca^+ fluorescence is measured to obtain the fluorescence recovery scan shown in **Figure 5.6**.

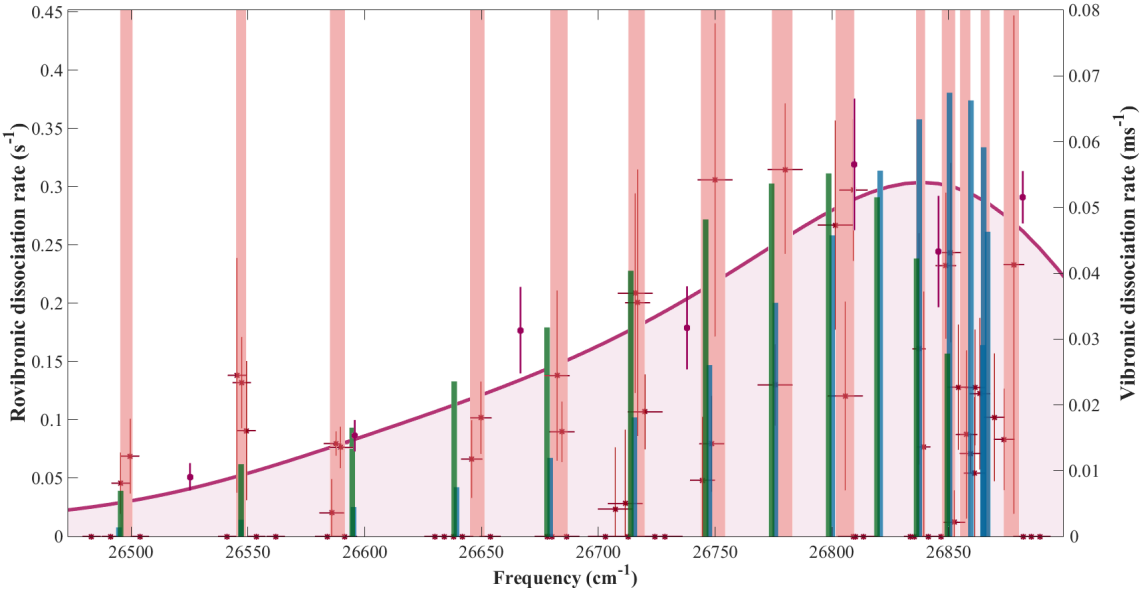

Figure 5.1: The measured vibronic spectrum of the v' = 3 transition in CaH^+ with the measured underlying rotational structure.

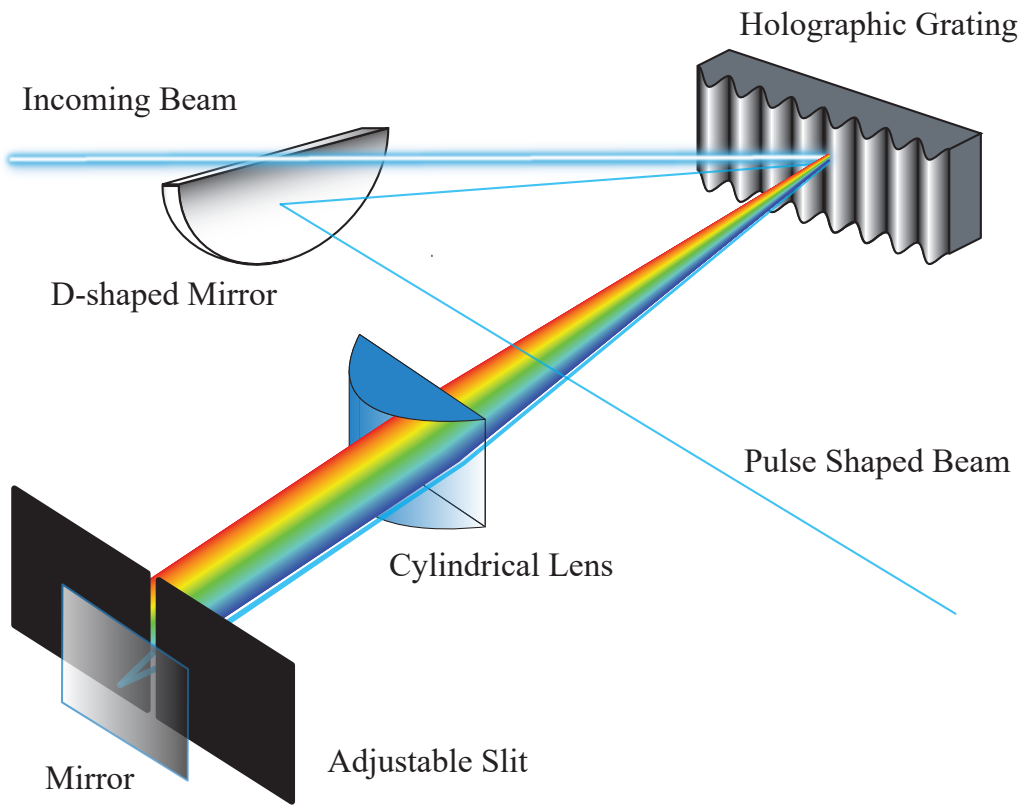

Figure 5.2: To resolve the underlying rovibronic transitions, a 4-f pulse shaping setup is introduced. The position of the slit yields the fine control of the laser wavelength.

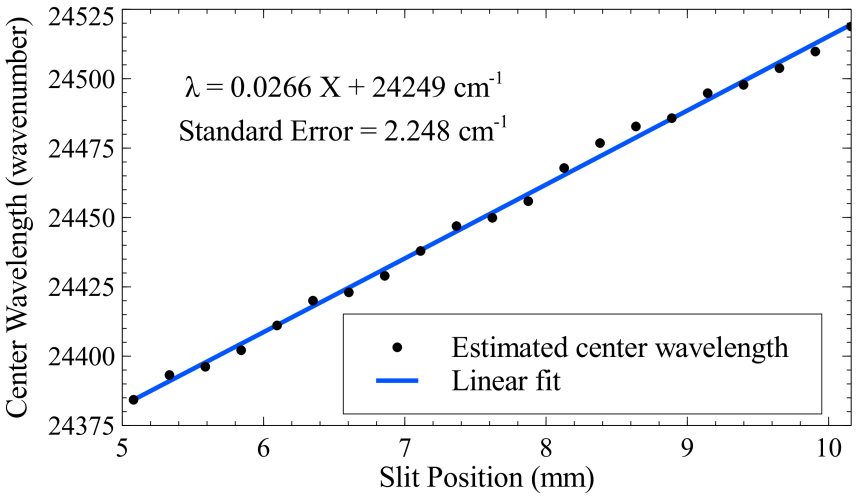

Figure 5.3: The wavelength is determined from the relative slit position by a linear calibration curve. Deviations from a linear trend are due to the limited resolution of the spectrometer and error in estimating the center wavelength, which is taken into account as the uncertainty in wavelength from the standard error of regression. The slit width and resolution of the measured pulse-shaped frequency limit the resolution of the obtained spectrum.

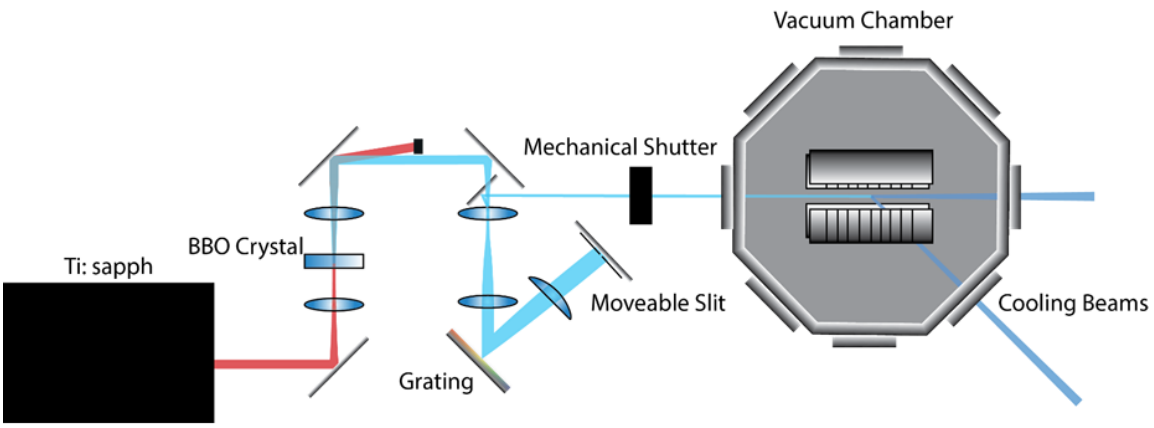

Figure 5.4: The rovibronic experimental schematic shows the pulse shaping added to the Ti:Sapph setup. Here, the long pass and several passes through collimating lenses disperses the fundamental frequency. The frequency doubled beam is sent into the axial direction of the trap.

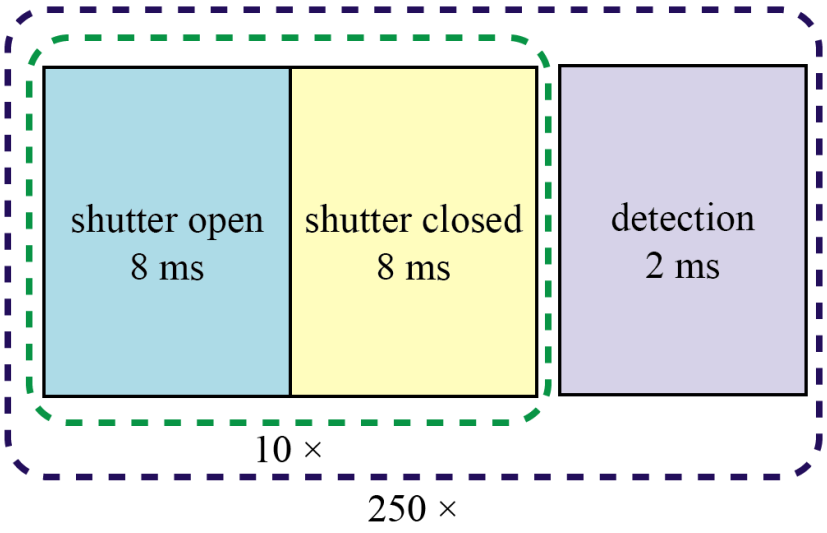

Figure 5.5: The crystal is exposed to the beam alternating between on and off with a time of 8 ms each for 10 cycles. The Ca^+ fluorescence is detected for 200 μs each data point and the process is repeated 250 times.

Figure 5.6 compares the rate of dissociation at different excitation wavelengths. The fluorescence increase is fit to an exponential curve to model a first order dissociation process:

$$A(t) = A_\infty - (A_\infty - A_0)e^{-\Gamma(\lambda)t} \tag{5.1}$$

where $A(t)$ represents the time dependent fluorescence, A_0 is the initial fluorescence, A_∞ is the steady state florescence, and $\Gamma(\lambda)$ is the wavelength dependent rate recorded to produce the spectrum. When the laser is off resonance, the fluorescence increase is negligible and in these cases, the error in $\Gamma(\lambda)$ is larger than 30% and the dissociation value is consistent with 0. The data points for the spectrum **Figure 5.7** are the average of five data points and vertical error bars are the standard deviation. The entire range previously studied with vibronic resolution [10, 11] was remeasured with rotational resolution.

5.3 Results and Discussion

Measuring the dissociation rate as a function of wavelength yielded a series of peaks **Figure 5.7**, corresponding to transitions from $X\ ^1\Sigma, v'' = 0, J'' \rightarrow A\ ^1\Sigma^+, v' = 0 - 4, J'$. The horizontal error bars are the standard error of the residuals from the calibration curve. Up to two or three rovibronic peaks are taken each day with a new calibration curve created every time the Ti:sapph laser central wavelength changed. The measured dissociation rate is not a quantitative indication of the transition strength or relative population in the rotational levels due to uncertainty of laser intensity in the current setup. Rates are extracted from a first order fit of the fluorescence recovery curve, **Equation 5.1**, consistent with previous experiments on this electronic transition [10, 11]. The dissociation pathway is currently unknown and the dissociation is complicated by rethermalization of rotational levels populated in the ground state by blackbody radiation and collisions with the background gas.

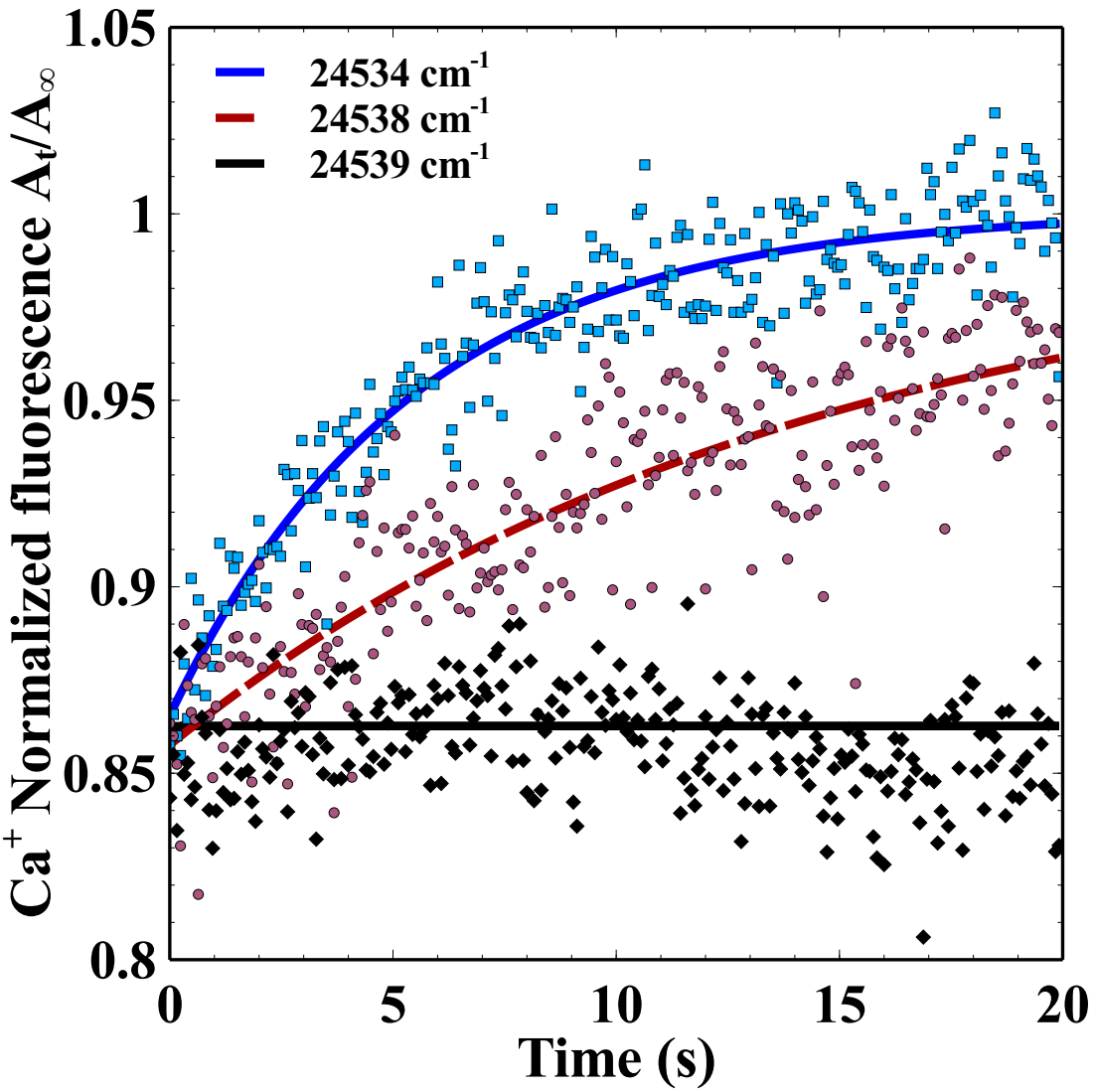

Figure 5.6: Fluorescence recovers when the laser is on resonance with a rovibronic transition of CaH^+ to form Ca^+. A typical dissociation scan for three wavelengths showing the normalized fluorescence over exposure time is used to extract dissociation rates. The 24539 cm^{-1} scan shows no detectable dissociation. The fluorescence recovery curves are fit to a first order dissociation process.

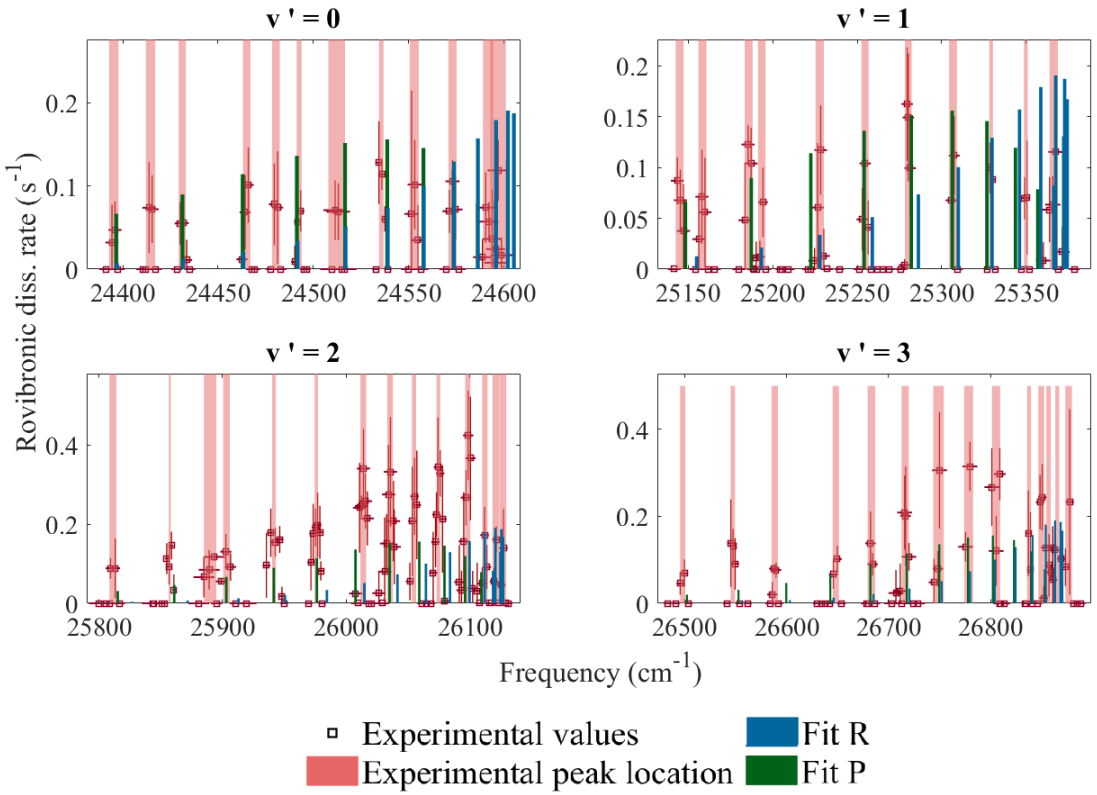

Figure 5.7: The predicted P and R branches using the rotational constant obtained with the Fortrat diagram is compared to the measured experimental transitions. The experimental transitions are centered on the weighted average of the measured dissociation rates with a width obtained from the standard error of the residuals from the calibration curve.

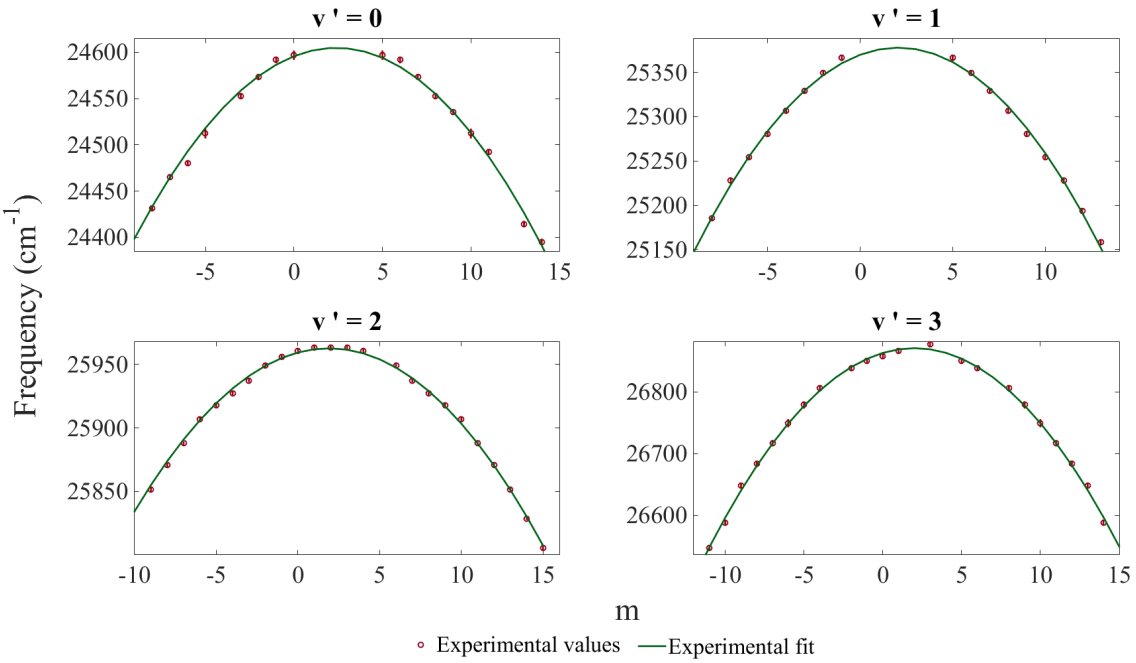

Figure 5.8: Fortrat diagrams composed for each vibronic transition were used to extract $B_{1,v'}$ without higher order distortion terms.

To extract rotational constants from the experimental data, the measured transitions were assigned to an initial rotational state to plot a Fortrat diagram shown in **Figure 5.8**. The experimental transitions were fit to the first order equation to obtain the rotational constants, B':

$$\nu_{P,R} = \nu_{vibronic} + (B' + B'')m + (B' - B'')m^2 \tag{5.2}$$

Here, m is for the rotational quantum number where m=J of the excited state for the R branch and for m=-J of the ground state for the P branch. After an initial guess, measured transitions were re-assigned with m to give a reasonable rotational constant, vibrational offset, and an improved parabolic fit. The parabolic fit parameter of the second order term in **Equation 5.2** at the 95% confidence interval is used to estimate the uncertainty of the rotational constants. We use the value of the rotational constant in the ground state

v'	$\lambda(v')$	B'
0 Theory CCSDT	24294	3.047
0 Experiment	24595 ± 3	3.17 ± 0.08
1 Theory CCSDT	25073	3.00
1 Experiment	25370 ± 1.7	2.86 ± 0.03
2 Theory CCSDT	25861	2.94
2 Experiment	26119 ± 1.8	2.94 ± 0.05
3 Theory CCSDT	26655	2.88
3 Experiment	26863 ± 1.6	2.85 ± 0.03

Table 5.1: Optimized parameters for the experimental spectroscopic constants for the excited states are compared to *ab initio* [11] theoretical parameters for the predicted spectrum. The $\lambda(v')$ term is the $v'' = 0, J'' = 0 \rightarrow v', J' = 0$ transition. Error ranges in the experimental fit constants are the standard errors in the parameters from the Fortrat curve quadratic fit. All values reported are in cm^{-1}.

recently measured by the National Institute of Standards and Technology (NIST), 4.75 cm^{-1} (private communications [1]), and attribute all of the uncertainty to the excited state. If we also fit the ground state B, we measure a ground state B of 4.74 $\pm$ 0.01 cm^{-1} in agreement with the NIST value.

After obtaining a rotational constant from the Fortrat diagrams, the expected P and R branches were plotted in **Figure 5.7**. While this fit is solely a first order approximation, it does provide the reasonable rotational constants for the limited resolution as shown in **Table 5.1**.

Finally, the results were used to extract information about the vibrational constants. Using the quadratic fit of the vibronic transition energies ($\lambda(v')$), the optimized energy difference between the potential minimum of the $X\ ^1\Sigma$ and the $A\ ^1\Sigma^+$ electronic manifolds (T(0,1)), vibrational harmonic constant of the $X\ ^1\Sigma^+$ state (ω_e), and the anharmonic constant ($\omega_e x_e$) were obtained **Table 5.2**. The constants agree better with the *ab initio* calculations than results derived from vibronic spectroscopy and are more reliable since the measured transitions are largely unaffected by the unknown dissociation pathway.

[1] This value was reported with higher precision, a manuscript is in preparation.

The rovibronic results measure vibronic transition frequencies in agreement with vibronic spectroscopy [10] and measure an average shift of 310 ± 3 cm^{-1} in the electronic transition relative to *ab initio* calculations. The rotational constants match well with theory, however higher distortion constants are not measured due to the limited resolution of the experiment. In addition, although v' = 0 was taken with the same method to yield a reasonable rotational constant, two transitions were measured that deviated far from the predicted value by calculating the P and R branches as shown in **Figure 5.7**. It is possible that hot bands (**Figure 5.9**) contribute extra rovibronic transitions from higher lying vibrational states in the ground state accessed by spontaneous decay after the initial excitation. This is more likely to occur for the excitation to the ground vibrational state of the excited electronic state due to the larger Franck-Condon overlap of that state with higher lying vibrational states in the ground electronic state. This effect could explain the relatively large discrepancy between the measured and the theoretical rotational constants for v' = 0, 1 compared to v' = 2, 3, which have predicted larger overlap with the ground vibrational state in the ground electronic state [81] as well as the two transitions in v' = 0 that could not be assigned using the first order model. The spacing and frequency is consistent with transitions from v" = 1, at high J" to v' = 4, J'. Additionally, resolving the transitions with a continuous-wave (CW) laser source would allow more accurate determination of the transition assignments and rotational constants, especially at the bandhead for the v' = 0, 1 cases where the Franck-Condon overlap is weaker.

	CaH^+ Rovibronic	CaH^+ Vibronic	Theory
T(0,1)	24207 ± 2	24239 ± 5	23907
ω_e	786 ± 9.6	813 ± 6	772
$\omega_e x_e$	7.8 ± 2.3	16.8 ± 1.4	3.8

Table 5.2: Spectroscopic constants obtained from the rovibronic spectrum of CaH^+ compared to the constants determined from vibronic spectroscopy and CCSDT [11]. All values reported are in cm^{-1}.

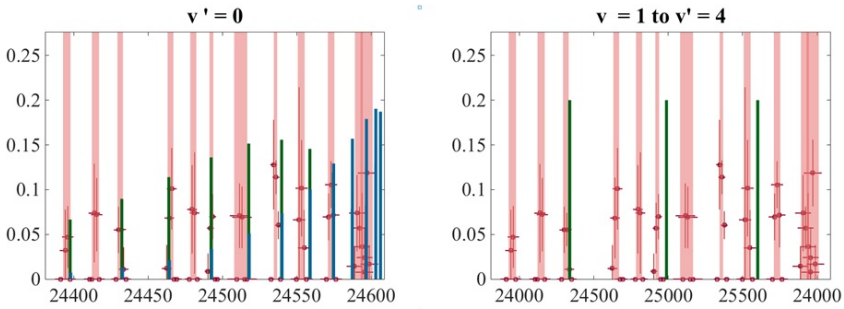

Figure 5.9: The hot bands that may be attributed to the unassigned v' = 0 transitions are shown in the second figure. The hot band spacing is consistent with the spacing of the two unassigned transitions, but the offset is shifted by an amount allowable by the uncertainty in the measured harmonic constants. The predicted P and R branches of v' = 0 extracted by fitting the Fortrat diagram without the unassigned transitions is shown on the right.

5.4 Conclusion and Outlook

The spectrum and rotational constants obtained here represent the highest precision measurements available for an electronic transition in CaH^+. The distortion constants could be easily obtained with a CW frequency-doubled Ti:Sapph given the preliminary spectrum obtained here to facilitate the search. This method provides a convenient means of obtaining rotational resolution over a large range that is extendable to other molecular ions. The fit for the v' = 0 peak suffers relatively larger error due to the lack of resolution of the P and R branches, especially at the bandhead. Nonetheless, the strong v' = 2 transition clearly shows resolved rotational transitions and a hint at a thermal envelope of peak heights. Measurements of this transition with a pulse shaped or CW source could provide a convenient method of state readout for proposed methods of rotational cooling

by a cryogenic chamber [116], sympathetic cooling with a buffer gas of Doppler cooled atoms [44], or by optical pumping[21, 34, 38, 117].

CHAPTER 6

BORON HYDRIDE REACTION SETUP

After the experiments described in this thesis, the molecular chamber was disassembled and a $NaBH_4$ laser ablation target was added to potentially produce BH^+. This molecular ion is attractive in that its nearly diagonal Franck-Condon factors make it a target for direct Doppler cooling [39]. After a few trials of ablation, water from the sodium borohydride crystal increased the base pressure of the chamber substantially. To remedy this problem, a reaction chamber arm was added onto the main trap chamber **Figure 6.1**. This design is inspired by the Odom group's setup for producing AlH^+ [118] with a laser ablation target in front of an H_2 pulsed valve. A jet of H_2 will provide a brief increase in concentration to allow the B* to react, where B* refers to ablated boron in an electronically excited state. The resulting BH plume passes through a conical skimmer (diameter = 1 mm, Beam Dynamics Model 2) which provides a collimated beam and additional differential pumping. A charged deflector plate filters out unwanted charged species created by ablation. Photoionization lasers will photoionize the plume to give BH^+ which is subsequently trapped.

6.1 Experimental setup

The reaction chamber is shown in **Figure 6.1** and represented schematically in **Figure 6.2**. For this, a high concentration transient plume of hydrogen gas is introduced to the reaction chamber through a pulsed valve backed by 1 atm of hydrogen gas. At the same time, the third harmonic of a Nd:YAG (Continuum Minilite II) is used to ablate a boron target. The laser pulses at 355 nm with 6 mW of power and 6 mJ/pulse. Ablation of the target is confirmed by an increase in pressure in the chamber. In principle, the hydrogen plume reacts with ablated boron and carries the reaction products through the skimmer into

the reaction chamber. The 1mm diameter skimmer provides differential pumping and a collimated molecular beam into the trap chamber.

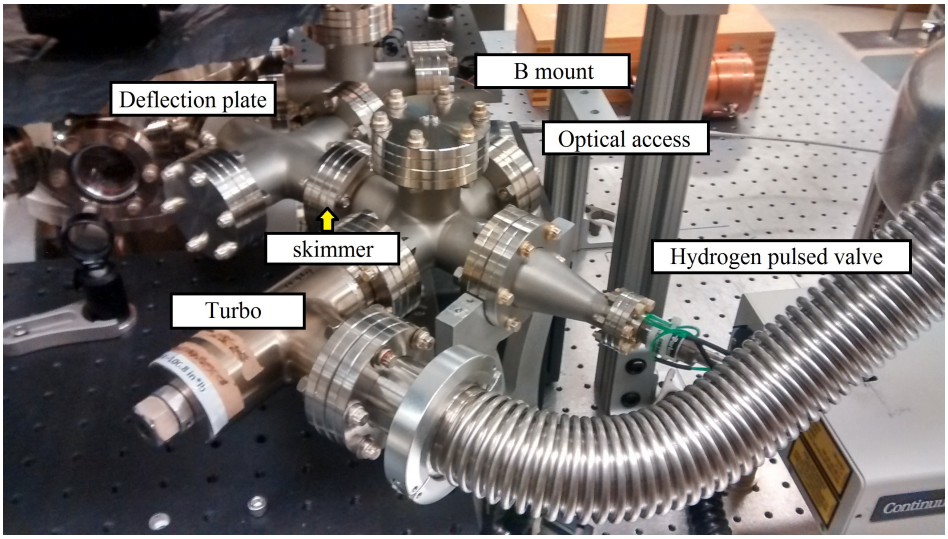

Figure 6.1: The reaction chamber for BH^+ creation.

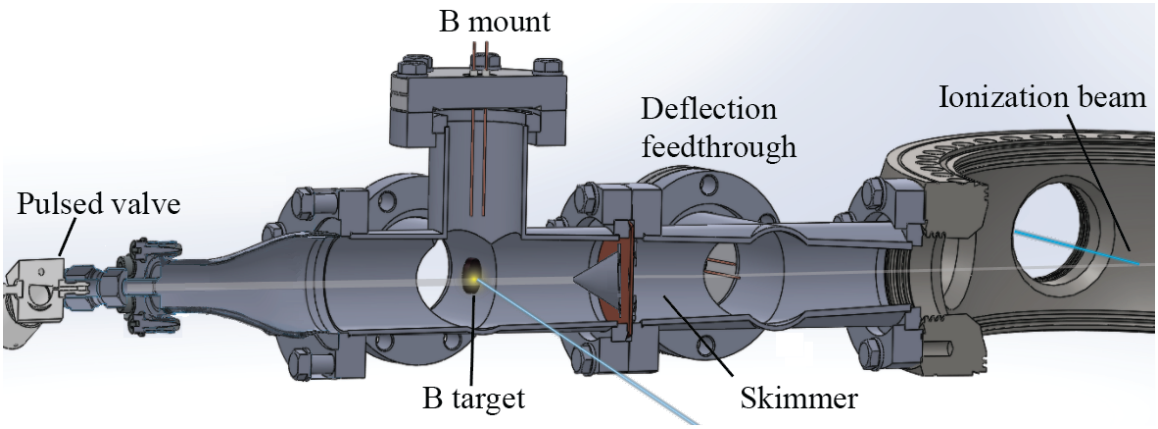

Figure 6.2: A cross section of the BH reaction chamber showing the B target ablated in a stream of hydrogen and photo-ionized in the trap.

The ionization laser is aligned in the radial direction of the trap. This serves two reasons. First, the ionization should occur within the trap since BH molecules ionized outside the trapping region are likely to be deflected by the field. Second, it is easy to co-align the 370 nm laser to the outgoing 423 Ca ionization lasers. The 370 nm molecule ionization presents difficulty for trapping within a Coulomb crystal. The ionization laser induces the 393 nm ($S_{1/2} \rightarrow P_{3/2}$) transition that heats the Coulomb crystal. However, the crystal quickly cools and the effect can be eliminated with a high enough 854 nm repump power.

Two REMPI schemes were proposed as shown in **Figure 6.3**. The (1+2) REMPI scheme involves the 370 nm 3 photon transitions shown to produce BH^+ from diborane-sourced BH [119]. The first corresponds to the excitation of the $X^1\Sigma^+$ v = 0 to $A^1\Pi$ v = 2 transition. The next two photon transition ionizes through the intermediate $B^1\Sigma^+$ state. The (2 + 1') REMPI scheme involves excitation of the $X^1\Sigma^+$ v = 0 to $A^1\Pi$ v = 1 transition with a 433 nm photon. The second 433 nm photon, followed by a 300 nm photon ionize the molecule. The second scheme does not likely produce BH^+ due to the low intensity of the 300 nm source from an incoherent light emitting diode as well as the substantial detuning of the second 433 nm photon from the $B^1\Sigma^+$ state.

For the experiment, the third harmonic of a Q-switched Nd:YAG operating at 10 Hz ablates a boron target in the reaction chamber. The Q-switch sync output is sent to a arbitrary waveform generator (Agilent AG33220 WS) on burst mode gated to the YAG signal. The pulse of 10 μs at 10 Hz is sent to a positive HV pulser (DEI HV 1000) to overdrive the pulse valve. The valve was backed by various pressures up to about 1.5 atm. With the pulse valve driven by 200 V, reactions were observed **Figure 6.4**. The 370 nm light for photoionization was produced by frequency doubling the Ti:sapph laser and the power was kept at 7 mW. To detect any molecular ions trapped, the mass dependant secular motion was excited by applying a variable RF to the center bottom electrode. When the applied frequency approaches the secular frequency of the ion, the crystal is heated and

results in an increase or decrease in the fluorescence depending on the relative detuning of the Doppler cooling lasers. In the regime that the Mathieu a parameter is much less than the q parameter, the secular frequencies scale with the mass to charge ratio [86]. Lighter mass species

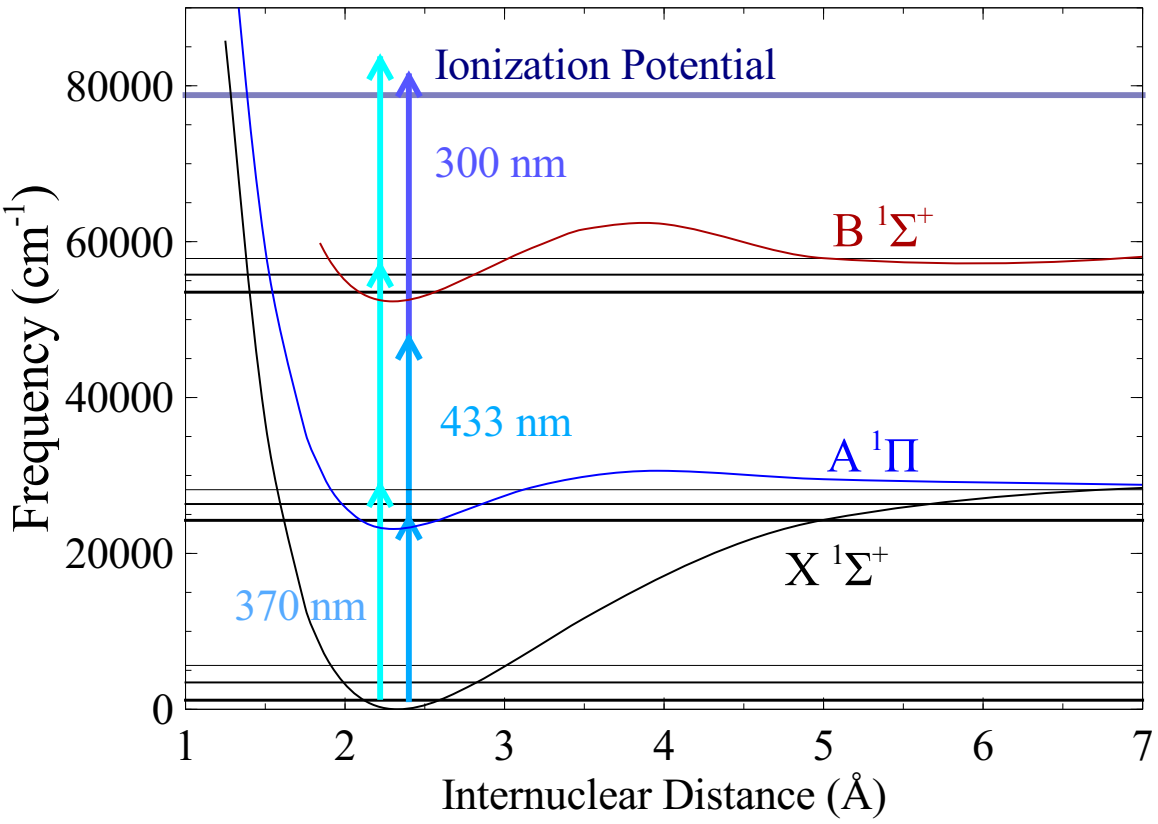

Figure 6.3: Potential energy curves of BH showing two ionization pathways. The first three vibrational levels are shown for each electronic state. The potential curves are produced using RKR potentials presented in Luh, *et al.* [120].

should show up as a change in fluorescence at higher secular frequencies as was observed for sympathetically cooled boron ions [121].

The applied voltage of 259 V at 21.75 MHz gave a q_{Ca^+} of 0.0677. The radial secular frequency of the atomic ion is seen at 0.5 MHz in **Figure 6.5**. The peak at 0.3 MHz and occasionally seen at $\approx$ 0.75 MHz were possibly higher order modes. The expected radial secular frequency for BH^+ was estimated by **Equation 2.28** to be 1.89 and 1.73 MHz for

$^{10}BH^+$ and $^{11}BH^+$ respectively. As shown in **Figure 6.5**, no change in fluorescence in the expected region was measured. Likewise, no darkening of the core of the Coulomb crystal was observed on the EMCCD. The pulse valve was also driven at longer times (ms) with lower voltages, however this flooded the chamber and required several days to regain base pressure.

6.2 Future directions for the boron hydride experiment

Adding a variable phase delay to the pulse valve may be one direction to try in getting reactions from the ablated boron. For this experiment, a crude method of delaying the phase by manually turning on and off the TTL signal to the valve driver while the ablation laser fired independently was tried with no results. Higher backing pressure may be applied but was not pursued due to safety concerns.

One promising method may be to bombard a boron target with protons and mount that directly in the chamber. This would be ideal as ablation of a boron target has demonstrated the production of boron ions that are trappable. For this, an isotopically pure source of boron is ideal to more easily distinguish the BH^+ from the two B^+ isotopes that can be trapped [121]. Finally, BH is typically produced by laser dissociation [119] or electron impact [122] of diborane gas, however the explosive nature of diborane makes this method a last resort.

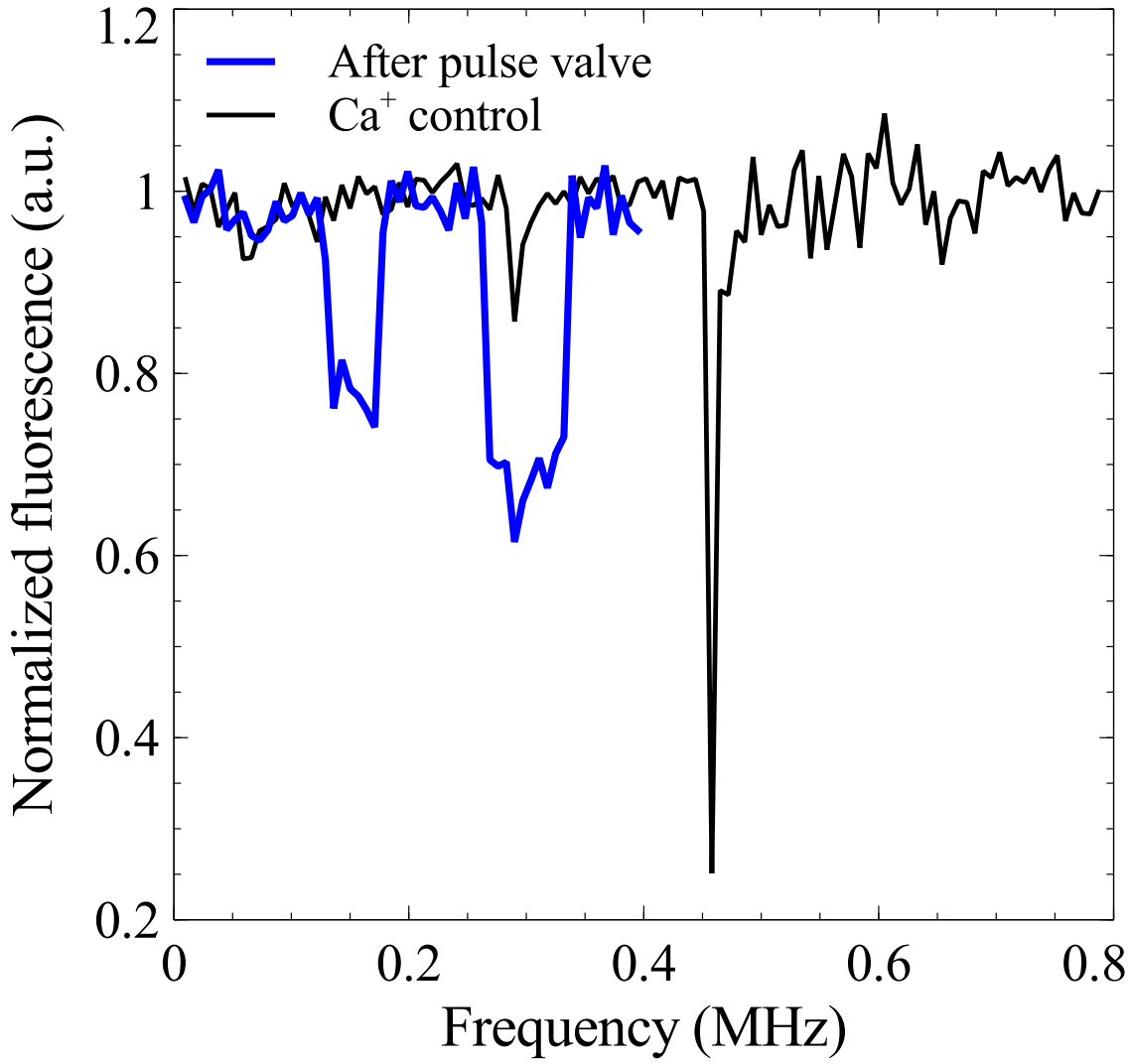

Figure 6.4: Reactions were noticed as a darkening of the outer shell of the crystal. The voltage was 247 V at 21.75 MHz gave a q_{Ca^+} of 0.06. The appearance of secular resonances for masses heavier than Ca^+ indicates reactions. $CaOH^+$ and CaO^+ secular frequencies are expected around 0.276 and 0.218 MHz respectively. This may contribute to the broadening of the peak at 0.3 MHz and the appearance of a higher order secular frequency. In addition, the resolution is lower for higher masses [95]. CaH^+ is expected around 0.38 MHz. Scanning further than 0.4 MHz dumped the crystal and reactions were not observed again, so the appearance of CaH^+ cannot be confirmed. The $CaOH^+$ or CaO^+ could be from water ablated off the boron target and carried by the hydrogen jet.

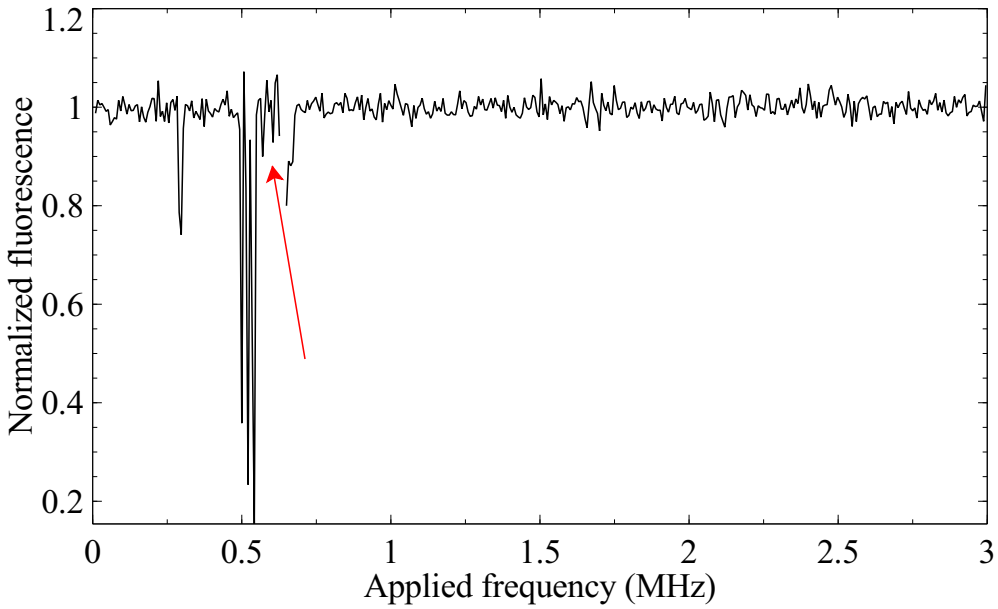

Figure 6.5: No BH^+ was detected by resonant excitation of the secular motion. The MHz signal was applied with a 6 kHz pulse width at an amplitude around 1 V. This amplitude was decreased by half around the Ca^+ resonance. This scan was started from 0.7 MHz to 3 MHz, then scanned from 0.1 to 0.7 MHz. The arrow corresponds to the loss of the crystal due on the Ca^+ resonance.

CHAPTER 7
OUTLOOK AND FUTURE WORK

Much of the interest in the molecular ion community is in state control and in non-destructive measurements of transitions. The spectra obtained here will enable several experiments toward that goal. Rotational cooling by optical pumping [21, 33, 34] is now possible with CaH^+. In addition, our group has demonstrated been able to co-trap laser cooled Ca^+ and a MOT of K. This is a promising step towards using the K MOT to rotationally cool CaH^+ in a Coulomb crystal [44]. Cryogenically cooling the suroundings to suppress blackbody radiation induced transitions is another possibility. In either case, the transitions observed in the rovibronic spectra should provide an indication of the cooling efficiency [123].

These prospects of rotational cooling, along with the ability to sympathetically sideband cool [27], make high precision measurements using non-destructive techniques a promising move forward. A variant of quantum logic spectroscopy [72] on the electronic transition [73] is now possible for CaH^+. Another nondestructive method of photon recoil spectroscopy is also possible, and should be easily implemented with BH^+. The pulse shaping method demonstrated here is extendable to rotationally cool BH^+ by pumping only P branch transitions.

7.1 Spectroscopy on the ground state of CaH^+ and rotational cooling methods in development

Populating a specific rotational state allows enhanced signals during the measurement of a transition, and is crucial high precision measurements. Rotational cooling by optical pumping takes advantage of selection rules and blackbody-induced excitations of rotational levels to drive the molecular ion into the rotational ground state. Driving the

$1^1\Sigma, v = 0, J = 2 \rightarrow 1^1\Sigma v = 1, J' = 1$ transition allows the molecule to relax either to the $1^1\Sigma, v = 0, J = 2$ or $1^1\Sigma, v = 0, J' = 0$ states as shown in **Figure 7.1**. However, continuous excitations should pump the molecule to the absolute ground state after several cycles. In order to resolve transitions for this pumping cycle, the fundamental transition in CaH^+ must be studied with rotational resolution with a 6.9 μm quantum cascade laser (QCL). A variation on photodissociation provides a convenient means to accomplish this with the rovibronic transitions measured [123]. For this, the pulse-shaped, frequency doubled Ti:Sapph laser is parked on a measured rovibronic transition. When the probe QCL is resonant with a $1^1\Sigma, v = 0, J$ to $1^1\Sigma, v = 0, J' = J \pm 1$, the population in that particular rotational state is depleted and measured as a suppression in the photo-dissociation signal.

7.2 Towards non-destructive measurements of CaH^+

The spectroscopic information obtained in this work paves the way for future non-destructive measurements on CaH^+. The destructive photodissociation method conveniently provides spectroscopic information. However, it has the disadvantage of being inefficiently slow for single ion measurements and adds systematic errors caused by slight changes in the experimental conditions by reloading [124]. Nondestructive measurements using quantum logic [72] takes advantage of the fact that the atomic ion's internal state is easily determined from the fluorescence counts **Figure 7.2**. A molecular ion can be co-trapped and entangled to the atomic ion through the Coulomb interaction to map the state of the molecular ion to the atomic ion. In the context of high precision measurements of weak clock transitions, a one-photon transition of any wavelength can be measured as scattering of many optical photons of the atomic ion.

The natural linewidth of a transition is limited by the time-energy uncertainty relation, $\Delta E \Delta t = \hbar/2$. $\tau = \Delta t$ is defined as the lifetime of the transition. It is inversely

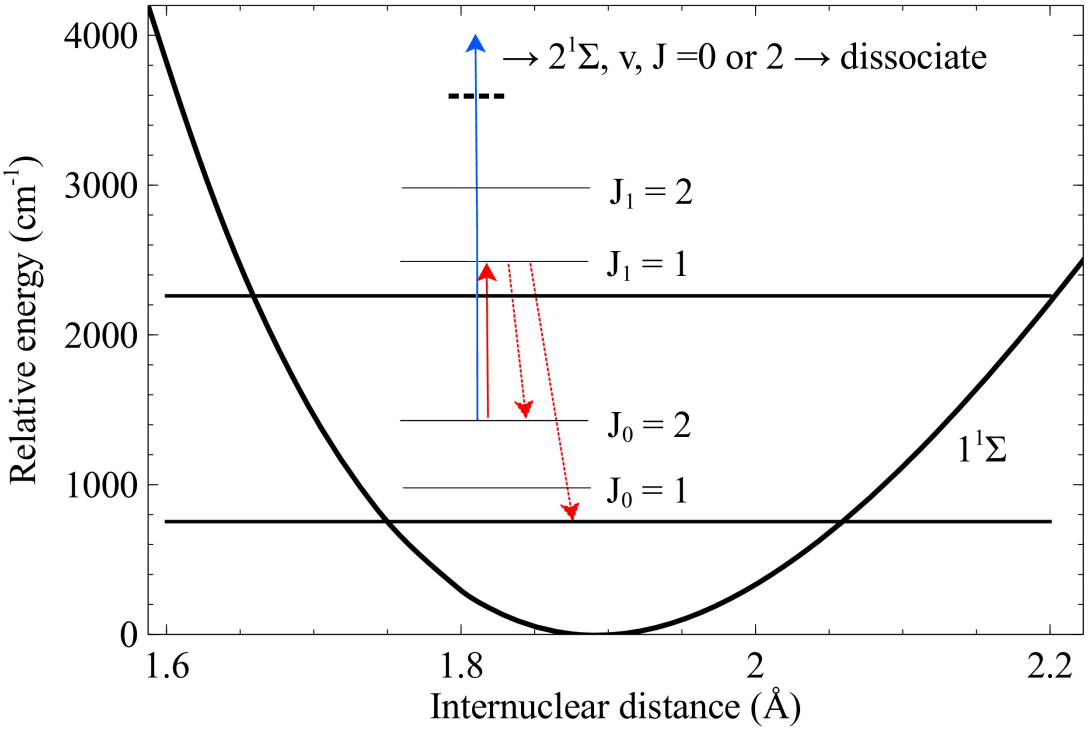

Figure 7.1: Potential energy diagram of the ground state of CaH^+ showing an optical pumping scheme proposed in [33]. Rotational energy levels are not to scale for visual clarity. Subscripts on the J refer to the vibrational quantum number. The molecule is driven to the ground state by a 6.9 μm laser (red) and the cooling is detected by a visible laser parked on one of the measured rovibronic transions (blue).

proportional to the Einstein A coefficient [125],

$$A_{fi} \approx \frac{16\pi|\mu_{if}|^2\nu^3}{3\epsilon_0 hc^3} \tag{7.1}$$

The spontaneous emission rate depends on the transition dipole moment (μ_{if}) squared and the frequency (ν) cubed. The rate can be suppressed by choosing a state with a weak transition or transition with a large transition wavelength. Hence, a forbidden rovibrational transition [22] is a target for high precision measurements. These weaker transitions are also more difficult to measure, especially for a single molecular ion. With direct fluorescence measurements impractical, mapping the transition to a strongly fluorescing atomic ion is more desirable. While a destructive measurement may be used, a non-destructive measurement is preferred to allow rapid collection for high signal-to-noise and to avoid systematic errors in reloading.

The basic scheme for non-destructive, high precision measurement follows quantum logic spectroscopy used first on a clock transition in Al^+ [72]. Here, a bright "logic" ion, named for its ability to be laser cooled and optically detected, is co-trapped with a dark "spectroscopy" ion that cannot be directly probed. The spectroscopy ion could be an atomic ion with a weak clock transition of interest, or a molecular ion. In either case, the pair is state initialized, usually into the ground state for every degree of freedom. Sideband cooling has been demonstrated for CaH^+ [9, 27] and MgH^+ [28] and discussed in detail elsewhere [95, 126, 127]. This involves exciting the atomic ion on the red sideband, typically to a long-lived state. The state can then be deshelved to a higher lying state that spontaneously decays to the ground electronic state. The emission preserves the motional state. The process is repeated until the motion approaches the ground state.

Since the motional modes are shared by the species trapped, the molecular motion is cooled as well. A spectroscopy laser probes an internal transition of the spectroscopy ion and excites the motion of the ion pair conditional on the excitation on the spectroscopy ion. The motional state is read out on the logic ion by the measurement of a photon. Hence, any

transition, with any strength or frequency, is mapped to a strong optical transition through the shared motional mode.

In the specific case where Ca^+ acts as the logic ion as shown in **Figure 7.3**, a 729 ($S_{1/2} \rightarrow D_{5/2}$) laser is used to determine the motional state. This transition is suitably narrow enough to resolve the motional sidebands (usually on the order of hundreds of kHz). If the ion pair's motion is heated, a red sideband pulse excites the Ca^+ to the metastable $D_{5/2}$ state. With an 854 nm pulse, the ion is excited to the $P_{3/2}$ state, which quickly decays to $S_{1/2}$ and emits a 393 nm photon that can be easily measured by the PMT. If the ion pair remains cooled, no excitation to the metastable state occurs and the fluorescence is dark to the photon counter.

The preceding scheme is useful for narrow transitions for which the blue sideband of the spectroscopy ion's transition can be resolved and coherently excite the motion of the ion pair as shown in 7.3. These are in general the narrow linewidth transitions of interest for precision measurements. However, implementing such a scheme efficiently and with suitable signal to noise [95] requires state preparation and presents a challenge in the case of molecular ions since their internal state is at thermal equilibrium with the environment. In the case of diatomic alkaline earth metal hydrides, the vibrational spacing is wide enough that only the ground state is significantly populated. The rotational levels are excited as shown by the measurements in the preceding chapter. For the broader (3 MHz natural linewidth) rovibronic transitions measured, another approach is possible to engineer an interaction Hamiltonian that excites the ions' motion conditional on the internal state of the molecular ion. Non-destructive state detection implemented has been demonstated on MgH^+[73] and is extendable to CaH^+. The lack of spectra for CaH^+ relative to MgH^+ [123, 128] has so far hindered the implementation of the quantum logic technique on the electronic transition. to implement this technique, a Ca^+ - CaH^+ pair are sideband cooled to the lowest translational motional state[27]. A pair of detuned counterpropagating lasers

create a standing walking wave that induces a Stark shift [73, 95, 126],

$$\delta E = \frac{\mu_{ge} E^2 \omega_{ge}}{2(\omega_{ge}^2 - \nu^2)}, \tag{7.2}$$

where E is the magnitude of the electric field, μ_{ge} is the transition dipole moment, ω_{ge} is the transition frequency, and ν is the laser frequency. If the spectroscopy laser is sent in the form of two counter-propagating beams with $\Delta\nu = \nu_1 - \nu_2$, and wavevectors k_1 and k_2 the electric field has the form:

$$E_t = Ecos(\frac{1}{2}(\nu_1 + \nu_2)t)cos(\frac{\Delta k}{2}z - \frac{\Delta\nu t}{2}). \tag{7.3}$$

The gradient of the Stark shift gives an induced force,

$$F = -\Delta(\delta E) = -\Delta(\frac{\mu_{ge}^2 E^2 \omega_{ge}}{\omega_{ge}^2 - \nu^2} cos^2(\frac{\Delta k}{2}z - \frac{\Delta\nu t}{2}) \tag{7.4}$$

This force is dependent on the detuning from the molecule's resonance, and coherently excites the ion's motion when $\Delta\nu$ is on resonance with the motional frequency. This excitation can be detected by measuring the temperature (ratio of the red and blue resolved sidebands) as a function of time for each detuning. Since the Rabi frequency of a transition of an ion with the Lamb-Dicke parameter, η, has a dependence on the temperature (t) [126],

$$\rho_D(t) = \frac{1}{2}[1 - \frac{1}{\bar{n}+1}\frac{\cos(2\Omega_0 t)(1 - x\cos(2\Omega_0 t\eta^2)) + x\sin(2\Omega_0 t)\sin(2\Omega_0 t\eta^2)]}{1 + x^2 - 2x\cos(2\Omega_0 t\eta^2)}. \tag{7.5}$$

This effectively measures the Rabi frequency as a function of the optical dipole force to obtain the spectrum.

One disadvantage of this approach is that it only observes a signal of the transition when the molecular ion is in the rotational state of interest. The signal is observed consistent with

blackbody radiation induced quantum jumps [73]. Modifications of the current atomic trap setup used in the previous sideband cooling experiment are required for the non-destructive state detection. A metal sheath surrounding the wires inputting the RF signal to the trap contribute to the high capacitance that impede obtaining a large enough secular frequency for sideband cooling. The v'= 3 transition would be advantageous for this experiment since it is far enough away from the Ca^+ cooling transition that heating is minimized.

For this experiment, a CW laser is preferable for stability and improved resolution over the pulsed shaped Ti:sapph. An external cavity diode laser that covers the v = 0 to v'= 3 transition is already used for photoionizing Ca. This could easily be controlled to perform resonance enhanced photodissociation spectroscopy of this transition to resolve the P and R branches and as a proof of concept that the CW laser can access a transition of interest. The preliminary spectrum could be obtained in the molecular chamber used for the previous vibronic and rovibronic experiments. Afterward, work with a single molecular ion could be performed towards nondestructive measurements.

Another form of nondestructive detection relies on the incoherent heating of the motion from the photon recoil [28]. Such a scheme has been proposed for efficient detection of transitions in polyatomics [75]. After motional cooling, the probability of exciting the motion after absorbing the N_a photons is approximated by

$$p_e \approx 1 - e^{-N_a^2 \eta^2.} \tag{7.6}$$

For a typical Lamb-Dicke parameter, η of 0.1, detection with significant signal to noise requires the scattering 10 photons. Demonstrating this technique would ideal on a molecule that scatters many photons. A molecule with diagonal Franck-Condon factors like BH^+ would be ideal since the molecule decays to the initial state after excitation with high probability. This molecule could scatter up to 600,000 photons per second with appropriate repump lasers. In addition, the demonstration of pulse shaping here will be easily extended to rotational cooling of BH^+ on the 379 $X^2\Sigma, v = 0 \rightarrow A^2\Pi, v = 0$

cooling transition towards full quantum control of a molecular ion **Figure 7.4**.

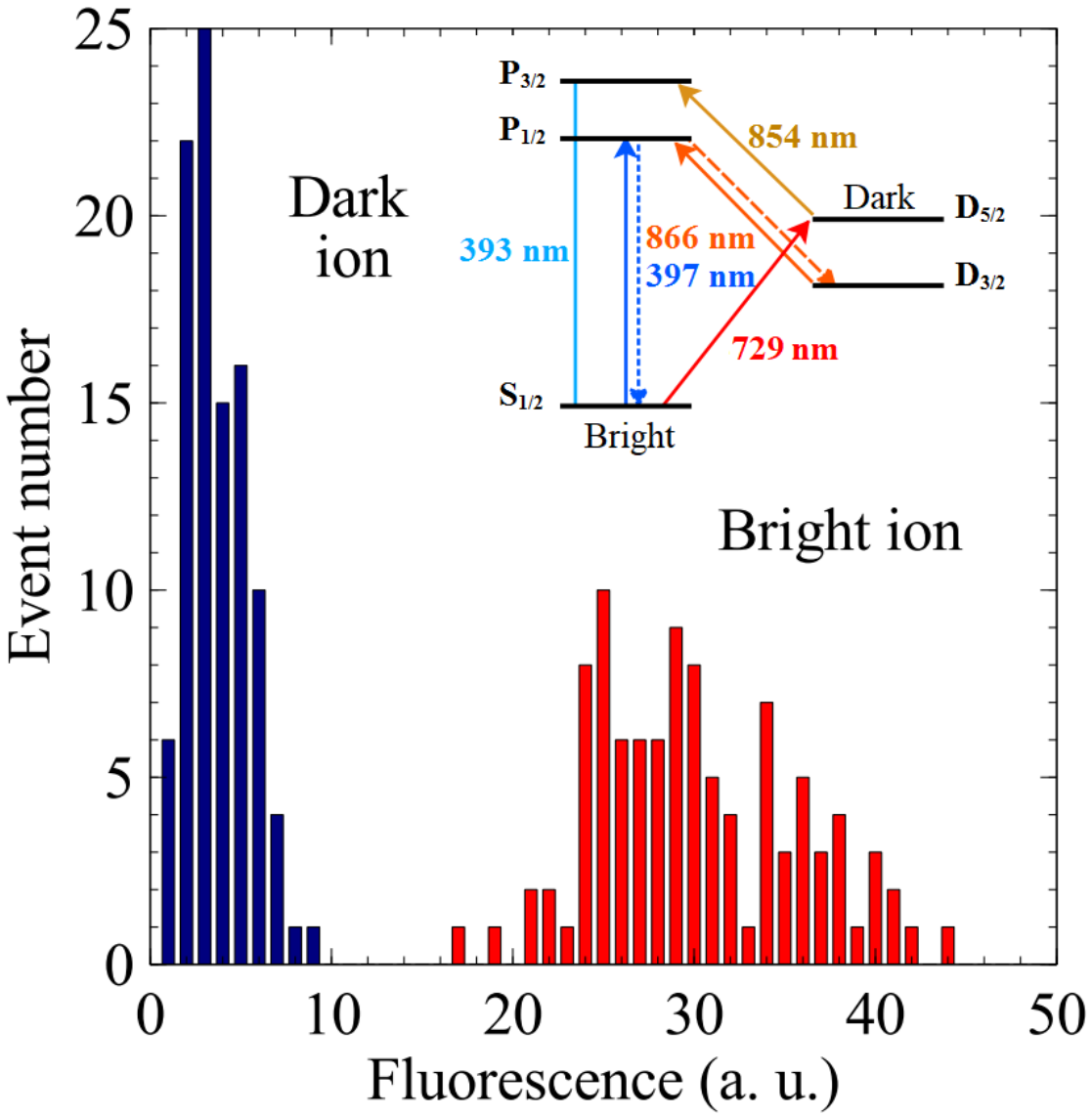

Figure 7.2: Energy level diagram of Ca^+ for state detection is shown alongside a histogram demonstrating the fluorescence measurement used to determine the internal state of the calcium ion with high fidelity. For calibration, a histogram of counts is collected when the ion is bright, and when the ion is shelved to the $D_{5/2}$ state. From this, a threshold is established so that if more than the threshold of counts is observed, the ion is determined to be in the bright state.

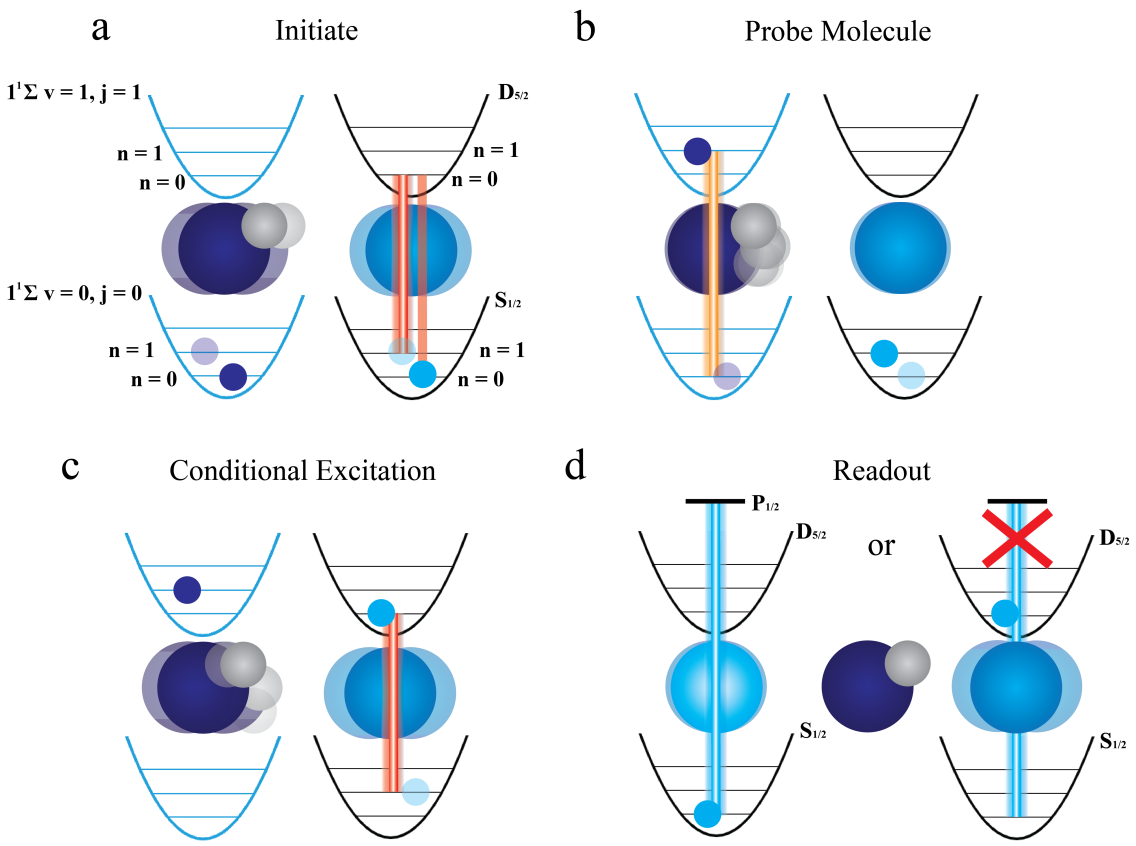

Figure 7.3: a. Initiate: With the molecule in the desired rovibrational state, a narrow laser drives an electronic transition on the resolved red sideband. The ion can be deshelved from the excited electronic state to essentially decay to the ground electronic state while preserving the number of phonons. The net effect, shown here, is the removal of a phonon for each excitation cycle. The process is repeated until the ion is cooled to the ground state of motion. The molecule's motion is cooled as well because of coupling through the Coulomb interaction. b. Probe the molecule: An excitation of the blue sideband of the molecular ion increases the motion if the probe laser is on resonance with the transition. c. Conditional excitation of the atomic ion: The red sideband of the atomic ion drives to the excited state conditional on the excitation of the motion. d. Readout: Fluorescence from the cooling transition is measured from the atomic ion if the motion was not excited or unobserved if the motion was. This scheme is one which non-destructively transfers information from the molecular ion to the atomic ion and maps a single photon transition of any wavelength to a visible transition that scatters millions of photons.

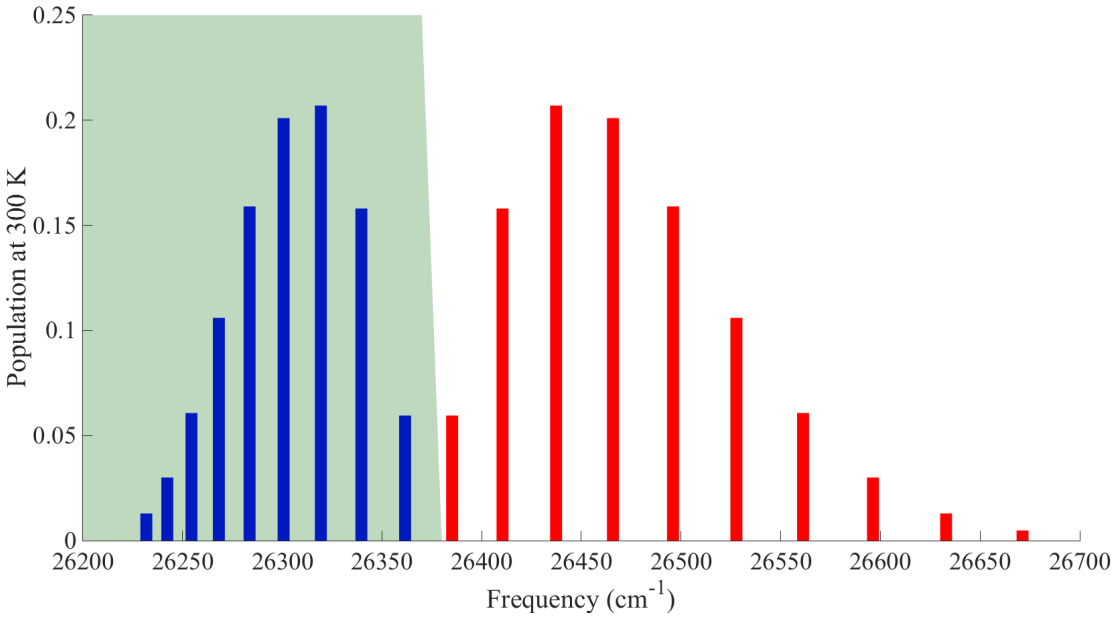

Figure 7.4: A 10 cm^{-1} pulse shaping resolution is enough to rotationally cool BH^+ by driving only the P branch transitions. Vibrational branching is not considered here, but can be taken advantage of to cool parity levels [38] .

Appendices

APPENDIX A

ROVIBRONIC TRANSITIONS OF CaH^+

Table A.1: The experimental rovibronic frequency along with the associated assignment for each transition. Repeated values are due to unresolved P and R branches. The rotational quantum number where m=J of the excited state for the R branch and for m=-J of the ground state for the P branch is labeled here by m. All transition frequencies are reported in cm^{-1}.

v' = 0		v' = 1		v' = 2		v' = 3	
m	Frequency	m	Frequency	m	Frequency	m	Frequency
-8	24431.2 ± 1.9	-8	25185.7 ± 2.4	-9	25903.2 ± 2.7	-11	26547.1 ± 2.1
-7	24465.0 ± 2.0	-7	25227.7 ± 2.4	-8	25941.6 ± 1.5	-10	26588.3 ± 3.2
-6	24480.4 ± 2.0	-6	25254.6 ± 2.1	-7	25975.9 ± 1.3	-9	26648.2 ± 3.1
-5	24512.3 ± 4.4	-5	25280.2 ± 2.0	-6	26013.9 ± 2.4	-8	26683.2 ± 3.7
-3	24553.0 ± 2.3	-4	25306.7 ± 2.4	-5	26035.5 ± 2.3	-7	26716.4 ± 3.5
-2	24573.1 ± 2.2	-3	25329.2 ± 1.1	-4	26054.9 ± 1.7	-6	26749.1 ± 5.2
-1	24591.8 ± 2.7	-2	25349.8 ± 1.1	-3	26074.7 ± 1.5	-5	26778.7 ± 4.4
0	24597.0 ± 4.1	-1	25366.3 ± 2.5	-2	26098.4 ± 2.1	-4	26805.6 ± 4.0
5	24597.0 ± 4.1	5	25366.3 ± 2.5	-1	26112.2 ± 2.2	-2	26838.0 ± 1.9
6	24591.8 ± 2.7	6	25349.8 ± 1.1	0	26121.0 ± 2.7	-1	26849.9 ± 2.9
7	24573.1 ± 2.2	7	25329.2 ± 1.1	1	26126.8 ± 2.7	0	26857.1 ± 2.2
8	24553.0 ± 2.3	8	25306.7 ± 2.4	2	26126.8 ± 2.7	1	26865.6 ± 1.9
9	24535.7 ± 1.2	9	25280.2 ± 2.0	3	26126.8 ± 2.7	3	26876.8 ± 3.3
10	24512.3 ± 4.4	10	25254.6 ± 2.1	4	26121.0 ± 2.7	5	26849.9 ± 2.9
11	24492.6 ± 1.3	11	25227.7 ± 2.4	6	26098.4 ± 2.1	6	26838.0 ± 1.9
13	24414.6 ± 2.4	12	25193.4 ± 2.2	7	26074.7 ± 1.5	8	26805.6 ± 4.0
14	24395.3 ± 2.5	13	25158.3 ± 2.3	8	26054.9 ± 1.7	9	26778.7 ± 4.4
				9	26035.5 ± 2.3	10	26749.1 ± 5.2
				10	26013.9 ± 2.4	11	26716.4 ± 3.5
				11	25975.9 ± 1.3	12	26683.2 ± 3.7
				12	25941.6 ± 1.5	13	26648.2 ± 3.1
				13	25903.2 ± 2.7	14	26588.3 ± 3.2
				14	25857.3 ± 0.8		
				15	25811.3 ± 2.8		

APPENDIX B

DC CONNECTIONS MAP

Table B.1: The map of connections of the DC electrodes for the molecular chamber.

Electrode Number	DAC Channel	DB 25 Channel
Top 11	16	9
Top 10	19	23
Top 9	14	8
Top 8	20	11
Top 7	15	21
Top 6	17	22
Top 5	18	10
Top 4	21	24
Top 3	22	12
Top 2	23	25
Top 1	24	13
Bottom 11	3	15
Bottom 10	4	3
Bottom 9	5	16
Bottom 8	2	
Bottom 7	6	4
Bottom 6	7	17
Bottom 5	8	5
Bottom 4	9	18
Bottom 3	10	6
Bottom 2	1	
Bottom 1	11	19

REFERENCES

[1] Uta Wille. “Reaction mechanisms: radical and radical ion reactions”. In: *Annu. Rep. Prog. Chem., Sect. B: Org. Chem.* 108 (2012), pp. 228–250.

[2] Z.V. Todres. “Ion-radical organic reactions”. In: *Tetrahedron* 41.14 (1985), pp. 2771 –2823.

[3] T. J. Millar. “Astrochemistry”. In: *Plasma Sources Science and Technology* 24.4 (2015), p. 043001.

[4] M. Larsson, W. D. Geppert, and G. Nyman. “Ion chemistry in space”. In: *Reports on Progress in Physics* 75.6 (2012), p. 066901.

[5] Charles M. Olmstedt. “Sunspot bands which appear in the spectrum of a calcium arc burning in the presence of hydrogen”. In: *Astrophys. J.* 27 (1908), pp. 66–69.

[6] R. Georgiadis and P. B. Armentrout. “Kinetic energy dependence of the reactions of calcium(1+) and zinc(1+) with hydrogen, deuterium, and hydrogen-d1: effect of empty versus full d orbitals”. In: *J. Phys. Chem.* 92.25 (1988), pp. 7060–7067.

[7] A. K. Hansen et al. “Single ion recycling reactions”. In: *Angew. Chem. Int. Ed.* 51.32 (2012), pp. 7960 –7962.

[8] Ncamiso B Khanyile, Gang Shu, and Kenneth R Brown. “Observation of vibrational overtones by single molecule resonant photodissociation”. In: *Nat. Comm.* 6.7825 (2015).

[9] C. Chou et al. “Preparation and coherent manipulation of pure quantum states of a single molecular ion”. In: *Nature* 545 (2017), pp. 203–207.

[10] Renè Rugango et al. “Vibronic spectroscopy of sympathetically cooled CaH^+”. In: *ChemPhysChem* 17.22 (2016), pp. 3764–3768.

[11] J. Condoluci et al. “Reassigning the CaH^+ $1^1\Sigma \rightarrow 2^1\Sigma$ vibronic transition with CaD^+”. In: *Journal of Chemical Physics* 147.21 (2017), p. 214309.

[12] Aaron Calvin et al. “Rovibronic spectroscopy of sympathetically cooled $^{40}CaH^+$”. In: *J. Phys. Chem. A* 122.12 (2018), pp. 3177–3181.

[13] J. H. Marks, T. B. Ward, and M. A. Duncan. “Photodissociation of manganese oxide cluster cations”. In: *J. Phys. Chem. A* 122.13 (2018), pp. 3383 –3390.

[14] E. K. Campbell et al. “Laboratory confirmation of C_{60}^+ as the carrier of two diffuse interstellar bands”. In: *Nature* 523.7560 (2015), pp. 322–323.

[15] P. C. Schmid et al. “An ion trap time-of-flight mass spectrometer with high mass resolution for cold trapped ion experiments”. In: *Rev. Sci. Instrum.* 88 (2017), p. 123107.

[16] Stephan Schlemmer and Oskar Asvany. “Laser induced reactions in a 22-pole ion trap”. In: *Journal of Physics: Conference Series* 4 (2005), p. 134.

[17] P. Blythe et al. “Production of ultracold trapped molecular hydrogen ions”. In: *Phys. Rev. Lett.* 95 (18 2005), p. 183002.

[18] A. Ostendorf et al. “Sympathetic cooling of complex molecular ions to millikelvin temperatures”. In: *Phys. Rev. Lett.* 97 (24 2006), p. 243005.

[19] D. Offenberg et al. “Translational cooling and storage of protonated proteins in an ion trap at subkelvin temperatures”. In: *Phys. Rev. A* 78 (6 2008), p. 061401.

[20] K. Højbjerre et al. “Consecutive photodissociation of a single complex molecular ion”. In: *Phys. Rev. A* 77 (3 2008), p. 030702.

[21] U. Bressel et al. “Manipulation of individual hyperfine states in cold trapped molecular ions and application to HD^+ frequency metrology”. In: *Phys. Rev. Lett.* 108.18 (18 2012), p. 183003.

[22] Matthias Germann, Xin Tong, and Stefan Willitsch. “Observation of electric-dipole-forbidden infrared transitions in cold molecular ions”. In: *Nat. Phys.* 10 (2014), pp. 820 –824.

[23] Xin Tong, Alexander H. Winney, and Stefan Willitsch. “Sympathetic Cooling of Molecular Ions in Selected Rotational and Vibrational States Produced by Threshold Photoionization”. In: *Phys. Rev. Lett.* 10 (2010), pp. 820 –824.

[24] K.-K. Ni et al. “A High Phase-Space-Density Gas of Polar Molecules”. In: *Science* 322 (5899 2008), pp. 231 –235.

[25] Sebastian A. Will et al. “Coherent Microwave Control of Ultracold $^{23}Na^{40}K$ Molecules”. In: *Phys. Rev. Lett.* 116 (22 2016), p. 225306.

[26] Mingyang Guo et al. “High-resolution internal state control of ultracold $^{23}Na^{87}Rb$ molecules”. In: *Phys. Rev. A* 97 (2 2018), p. 020501.

[27] R. Rugango et al. “Sympathetic cooling of molecular ion motion to the ground state”. In: *New J. Phys.* 17.3 (2015), p. 035009.

[28] Y. Wan et al. “Efficient sympathetic motional ground-state cooling of a molecular ion”. In: *Phys. Rev. A* 91 (2015), p. 043425.

[29] A. Hashemloo and C. M. Dion. “Rotational dynamics of a diatomic molecular ion in a Paul trap”. In: *J. Chem. Phys.* 143.20 (2015), p. 204308.

[30] Anders Bertelsen, Solvejg Jørgensen, and Michael Drewsen. “The rotational temperature of polar molecular ions in Coulomb crystals”. In: *J. Phys. B* 39.5 (2006), pp. L83–L89.

[31] J. C J Koelemeij, B. Roth, and S. Schiller. “Blackbody thermometry with cold molecular ions and application to ion-based frequency standards”. In: *Phys. Rev. A.* 76.2 (2007), p. 023413.

[32] A. Windberger et al. “Coulomb crystals in a cryogenic Paul trap for sympathetic cooling of molecular ions and highly charged ions”. In: *AIP Conference Proceedings* 1521.1 (2013), pp. 250–256.

[33] I. S. Vogelius, L. B. Madsen, and M. Drewsen. “Rotational cooling of heteronuclear molecular ions with $^1\Sigma$, $^2\Sigma$, $^3\Sigma$, and $^2\Pi$ electronic ground states”. In: *Phys. Rev. A* 70 (5 2004), p. 053412.

[34] Peter F. Staanum et al. “Rotational laser cooling of vibrationally and translationally cold molecular ions”. In: *Nat. Phys.* 6 (2010), pp. 271–274.

[35] Eric R. Hudson. “Method for producing ultracold molecular ions”. In: *Phys. Rev. A* 79 (3 2009), p. 032716.

[36] A. K. Hansen et al. “Efficient rotational cooling of Coulomb-crystallized molecular ions by a helium buffer gas”. In: *Nature* 508 (2014), pp. 76–79.

[37] S. Schiller et al. “Quantum state preparation of homonuclear molecular ions enabled via a cold buffer gas: An ab initio study for the H_2^+ and the D_2^+ case”. In: *Phys. Rev. A* 95 (4 2017), p. 043411.

[38] Chien-Yu Lien et al. “Broadband optical cooling of molecular rotors from room temperature to the ground state”. In: 5 (2014), p. 4783.

[39] Jason H. V. Nguyen et al. “Challenges of laser-cooling molecular ions”. In: *New J. Phys.* 13 (2011), p. 063023.

[40] Patrick R. Stollenwerk et al. “Electronic spectroscopy of a cold SiO^+ sample: Implications for optical pumping”. In: *J. Mol. Spectrosc.* 332 (2017), pp. 26 –32.

[41] I. S. Vogelius, L. B. Madsen, and M. Drewsen. “Probabilistic state preparation of a single molecular ion by projection measurement”. In: *J. Phys. B* 39 (2006), S1259.

[42] S. Ding and D. N. Matsukevich. “Quantum logic for the control and manipulation of molecular ions using a frequency comb”. In: *New J. Phys.* 14.2 (2012), p. 023028.

[43] Wade G. Rellergert et al. “Evidence for sympathetic vibrational cooling of translationally cold molecules”. In: *Nature* 495 (2013), pp. 490 –494.

[44] Eric R. Hudson. “Sympathetic cooling of molecular ions with ultracold atoms”. In: *EPJ Techniques and Instrumentation* 3.1 (2016).

[45] Thierry Stoecklin et al. “Explanation of efficient quenching of molecular ion vibrational motion by ultracold atoms”. In: *Nature Communications* 7 (2016), p. 11234.

[46] D. Hanneke, R. A. Carollo, and D. A. Lane. “High sensitivity to variation in the proton-to-electron mass ratio in O_2^+”. In: *Phys. Rev. A* 94 (5 2016), p. 050101.

[47] Masatoshi Kajita. “Accuracy estimation of the $^{16}O_2^+$ transition frequencies targeting the search for the variation in the proton-electron mass ratio”. In: *Phys. Rev. A* 95 (2 2017), p. 023418.

[48] Masatoshi Kajita et al. “Test of m_p/m_e changes using vibrational transitions in N_2^+”. In: *Phys. Rev. A* 89 (3 2014), p. 032509.

[49] J. P. Karr et al. “Hydrogen molecular ions for improved determination of fundamental constants”. In: *Phys. Rev. A* 94 (5 2016), 050501(R).

[50] S. Schiller and V. Korobov. “Tests of time independence of the electron and nuclear masses with ultracold molecules”. In: *Phys. Rev. A* 71 (3 2005), p. 032505.

[51] J. C. J. Koelemeij. “Forbidden vibrations”. In: *Nat. Phys.* 10 (2014), p. 800.

[52] A.G.G.M. Tielens and T.P. Snow. *The Diffuse Interstellar Bands*. Vol. 202. Springer Netherlands, 1995.

[53] Eric. Herbst. “The chemistry of interstellar space”. In: *Chem. Soc. Rev.* 30 (2001), pp. 168–176.

[54] J. C. J. Koelemeij et al. “Vibrational spectroscopy of HD^+ with 2-ppb accuracy”. In: *Phys. Rev. Lett.* 98.17 (2007), p. 173002.

[55] Keri L Williams, Ina T Martin, and Ellen R Fisher. “On the importance of ions and ion-molecule reactions to plasma-surface interface reactions”. In: *J. Am. Soc. Mass Spectrom.* 13.5 (1044-0305), pp. 518 –529.

[56] Heather Lewandowski. “Controlled ion chemistry”. In: *North American Conference on Trapped Atomic Ions* (2017), Invited talk.

[57] Hendrick L. Bethlem and Gerard Meijer. “Production and application of translationally cold molecules”. In: *Int. Rev. Phys. Chem.* 22.1 (2003), pp. 73–128.

[58] Stefan Willitsch et al. “Cold Reactive Collisions between Laser-Cooled Ions and Velocity-Selected Neutral Molecules”. In: *Phys. Rev. Lett.* 100 (4 2008), p. 043203.

[59] Martin T. Bell and Timothy P. Softley. “Ultracold molecules and ultracold chemistry”. In: *Molecular Physics* 107.2 (2009), pp. 99–132.

[60] R. V. Krems. “Cold controlled chemistry”. In: *Phys. Chem. Chem. Phys.* 10 (28 2008), pp. 4079–4092.

[61] N. F. Dalleska, Kevin C. Crellin, and P. B. Armentrout. “Reactions of alkaline earth ions with hydrogen, deuterium, and hydrogen deuteride”. In: *J. Phys. Chem.* 97.13 (1993), pp. 3123–3128.

[62] Peter F. Staanum et al. “Probing isotope effects in chemical reactions using single ions”. In: *Phys. Rev. Lett.* 100.24 (2008), p. 243003.

[63] Daniel Rösch et al. “Design and characterization of a linear quadrupole ion trap for high-resolution Coulomb-crystal time-of-flight mass spectrometry”. In: *EPJ Techniques and Instrumentation* 3.1 (2016), p. 5.

[64] Stefan Willitsch. “Molecules and Ions at Very Low Temperatures”. In: *Chimia* 63.1-2 (2009), pp. 54–57.

[65] Alexander D. Gingell et al. “Cold chemistry with electronically excited Ca^+ Coulomb crystals”. In: *J. Chem. Phys.* 133.19 (2010), p. 194302.

[66] Martin T. Bell et al. “Ion-molecule chemistry at very low temperatures: cold chemical reactions between Coulomb-crystallized ions and velocity-selected neutral molecules”. In: *Faraday Discuss.* 142 (0 2009), pp. 73–91.

[67] Prateek Puri et al. “Synthesis of mixed hypermetallic oxide $BaOCa^+$ from laser-cooled reagents in an atom-ion hybrid trap”. In: *Science* 357.6358 (2017), pp. 1370–1375.

[68] Gerald Gabrielse. “Testing the standard model and its symmetries”. In: *North American Conference on Trapped Atomic Ions* (2017), Invited talk.

[69] S. Alighanbari et al. “Rotational spectroscopy of cold and trapped molecular ions in the Lamb Dicke regime”. In: *Nat. Phys.* (2018), pp. 1745–2481.

[70] Masatoshi Kajita et al. “Estimated accuracies of pure XH^+ (X: even isotopes of group II atoms) vibrational transition frequencies: towards the test of the variance in m_p/m_e”. In: *J. Phys. B* 44.2 (2011), p. 025402.

[71] C. Monroe et al. “Demonstration of a Fundamental Quantum Logic Gate”. In: *Phys. Rev. Lett.* 75 (25 1995), pp. 4714 –4717.

[72] P. O. Schmidt et al. “Spectroscopy using quantum logic”. In: *Science* 309 (5735 2005), pp. 749–752.

[73] Fabian Wolf et al. “Non-destructive state detection for quantum logic spectroscopy of molecular ions”. In: *Nature* 530.7591 (2016), pp. 457–460.

[74] Wes Campbell. “Atomic envoy enables molecular control”. In: *Science* 545 (2017), pp. 164 –165.

[75] David Patterson. “Method for preparation and readout of polyatomic molecules in single quantum states”. In: *Phys. Rev. A* 97 (3 2018), p. 033403.

[76] T. D. Lee and C. N. Yang. *Elementary Particles and Weak Interactions*. 1957.

[77] C. S. Wu et al. “Experimental Test of Parity Conservation in Beta Decay”. In: *Phys. Rev.* 105 (4 1957), pp. 1413–1415.

[78] Sandra Eibenberger, John Doyle, and David Patterson. “Enantiomer-Specific State Transfer of Chiral Molecules”. In: *Phys. Rev. Lett.* 118 (12 2017), p. 123002.

[79] William A. Bonner. “Parity violation and the evolution of biomolecular homochirality”. In: *Chirality* 12.3 (2000), pp. 114–126.

[80] Martin Quack. “How Important is Parity Violation for Molecular and Biomolecular Chirality?” In: *Angewandte Chemie International Edition* 41.24 (2002), pp. 4618–4630.

[81] Minori Abe et al. “Ab initio study on potential energy curves of electronic ground and excited states of $^{40}CaH^+$ molecule”. In: *Chem. Phys. Lett.* 521 (2012), pp. 31 –35.

[82] Raymond E. March. “An Introduction to Quadrupole Ion Trap Mass Spectrometry”. In: *J. Mass Spect.* 32.4 (), pp. 351–449.

[83] R. F. Wuerker, H. Shelton, and R. V. Langmuir. “Electrodynamic Containment of Charged Particles”. In: *Journal of Applied Physics* 30.3 (1959), pp. 342–349.

[84] T. Jones. *Mathieu’s equations and the ideal rf trap*.

[85] Pradip K. Ghosh. *Ion traps*. Clarendon Press, 1995.

[86] B. Roth, P. Blythe, and S. Schiller. “Motional resonance coupling in cold multispecies Coulomb crystals”. In: *Phys. Rev. A* 75 (2 2007), p. 023402.

[87] Jean Pierre Hansen. “Statistical Mechanics of Dense Ionized Matter. I. Equilibrium Properties of the Classical One-Component Plasma”. In: *Phys. Rev. A* 8 (6 1973), pp. 3096–3109.

[88] Stefan Willitch. “Coulomb crystallized molecular ions in traps: methods, applications, prospects, International Reviews in Physical Chemistry”. In: *Int. Rev. Phys. Chem.* 31.2 (2012), pp. 175 –199.

[89] L. Hornekær et al. “Structural Properties of Two-Component Coulomb Crystals in Linear Paul Traps”. In: *Phys. Rev. Lett.* 86 (10 2001), pp. 1994–1997.

[90] M. Drewsen et al. “Ion Coulomb crystals: a tool for studying ion processes”. In: *Int. J. of Mass Spectrometry* 229.1 (2003), pp. 83 –91.

[91] K. Mølhave and M. Drewsen. “Formation of translationally cold MgH^+ and MgD^+ molecules in an ion trap”. In: *Phys. Rev. A* 62 (1 2000), p. 011401.

[92] D. J. Wineland, R. E. Drullinger, and F. L. Walls. “Radiation-Pressure Cooling of Bound Resonant Absorbers”. In: *Phys. Rev. Lett.* 40.25 (1978), pp. 1639–1642.

[93] M. Neuhauser et al. “Optical-Sideband Cooling of Visible Atom Cloud Confined in Parabolic Well”. In: *Phys. Rev. Lett.* 41.4 (1978), pp. 233 –236.

[94] E. S. Shuman, J. F. Barry, and D. DeMille. “Laser cooling of a diatomic molecule”. In: *Nature* 467 (2010), 820 – 823.

[95] R. Rugango. “Spectroscopy of Molecular Ions in Coulomb Crystals”. In: *Thesis, GA Inst. of Tech.* (2016).

[96] J. E. Goeders et al. “Identifying single molecular ions by resolved sideband measurements”. In: *J. Phys. Chem. A,* 117 (2013), 9725–9731.

[97] J. D. Siverns et al. “On the application of radio frequency voltages to ion traps via helical resonators”. In: *Applied Physics B.* 106 (2011), p. 327.

[98] J. Keller et al. “Precise determination of micromotion for trapped-ion optical clocks”. In: *Journal of Applied Physics* 118.10 (2015), p. 104501.

[99] Ncamiso B. Khanyile. “Vibrational spectroscopy of sympathetically laser-cooled CaH^+”. In: *Thesis, GA Inst. of Tech.* (2015).

[100] S. C. Doret. “Transfer cavity stabilized HeNe based laser frequency stabilization”. In: (2011).

[101] D. E. Spence, P. N. Kean, and W. Sibbett. “60-fsec pulse generation from a self-mode-locked Ti:sapphire laser”. In: *Opt. Lett.* 16.1 (1991), pp. 42–44.

[102] Andrew Marc Weiner. *Ultrafast Optics*. John Wiley and Sons, 2009.

[103] Andrew M. Weiner. “Ultrafast optical pulse shaping: A tutorial review”. In: *Opt. Commun.* 284.15 (2011), pp. 3669–3692.

[104] Chien-Yu Lien. “Broadband Optical Cooling of Molecular Rotors”. In: *Thesis, Northwestern University* (2014).

[105] Minori Abe et al. “Ab initio study on vibrational dipole moments of XH^+ molecular ions: X = ^{24}Mg, ^{40}Ca, ^{64}Zn, ^{88}Sr, ^{114}Cd, ^{138}Ba, ^{174}Yb and ^{202}Hg”. In: *J. Phys. B* 43 (2010), p. 245102.

[106] A. Pardo et al. “The $A^1\Sigma^+$ - $X^1\Sigma^+$ Band System of the KH and KD Molecules”. In: *Chem. Phys.* 117 (1987), pp. 149–162.

[107] W. C. Stwalley, W.T. Zemke, and S. C. Yang. “Spectroscopy and Structure of the Alkali Hydride Diatomic Molecules and their Ions”. In: *J. Phys. Chem. Ref. Data* 20 (1991), p. 153.

[108] I. R. Bartky. “The $A^1\Sigma - X^1\Sigma$ transition of ^{39}KH and ^{39}KD. Vibrational numbering and molecular constants”. In: *J. Mol. Spectrosc.* 20 (1966), pp. 299–311.

[109] A. Pardo et al. “Laser-induced fluorescence and inelastic collisions of KH molecule”. In: *J. Mol. Spectrosc.* 97 (2 1983), pp. 248–252.

[110] Robert J. Le Roy. “LEVEL A computer program for solving the radial Schrödinger equation for bound and quasibound levels”. In: *J. Quant. Spectrosc. Radiat. Transfer* 186 (2017), pp. 167–178.

[111] W. Zrafi et al. “Evaluation of the adiabatic correction for LiH, RbH and CsH molecules”. In: *J. Mol. Struct.* 777.1–3 (2006), pp. 87 –97.

[112] Wei-Cheng Tung, Michele Pavanello, and Ludwik Adamowicz. “Very accurate potential energy curve of the LiH molecule”. In: *J. Chem. Phys.* 134.6 (2011), p. 064117.

[113] Robert M. Parrish et al. “Psi4 1.1: An Open-Source Electronic Structure Program Emphasizing Automation, Advanced Libraries, and Interoperability”. In: *Journal of Chemical Theory and Computation* 13.7 (2017), pp. 3185–3197.

[114] Zoltán Rolik et al. “An efficient linear-scaling CCSD(T) method based on local natural orbitals”. In: *The Journal of Chemical Physics* 139.9 (2013), p. 094105.

[115] J.F. Stanton et al. *CFOUR, Coupled-Cluster techniques for Computational Chemistry, a quantum-chemical program package*. contributions from A.A. Auer, R.J. Bartlett, U. Benedikt, C. Berger, D.E. Bernholdt, Y.J. Bomble, O. Christiansen, F. Engel, R. Faber, M. Heckert, O. Heun, C. Huber, T.-C. Jagau, D. Jonsson, J. Jusélius, K. Klein, W.J. Lauderdale, F. Lipparini, T. Metzroth, L.A. Mück, D.P. O’Neill, D.R. Price, E. Prochnow, C. Puzzarini, K. Ruud, F. Schiffmann, W. Schwalbach, C. Simmons, S. Stopkowicz, A. Tajti, J. Vázquez, F. Wang, J.D. Watts and the integral packages MOLECULE (J. Almlöf and P.R. Taylor), PROPS (P.R. Taylor), ABACUS (T. Helgaker, H.J. Aa. Jensen, P. Jørgensen, and J. Olsen), and ECP routines by A. V. Mitin and C. van Wüllen.

[116] J. D. Weinstein et al. “Magnetic trapping of calcium monohydride molecules at millikelvin temperatures”. In: *Nature* 395 (1998), pp. 148–150.

[117] T. Schneider et al. “All-optical preparation of molecular ions in the rovibrational ground state”. In: *Nature Physics* 6 (2010), pp. 275–278.

[118] M. G. Kokish, M. R. Dietrich, and B. C. Odom. “Simple and Compact Nozzle Design for Laser Vaporization Sources”. In: *J. Phys. B* 49 (2015).

[119] Jason Clark et al. “The $A^1\Pi \rightarrow X\ ^1\Sigma^+$ (2,0) transition in ^{11}BH and ^{10}BH observed by (1+2)-photon resonance-enhanced multiphoton ionization spectroscopy”. In: *Chem. Phys. Lett.* 340 (2001), pp. 45 –54.

[120] Wei-tzou Luh and William C. Stwalley. “The $X^1\Sigma^+$, $A^1\Pi$, and $B^1\Sigma^+$ Potential Energy Curves and Spectroscopy of BH”. In: *J. Mol. Spectr.* 102 (1983), pp. 212–223.

[121] R. Rugango et al. “Trapping and Sympathetic Cooling of Boron Ions”. In: *arXiv:1609.09521* (2016).

[122] R. Basner, M. Schmidt, and K. Becker. “Absolute total and partial cross sections for the electron impact ionization of diborane (B_2H_6)”. In: *J. Chem. Phys.* 118.5 (2003), pp. 2153 –2158.

[123] K. Højbjerre et al. “Rotational state resolved photodissociation spectroscopy of translationally and vibrationally cold MgH^+ ions: toward rotational cooling of molecular ions”. In: *New J. Phys.* 11.5 (2009), p. 055026.

[124] Stefan Willitsch. “Coulomb-crystallised molecular ions in traps: methods, applications, prospects”. In: *International Reviews in Physical Chemistry* 31.2 (2012), pp. 175–199.

[125] Jeanne L. McHale. *Molecular Spectroscopy*. Pearson.

[126] C. Roos. “Controlling the quantum state of trapped ions”. In: *Thesis, Universtität Innsbruck* (2000).

[127] D. Leibfried et al. “Quantum dynamics of single trapped ions”. In: *Rev. Mod. Phys.* 75 (1 2003), pp. 281–324.

[128] R. W. Numrich. 1974.